

Air Force Institute of Technology

**AFIT Scholar**

---

Theses and Dissertations

Student Graduate Works

---

3-10-2010

## Development and Evaluation of a Multistatic Ultrawideband Random Noise Radar

Matthew E. Nelms

Follow this and additional works at: <https://scholar.afit.edu/etd>



Part of the [Signal Processing Commons](#), and the [Systems and Communications Commons](#)

---

### Recommended Citation

Nelms, Matthew E., "Development and Evaluation of a Multistatic Ultrawideband Random Noise Radar" (2010). *Theses and Dissertations*. 2018.  
<https://scholar.afit.edu/etd/2018>

This Thesis is brought to you for free and open access by the Student Graduate Works at AFIT Scholar. It has been accepted for inclusion in Theses and Dissertations by an authorized administrator of AFIT Scholar. For more information, please contact [richard.mansfield@afit.edu](mailto:richard.mansfield@afit.edu).



**DEVELOPMENT AND EVALUATION OF A  
MULTISTATIC ULTRAWIDEBAND  
RANDOM NOISE RADAR**

THESIS

Matthew E. Nelms, Major, USAF  
AFIT/GE/ENG/10-21

**DEPARTMENT OF THE AIR FORCE  
AIR UNIVERSITY**

***AIR FORCE INSTITUTE OF TECHNOLOGY***

**Wright-Patterson Air Force Base, Ohio**

APPROVED FOR PUBLIC RELEASE; DISTRIBUTION UNLIMITED

The views expressed in this thesis are those of the author and do not reflect the official policy or position of the United States Air Force, Department of Defense, or the United States Government.

AFIT/GE/ENG/10-21

DEVELOPMENT AND EVALUATION OF A MULTISTATIC  
ULTRAWIDEBAND RANDOM NOISE RADAR

THESIS

Presented to the Faculty  
Department of Electrical and Computer Engineering  
Graduate School of Engineering and Management  
Air Force Institute of Technology  
Air University  
Air Education and Training Command  
in Partial Fulfillment of the Requirements for the  
Degree of Master of Science in Electrical Engineering

Matthew E. Nelms, BSEE

Major, USAF

March 2010

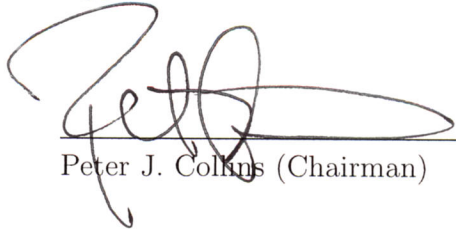
APPROVED FOR PUBLIC RELEASE; DISTRIBUTION UNLIMITED



DEVELOPMENT AND EVALUATION OF A MULTISTATIC  
ULTRAWIDEBAND RANDOM NOISE RADAR

Matthew E. Nelms, BSEE  
Major, USAF

Approved:



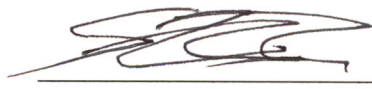
Peter J. Collins (Chairman)

12 MAR 2010  
Date



Michael A. Saville (Member)

12 MAR 2010  
Date



Steven K. Rogers (Member)

12 MAR 2010  
Date

## Abstract

As advances in shaping and materials continue to press the frontiers of signature reduction, the forward eyes and ears of operations, being a platform's onboard sensor systems, have kept pace with low observable designs by significantly reducing both intentional and unintentional emissions. A general shift to passive sensor suites may be the simplest near-term solution. However, superior situational awareness requires detection, discrimination and tracking of vast arrays of target classes across diverse sensing environments where active sensors may provide greater performance. From urban dismount identification to deep space collision avoidance, conventional active radars can deliver the high level of fidelity necessary for producing actionable imagery. The penalty is often an increase in the system's complexity, as well as the likelihood of radio frequency interference and interception.

The AFIT noise network (NoNET) is an experimental multistatic ultrawideband random noise radar designed to produce highly accurate, highly resolved imagery of a target scene while maintaining a simple design and low probability of intercept posture. The research studies the radar node design and the feasibility in processing the bistatic channel information of a cluster of widely distributed noise radar nodes. A system characterization is used to predict theoretical localization performance metrics. Design and integration of a distributed and central signal and data processing architecture enables the MATLAB<sup>®</sup>-driven signal data acquisition, digital processing and multi-sensor image fusion. After design and integration is successfully accomplished, research objectives focus on assessing the target localization accuracy and resolution performance of first the monostatic system and then the multistatic system of systems. Experimental evaluation of the monostatic localization perfor-

mance reveals its range measurement error standard deviation is 4.8 cm with a range resolution of  $87.2(\pm 5.9)$  cm. Finally, a joint coverage area within the AFIT RCS range allows single and multi-target scenarios for assessing the 16-channel multistatic solution. The average multistatic localization error is assessed as  $7.7(\pm 3.1)$  cm and a comparative analysis is performed against the netted monostatic solution. Results show that active sensing with a low probability of intercept (LPI) multistatic radar, like the AFIT NoNET, is not only feasible but capable of sub-meter accuracy and near meter-resolution in its 2-dimensional fused imagery products.

## Acknowledgements

I first give all honor and credit to my savior and king the Lord Jesus Christ, who for the joy that was in it bore the weight of that which separated us from Him. Thank You for literally ransoming my life. To You be any and all glory. To my beautiful and gracious bride - I will never forget your encouragement and listening ear. Thank you for being my best friend, and in the daily grind, inspiring the right attitude to help us through this endeavor (not to mention your willingness to go over some of your earlier work with me). To my son - you have such a special spirit. Thank you for being so excited with me for Saturday mornings. Somehow even at 2 yrs old, you seemed to understand why I was away so much. To my parents - thank you for teaching me not to wait to look *back* at footprints in the sand but to recognize the One who is carrying me today. And for continually pointing me toward and helping me in my academic journey. Finally, I owe a debt of gratitude to my advisor and the faculty & staff at AFIT - you put your hearts into educating and are superb at what you do.

Matthew E. Nelms

# Table of Contents

|   | Page |
|---|------|
| Abstract . . . . .  | iv   |
| Acknowledgements . . . . .                                      | vi   |
| List of Figures . . . . .                                       | ix   |
| List of Tables . . . . .  | xii  |
| I. Introduction . . . . .                                       | 1    |
| 1.1 Problem Description . . . . .                               | 1    |
| 1.2 Motivation . . . . .  | 2    |
| 1.3 Research Goals . . . . .                                    | 3    |
| 1.4 Background . . . . .  | 5    |
| 1.4.1 UWB Noise Radar . . . . .                                 | 5    |
| 1.4.2 Multistatic Radar Systems . . . . .                       | 10   |
| II. Theory . . . . .  | 17   |
| 2.1 Chapter Overview . . . . .                                  | 17   |
| 2.2 Transmitter Theory . . . . .                                | 17   |
| 2.2.1 Continuous Random Noise . . . . .                         | 17   |
| 2.2.2 Radar Ambiguity Function . . . . .                        | 19   |
| 2.2.3 Range Resolution with UWB Random Noise . . . . .          | 21   |
| 2.2.4 Correlation of UWB Noise . . . . .                        | 24   |
| 2.3 Receiver Theory . . . . .                                   | 25   |
| 2.3.1 Direct-Conversion . . . . .                               | 26   |
| 2.3.2 Digital Correlation . . . . .                             | 30   |
| 2.3.3 Theoretical Range Accuracy . . . . .                      | 32   |
| 2.4 Multistatic Theory . . . . .                                | 34   |
| 2.4.1 Multistatic Geometry and Measurement Parameters . . . . . | 35   |
| 2.4.2 Multistatic Signal Model . . . . .                        | 42   |
| 2.5 Chapter Conclusion . . . . .                                | 45   |
| III. System Characterization and Experimental Design . . . . .  | 46   |
| 3.1 Chapter Overview . . . . .                                  | 46   |
| 3.2 System Characterization . . . . .                           | 47   |
| 3.2.1 System Response and Calibration Experiments . . . . .     | 48   |
| 3.3 Monostatic Localization Performance . . . . .               | 63   |
| 3.3.1 Range Resolution Experiment . . . . .                     | 63   |
| 3.3.2 Range Accuracy Experiment . . . . .                       | 64   |

|   | Page |
|---|------|
| 3.4 Multistatic Localization Performance . . . . .              | 66   |
| 3.4.1 Downrange and Cross-Range Resolution Experiment . . . . . | 67   |
| 3.4.2 Downrange and Cross-Range Accuracy Experiment . . . . .   | 69   |
| 3.5 Risk Reduction . . . . .                                    | 70   |
| 3.6 Chapter Conclusion . . . . .                                | 71   |
| IV. Analysis of Results . . . . .                               | 72   |
| 4.1 Chapter Overview . . . . .                                  | 72   |
| 4.2 Monostatic Performance . . . . .                            | 72   |
| 4.2.1 Processing for Evaluation . . . . .                       | 72   |
| 4.2.2 Monostatic Range Resolution . . . . .                     | 75   |
| 4.2.3 Monostatic Range Accuracy . . . . .                       | 79   |
| 4.3 Multistatic Performance . . . . .                           | 84   |
| 4.3.1 Assessment of Range and Cross-Range Resolution . . . . .  | 86   |
| 4.3.2 Assessment of Range and Cross-Range Accuracy . . . . .    | 94   |
| 4.4 Chapter Conclusion . . . . .                                | 100  |
| V. Conclusions . . . . .  | 101  |
| 5.1 Chapter Overview . . . . .                                  | 101  |
| 5.2 Review of Objectives and Methodology . . . . .              | 101  |
| 5.3 Results and Contributions . . . . .                         | 102  |
| 5.4 Future Work . . . . .                                       | 103  |
| 5.4.1 System Hardware Improvements . . . . .                    | 104  |
| 5.4.2 System Software Improvements . . . . .                    | 105  |
| Appendix A. MATLAB <sup>®</sup> Scripts . . . . .               | 106  |
| Bibliography . . . . .  | 121  |

## List of Figures

| Figure |  | Page |
|--------|--|------|
| 1.     | Notional noise radar block diagrams used in early resolution computations . . . . .  | 6    |
| 2.     | Thumbtack ambiguity diagram depicting ideal resolution and ambiguity qualities of a waveform . . . . .                                       | 7    |
| 3.     | Demonstrated detection and estimation of human targets using a network of three monostatic UWB-RN radars at AFIT . . . . .                   | 9    |
| 4.     | Depiction of the two types of channels formed by transmitter-target-receiver signal paths that make up a multistatic radar network . . . . . | 11   |
| 5.     | Graphic depicting the coverage area and survivability concepts provided by a multistatic radar architecture . . . . .                        | 13   |
| 6.     | Spatial decorrelation in independent measurements of a MIMO multistatic radar . . . . .  | 15   |
| 7.     | Target resolution issues in a 4 channel multistatic radar system . . . . .   | 16   |
| 8.     | Ambiguity Diagram of a 15-bit pseudorandom binary phase coded waveform . . . . .   | 21   |
| 9.     | Autocorrelation function output of a 15-bit pseudorandom binary phase coded waveform . . . . .   | 22   |
| 10.    | Block Diagram of the noise radar receiver design. . . . .  | 25   |
| 11.    | Quantization noise spectra produced by a white Gaussian input signal . . . . .   | 29   |
| 12.    | Graphical Representation of the Fourier Transform property of convolution . . . . .  | 30   |
| 13.    | AFIT NoNET radar system block diagram . . . . .  | 32   |
| 14.    | Example of a multistatic localization estimate using multilateration of isorange contours . . . . .  | 36   |

| Figure |  | Page |
|--------|--|------|
| 15.    | Geometry of the planar bistatic measurement . . . . .  | 37   |
| 16.    | Multistatic radar can produce varying degrees of<br>cross-range resolution . . . . .               | 39   |
| 17.    | The ground plane multipath effect example of<br>geometry dependent propagation factors. . . . .    | 40   |
| 18.    | Experimental set-up of NTR6 characterization . . . . .   | 49   |
| 19.    | System Response and plotted statistics for<br>characterization measurement 1 . . . . .             | 51   |
| 20.    | System Response and plotted statistics for<br>characterization measurement 2 . . . . .             | 52   |
| 21.    | System Response and plotted statistics for<br>characterization measurement 3 . . . . .             | 54   |
| 22.    | Multistatic signal processing architecture . . . . .   | 57   |
| 23.    | Response features and post-processing evolution of<br>the correlation receiver response . . . . .  | 60   |
| 24.    | Experimental set-up and results of the monostatic<br>2-pt range calibration measurements . . . . . | 62   |
| 25.    | Experimental set-up of the monostatic range<br>resolution measurements . . . . .                   | 64   |
| 26.    | Experimental set-up of NTR6 monostatic range<br>accuracy measurements . . . . .                    | 65   |
| 27.    | Experimental set-up of the multistatic resolution measurements . . . .                             | 69   |
| 28.    | Experimental set-up of the multistatic localization<br>accuracy measurements . . . . .             | 70   |
| 29.    | Response features and post-processing evolution of<br>the correlation receiver response . . . . .  | 74   |
| 30.    | Sample monostatic range resolution measurements<br>using NTR3 and clutter suppression . . . . .    | 77   |
| 31.    | Sample monostatic range resolution measurements<br>without clutter suppression . . . . .           | 78   |
| 32.    | Range accuracy results using clutter suppression . . . . .   | 81   |



| Figure |   | Page |
|--------|---|------|
| 33.    | Range accuracy results of monostatic measurements with clutter suppression . . . . .  | 82   |
| 34.    | Range accuracy monostatic measurement using NTR3 without clutter suppression . . . . .  | 83   |
| 35.    | An example array of all discrete channel images . . . . .   | 85   |
| 36.    | First set of multistatic and netted monostatic imagery used to assess the range and cross-range resolution of the AFIT NoNET . . . . .          | 89   |
| 37.    | Second set of multistatic and netted monostatic imagery used to assess the range and cross-range resolution of the AFIT NoNET . . . . .         | 90   |
| 38.    | Third set of multistatic and netted monostatic imagery used to assess the range and cross-range resolution of the AFIT NoNET . . . . .          | 91   |
| 39.    | Forth set of multistatic and netted monostatic imagery used to assess the range and cross-range resolution of the AFIT NoNET . . . . .          | 92   |
| 40.    | Fifth set of multistatic and netted monostatic imagery used to assess the range and cross-range resolution of the AFIT NoNET . . . . .          | 93   |
| 41.    | First set of multistatic and netted monostatic imagery used to assess the range and cross-range accuracy of the AFIT NoNET . . . . .            | 96   |
| 42.    | Second set of multistatic and netted monostatic imagery used to assess the range and cross-range accuracy of the AFIT NoNET . . . . .           | 97   |
| 43.    | Third set of multistatic and netted monostatic imagery used to assess the range and cross-range accuracy of the AFIT NoNET . . . . .            | 98   |
| 44.    | The array of discrete images of the available 16 multistatic channels prior to central processing fusion for the first accuracy trial . . . . . | 99   |
| 45.    | Example of the node assignment's MATLAB <sup>®</sup> data structure . . . . .   | 107  |

## List of Tables

| Table |  | Page |
|-------|--|------|
| 1.    | Characterization and range calibration experiments . . . . .                             | 48   |
| 2.    | Statistics of the antenna spillover response peak . . . . .                              | 61   |
| 3.    | Monostatic range resolution test matrix . . . . .  | 63   |
| 4.    | Monostatic range accuracy test matrix . . . . .  | 65   |
| 5.    | Multistatic range and cross-range resolution<br>experimental test matrix . . . . .       | 69   |
| 6.    | Multistatic range and cross-range accuracy<br>experimental test matrix . . . . .         | 70   |
| 7.    | Monostatic range resolution measurement results . . . . .                                | 76   |
| 8.    | Monostatic range accuracy measurement results . . . . .                                  | 80   |
| 9.    | Multistatic and Netted Monostatic localization<br>accuracy measurement results . . . . . | 95   |

# DEVELOPMENT AND EVALUATION OF A MULTISTATIC ULTRAWIDEBAND RANDOM NOISE RADAR

## I. Introduction

### 1.1 Problem Description

New research in multistatic radar systems is demonstrating the potential detection and estimation gains created by multi-transmitter, multi-receiver shared coverage areas. Spatial diversity in a distributed active sensor system has been shown to reduce the impact of target fading due to propagation factors, target scintillation and glint, and even lessen the effectiveness of certain stealth techniques [34, 55]. Additionally, the angle diversity can dramatically reduce the geometric dilution of parameters being estimated. However, such multistatic gains are not realized without a price. The overarching problem with the multistatic design is the level of complexity that results from things like hybrid distributed/central processing architectures, distributed control and supporting datalink infrastructures, and adverse mutual interference effects within the shared electromagnetic spectrum. The question becomes, what fidelity of distributed estimation (i.e. accuracy and resolution of target parameter estimation) can be obtained while still maintaining a simplistic design. It is a classic engineering problem.

An added complication is the typical types of radar and their associated waveforms that most multistatic systems employ. Needing high range resolution for target discrimination and elimination of target ghosts, pulsed-Doppler systems using phase or frequency coded pulse compression waveforms are often the radar of choice. How-

ever, electronic support systems worldwide are readily detecting, identifying, and exploiting the deterministic waveforms of these systems, which is an obvious issue for most military operations. Now, the problem consists of not only a simple, distributed sensor architecture capable of multistatic operations, but it would ideally maintain a covert, low probability of intercept posture.

Consequently, this research is conducted to determine whether a radar that uses an ultrawideband random noise (UWB-RN) transmit waveform coupled with a simple direct-conversion, digital correlation receiver design is a viable architecture for covert, multistatic operations. Furthermore, characterization of the single node radar at an operating level, and evaluation of the monostatic measurement performance will determine whether measurement fidelity will allow an accurate central multilateration of a target scene. These questions are answered by analyzing the results of downrange monostatic and multistatic measurements to assess the system's performance in localizing and discriminating between multiple targets in both range and cross-range. If the design solution is successful, the multistatic UWB-RN radar would open doors to new noise technology research and unlock numerous special applications for sensor fusion studies at AFIT.

## **1.2 Motivation**

The ever-present challenge faced by U.S. Department of Defense Intelligence, Surveillance, and Reconnaissance (ISR) agencies is the need for greater performance from sensor assets. Key performance parameters like coverage area, detection range, target estimation accuracy and resolution, and certainly reliability and survivability are some of the typical enhancements required in imaging radar upgrades and the next generation of ISR sensors. More and more when a new material sensor solution is acquired to meet a capability need, it is delivered in the form of a distributed sensor

architecture. Research and operations are now seeking the many benefits of fusing multiple, simultaneously yet independently collected observations of scenes into fully registered, highly resolved, and often hyperspectral images. The goal is a single, integrated picture providing a situational awareness that is more accurate and more actionable than the sum of its individual parts.

In addition, the need to reduce the detectability of active sensors operating on the ground, in the air, and in space is not simply a matter of enhancing ones defensive posture. Most ISR missions are linked by the common key enabler of covertness. For superior ISR, the capability to sense, yet not be sensed is vital. And it is this problem of being active but undetected that motivates the mounting research into noise technology. The UWB-RN radar is a concept that has now reached a level of sustained interest in academic, commercial, and defense sectors. While the researched application areas are diverse, including ground, foliage and wall penetration capabilities, until now, its suitability and full utility in a multistatic architecture has not been studied.

### **1.3 Research Goals**

Specific research into UWB-RN radar began at AFIT in 2009, and three prototype monostatic noise technology radar (NTR) nodes were developed. By triangulation of individual monostatic NTR measurements, a through-the-wall (TTW) radar imaging capability was demonstrated that same year [43]. The follow-on research presented in this thesis is both foundational and pioneering in an effort to advance this form of covert distributed sensor technology, known as the AFIT Noise Network (NoNET). The primary objectives of the research are to:

1. develop and assess a multistatic imaging capability with enhanced range and cross-range resolution and accuracy (via additional radar nodes and full utiliza-

- tion of all multistatic channels),
2. develop an enhanced distributed processing design (reduce latency; increase precision via distributed and centralized DSP improvements),
  3. evaluate the critical radar node localization performance parameters of range resolution and range accuracy, and
  4. provide end-to-end theoretical and experimental system level characterization of the noise radar.

The secondary objectives include but are not limited to:

1. the development of a modular processing design for greater flexibility,
2. increasing the system operability with a centrally controlled and centrally fused architecture all via a datalink interface commanded in MATLAB<sup>®</sup>,
3. enhancing the overall mobility of the distributed sensor network (rehosting to a leaner platform and use of wireless datalinks).

Being the classic engineering problem that it is, achieving these research goals requires both breadth and depth in its theoretical development found in Chapter 2. The theory becomes the foundation for presenting the design and experimental methodology of Chapter 3, upon which a critical analysis can be performed. Ultimately, the results of the experimental investigation, which are detailed in Chapter 4, will present final performance assessments, which will determine whether the multistatic UWB-RN radar design strikes the rational balance in performance and simplicity that warrants ongoing development and research. Chapter 5 discusses such conclusions with a look at the possible areas of future work. To begin this journey, a detailed background discussion on the major concepts and components is first presented, which places the research into its appropriate context.

## 1.4 Background

In order to understand the full range of potential areas of analysis of a multistatic UWB-RN radar system, the background section first defines key terms in the appropriate context of distributed sensor system, while providing a brief look into the distinct evolutions of the noise radar and multistatic operations of distributed sensor systems. A detailed discussion of the most recent research in relevant applications is also presented.

### 1.4.1 UWB Noise Radar.

#### 1.4.1.1 Definition and History.

Historically, the design principle of a noise radar is sensing the degree of correlation between the intentionally stochastic or stochastic-like transmission signal and that of the received signal. While all transmitted and received signals have some amount of noise in them (the reduction of which is a radar engineering field in itself), the noise radar is designed to produce and use the stochastic nature of a signal for radar detection and estimation purposes. This concept of using noise as a transmit waveform first emerged about 50 years ago [24]. A broad look at the numerous designs and classifications places these systems into two major families, those that use true random noise and those classified as pseudorandom noise (PRN) radars. While both types are marked with relatively slow early evolutions, the solid state microwave, wideband communications, and digital technology progression of the last 20 years has re-energized the concepts. As a result, the number of noise radar designs and working prototypes is rapidly growing, as are the studies into its diverse applications. From its earliest concept, researchers of the noise radar boasted of several key features the most prevalent being its potential for high range resolution, excellent electronic protection (EP), low probability of intercept (LPI), and relatively simple hardware

architectures [20, 22, 24]. One of the earliest derivations of range resolution performance of the noise radar also exemplified its simplicity, as seen in the notional block diagrams in Figure 1. Using the joint correlation statistics of the transmit and receive signals, range resolutions on the order of meters were predicted [20]. The noise transmit waveform is potentially capable of attaining some of the highest resolution and lowest ambiguity of all waveforms, often alluded to having a “thumbtack” ambiguity, like that of the ambiguity diagram seen in Figure 2 [1, 2, 9, 33].

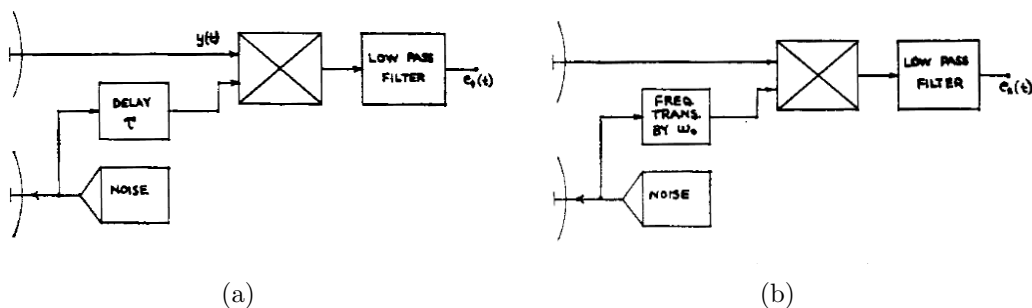


**Figure 1.** Notional noise radar block diagrams used in one of the earliest derivations of the theoretical range resolution performance using the concept of (a) time domain correlation or (b) frequency domain correlation to estimate target parameters (taken from [20]).

As the mainstream pulsed-Doppler design was advancing, early research into PRN codes was motivated by their reduced range sidelobes compared to other commonly employed pulse compression techniques, like the linear frequency modulated (LFM). The noise-like compression methods allowed significant enhancements in pulsed-Doppler radar range resolution. However, their periodic and relatively short sequences can be detected, identified, and exploited by electronic support systems. By lengthening the PRN sequences, the signal becomes less vulnerable to detection, but the monostatic’s duplexer limits the extents in range field of view with such long pulses [33]. As is discussed in the next section on recent research, the continuous UWB-RN waveform offers even greater LPI qualities than the longest periodic PRN sequence, along with its theoretically infinite unambiguous range and simultaneous high range reso-



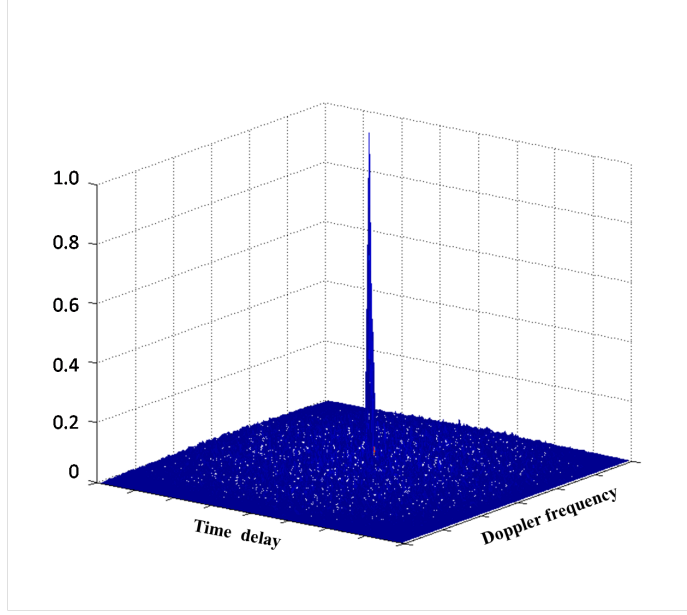


**Figure 2.** Ambiguity diagram depicting the ideal resolution and ambiguity qualities of a waveform, often referenced as the “thumbtack” [1, 2, 9, 33]

lution [39, 47].

The system bandwidth type described as ultrawideband (UWB) should be clarified. When the UWB descriptor is added to a radar system or waveform nomenclature, one can turn to a current standard for UWB radar definitions, IEEE Std 1672<sup>TM</sup>-2006. An UWB radar is a radar technology that simultaneously utilizes a band of frequencies spanning from hundreds of megahertz to higher radar frequencies. More specifically, it is characterized by transmission waveforms with a fractional bandwidth of 20%, as defined by the Federal Communications Commission (or 25% according to the US Defense Advanced Research Project Agency). Although agencies have different guidelines for classification of UWB, the formula for deriving the ratio of signal bandwidth to average frequency, that is, the signal’s fractional bandwidth,  $B_f$  has become standard. It is defined as [47]

$$B_f = 2 \frac{f_h - f_l}{f_h + f_l}, \quad (1)$$

where  $f_h$  is the highest frequency and  $f_l$  the lowest frequency in the transmitted signal. These spectral extents are determined by where the signal power rolls off by at least 10 dB with respect to the peak signal power.

#### 1.4.1.2 Recent Research.

A background on the noise radar is not complete without a synopsis of the most recent research published in the open literature. In the past 10 years, research into the noise radar technology has been conducted primarily on a single front - development and evaluation of various noise radar designs for special application areas. Kulpa *et al.* in “Signal processing in noise radar technology” summarize the the inherent EP advantage of a noise radar in context of the most current research areas [28]. Modeling and analysis of noise waveform’s covertness based on its structure and operational implementation was presented in [26]. Due to its potential high range resolution, radar imaging is a commonly researched application of the noise radar. It was demonstrated as a viable system for use in a radar cross section measurement compact range [49] and is capable of target identification and classification [52]. The extensive work of research teams at the University of Nebraska were instrumental in advancing the noise radar theory and technologies. By “injecting coherence” via a heterodyne receiver, a coherent UWB-RN radar capable of Doppler and polarimetric measurements was implemented [37]. Important discoveries were made in noise radar Doppler estimation and tracking performance metrics, including the derivation of a wideband ambiguity function specific to that radar design [9, 37, 60]. Additional research has applied the design to synthetic aperture radar (SAR) and inverse SAR imaging, as well as demonstrated capabilities in the areas of foliage and ground penetrating radar [16, 57, 58].

Advances in field programmable gate array (FPGA) and digital correlation pro-

cessing provides enhanced flexibility in pre-conditioning a digital transmit replica for specific feature extraction from the sensed environment [Walton - patent and private communication]. With a focus on the TTW capability of UWB in the lower Ultra High Frequency (UHF) band, a digital version of an UWB-RN radar was developed and successfully detects human activity through walls [30]. That research expanded into several micro-Doppler extraction studies [36] and a linear array of elliptic patch antennas with SAR capability, demonstrating indoor TTW tracking of human target motion [53]. Following the design of the digital implementation in [30] and leveraging the inherent EP of simultaneously operated UWB-RN radar, a network of three UWB-RN radars was developed at AFIT. A series of experiments demonstrated a TTW sensing capability. Furthermore, successful triangulation (as seen in Figure 3) of both stationary and moving targets was achieved with that network of monostatic UWB-RN radars [43]. Finally, mathematical models of multi-channel noise radar have been proposed to study specific issues like optimized beamforming designs [21], as well as ground clutter cancellation techniques [29]. A basic understanding of multi-channel concepts requires a brief background on multistatic radar.

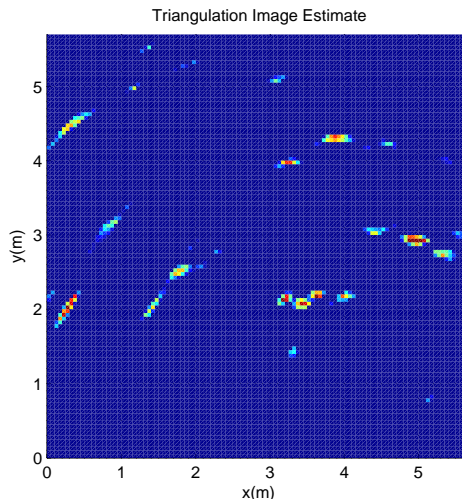


**Figure 3. Demonstrated detection and estimation of human targets using a network of three monostatic UWB-RN radars at AFIT [43].**

## 1.4.2 Multistatic Radar Systems.

### 1.4.2.1 Definition and History.

Many of the earliest radars in history were single frequency continuous wave (CW) bistatic systems, where the receiver was spatially separated from the transmitter. When duplexer technology enabled shared use of a single antenna for transmission and reception, advancements in radar theory were dominated by the monostatic design. Likewise, the research in monostatic radar led engineers to the numerous benefits of the pulse modulated waveform. In an early comparative assessment of monostatic and bistatic radar, Skolnik cites only three possible benefits to the bistatic configuration, namely (1) exploitation of the enhanced forward scatter region of a target's bistatic Radar Cross Section (RCS), (2) potential reduction in number of systems required for a fence-like detection network, and (3) simplifications in hardware components like the radar's duplexer, which is generally not required for bistatic operations [44]. Overall, his final analyses concludes that for target detection and location purposes the monostatic design is superior. With its additional communications overhead and generally reduced resolution capability, bistatic radar research was overshadowed by the greater interest in advancing monostatic performance [44].

According to [55], there have been three re-emergent periods of critical bistatic research, with the most recent driven by successful prototypes of passive bistatic radar systems. Supported by a pre-existing infrastructure of over-the-air communication transmitters and further motivated by speculations of a counter-stealth capability, research focused on the advantages and limitations of cooperative and non-cooperative bistatic radar networks [55]. With this came studies into a variety of possible waveforms for bistatic and multistatic networks, including UWB.

The IEEE standard provides a usable definition of the UWB multistatic radar. Concisely stated, it is an UWB radar with one transmitter and a network of multiple

receivers stationed at different geographical locations for enhancing performance. A multistatic radar system is characterized by a netted group of cooperative transmitters and receivers using multiple monostatic and bistatic channels to perform a detection, localization, or identification mission. Because a complex target/clutter environment often contains numerous duplicate signal paths or multipath channels, it is important to define what is meant by a *channel*. As depicted in Figure 4, a channel is the path in which the signal propagates from a transmit antenna directly to a target and is scattered directly to a receive antenna. All other paths of signal propagation are undesired and considered as interfering signal paths. A channel is specified by its type of link, that is, whether it is a monostatic or bistatic channel. A multistatic radar system is often comprised of both types of channels.

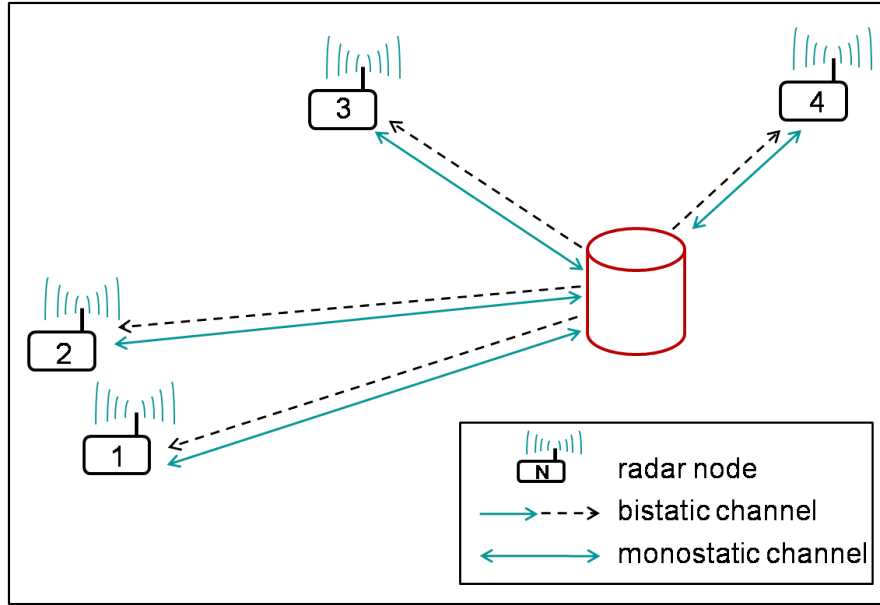


**Figure 4. Depiction of the two types of channels formed by transmitter-target-receiver signal paths that make up a multistatic radar network.**

The radar community has borrowed other nomenclature from the communications field for various types of multistatic architectures. Some researchers use the previous definition to describe the single-input, multiple-output multistatic system, which distinguishes it from systems having two or more transmitters, a design commonly

known as multiple-input multiple-output (MIMO). The architecture of a distributed sensor system is tied directly to the type and fidelity of information it must provide. For US defense systems, this is the sensor's concept of operations (CONOPS). It defines a sensor or sensor group's functionality in context of the operational need and accounts for things like the joint coverage area, terrain, target profiles, and other mission-specific hardware considerations [41]. Ultimately, the CONOPS drives the fusion architecture requirements, including exact numbers of transmitter-receiver pairs necessary to perform the distributed sensing purposes of a mission.

Besides number of transmitters and receivers, a multistatic radar is often described by the amount of inter-nodal communication, synchronization and distributed signal processing it employs. The most prevalent types include: non-coherent and coherent MIMO, decentralized multistatic, rephased MIMO, and netted monostatic [13, 34]. While a great variety of processing architectures exist, they can be grouped on the primary function governing their data fusion rules. In general, the fusion rules are optimized for distributed detection or distributed estimation of potential targets in their joint coverage area [51]. While target localization performance within the distributed estimation problem is of specific interest in this thesis, the overall enhanced performance afforded by multistatic architectures provides necessary background.

Of the open technical literature reviewed, the enhanced performance aspects of the multistatic radar design fall into two overarching categories. The first (and more intuitive) is the added performance afforded by a multistatic design via system redundancy. The performance of a well designed network of receivers degrades more gracefully than the non-networked system. The slow degradation might manifest as small holes in radar coverage extents or fewer layers in a joint coverage area, as opposed to entire sectors of coverage [4]. This is linked to the critical feature expressed in defense applications as enhanced survivability. Two commonly cited survivabil-

ity examples are EP against electronic attack systems and defense of anti-radiation weapons [5, 55]. The basic premise is simple. In a multistatic system, only the RF emissions of a transmitter are detected by the direction finding sensors of the jammer or weapon. With multiple receivers dispersed away from the transmitter, the overall system survivability from attack is enhanced. This also allows greater flexibility in positioning receiver stations farther forward in an integrated threat coverage area as seen in Figure 5 [5]. The underlying assumption being that any unintended RF emission of the receiver is indiscernible by the adversary's sensor suite. For clarity, these enhanced survivability aspects of the multistatic radar are separate from and adds to the LPI features of the noise radar.

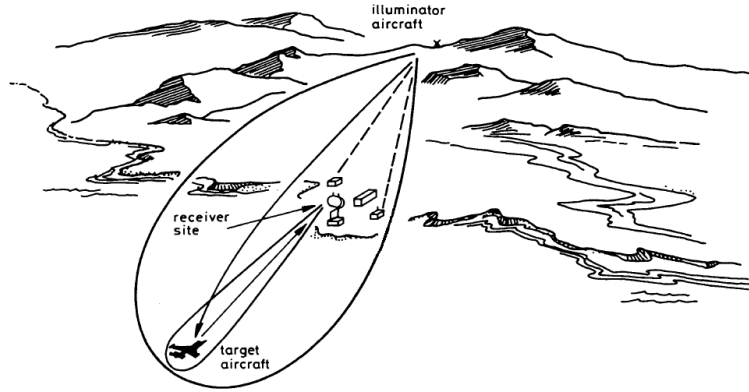


**Figure 5. Graphic depicting the coverage area and survivability concepts provided by a multistatic radar architecture(adapted from [5]).**

The second enhancement deals specifically with potential distributed detection and distributed estimation gains. Some gains relate purely to a system's coverage area, in which additional receivers are strategically placed to extend the maximum detection range of the system. Other gains exploit the spatially unique observations of a target provided by the multistatic geometries of the engagement. Over fifty years ago, the forward scatter phenomenon, which significantly enhances the RF signature of a target at bistatic angles near  $180^\circ$  was discovered and has been exploited in several multistatic designs [18, 55]. Recent research on noncoherent MIMO investigates

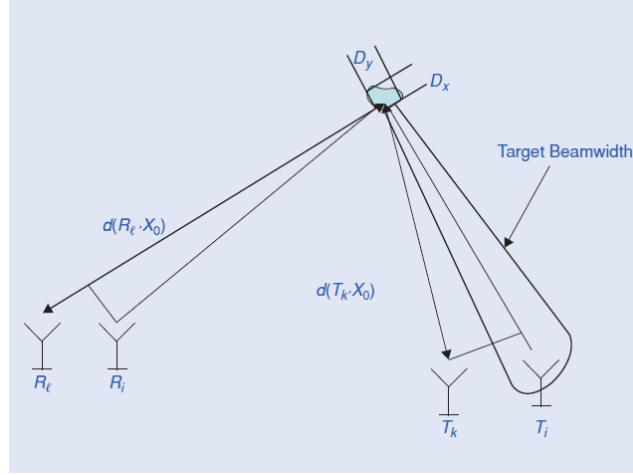
a statistical diversity gain available to systems with widely separated antennas performing a distributed detection mission. Similarly, the potential improvements in distributed estimation, is a topic of recent research in multistatic radar.

#### 1.4.2.2 Recent Research.

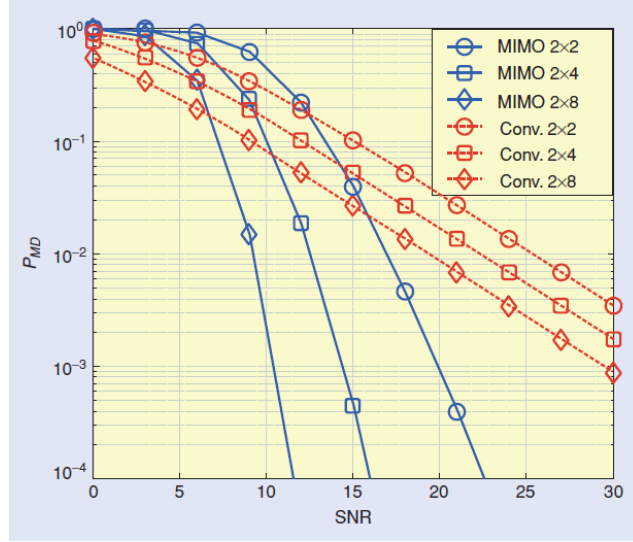
Research is mounting on the diversity gain offered by certain multistatic radar architectures, particularly those having a multi-transmitter, MIMO design. When widely distributed antenna are operating as a MIMO radar system, research shows a noncoherent signal gain is realized, if there exists adequate spatial decorrelation of the independent measurements with respect to the target's RCS distribution [14]. Figure 6(a) pictures the scenario in which spatial decorrelation is attained for a given detection engagement and Figure 6(b) shows the modeled improvement in terms of a reduction in probability of missing detection of a target. Based on the research, diversity gain improvements in the multistatic system as compared to conventional phased array antenna systems occur specifically for coverages where reduced levels of available SNR exist.

Other recent research deals more specifically with issues of multistatic target location estimation. Figure 7(a) shows the simulated results of a 2 transmitter-receiver pairs operating as a multistatic system [11]. In the simulation, the system clearly resolves in cross-range the two targets that exist at 120 meters downrange (y-axis). However, many centrally processed images using actual experimental multistatic systems result in target ghosts. A target ghost, like that seen in Figure 7(b) is due primarily to the aggregate spatial ambiguities and dynamic range resolutions of the monostatic and bistatic channels' downrange estimates [11]. A variety of two stage processing algorithms exist that can aid in the removal of such target ghosts. As seen in Figure 7(c), use of a first-stage decentralized threshold followed by a second-stage





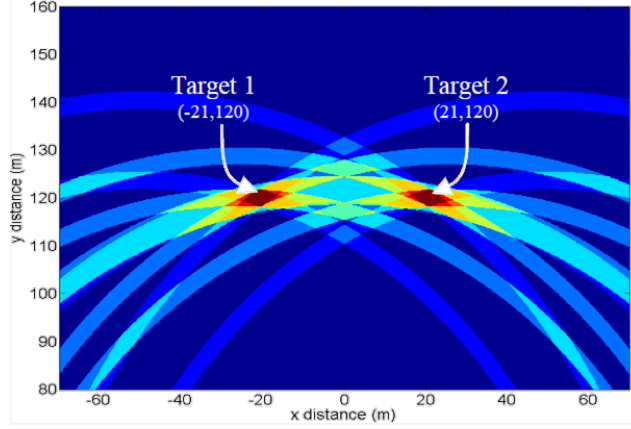
(a)



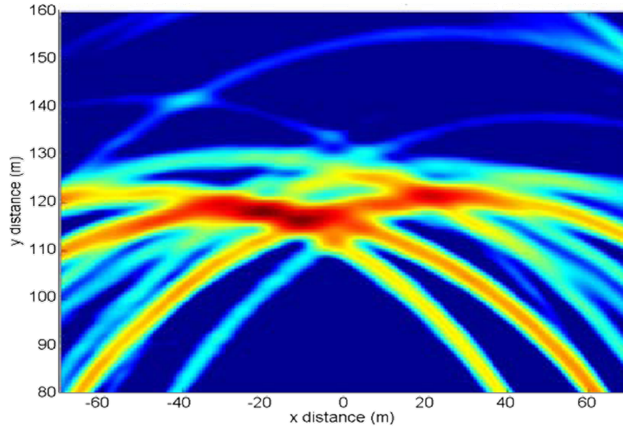
(b)

**Figure 6. (a) Adequate spatial decorrelation in the multistatic receive signal results in (b) a diversity gain due to the independent measurements of the target and a corresponding reduction in probability of missed detection as compared to equivalent power phased array configurations (reproduced from [14]).**

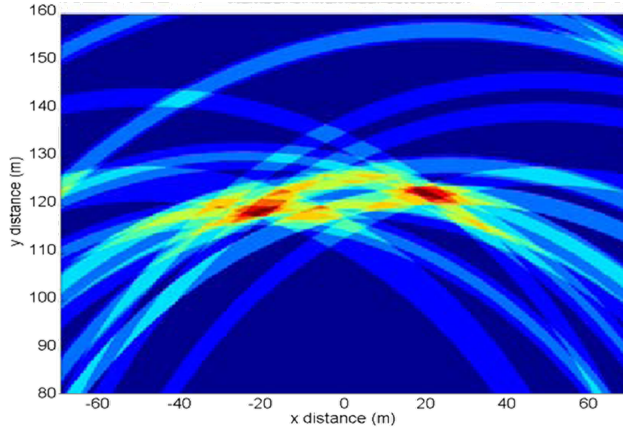
CLEAN algorithm effectively removes the target ghost from the true targets, which are now resolvable [11]. There is, however, a residual range error associated with the left target that could not be corrected in the post-processing. The results demonstrate the importance of choosing proper types and ordering of multistatic image post-processing.



(a)



(b)



(c)

Figure 7. Results of a two target cross-range resolution experiment where (a) simulated images show two clearly resolved targets, (b) central processed experimental data results in loss of resolution and a target ghost, and (c) an experimental result using first-stage thresholding and second-stage CLEAN processing to remove the ambiguity causing the target ghost (reproduced from [11]).

## II. Theory

### 2.1 Chapter Overview

The purpose of this chapter is to form a consolidated picture of the underlying theory, design attributes, and mathematical models relevant to designing and evaluating the individual performances of the noise radar and multistatic network of noise radars. Discussions of the transmitter and receiver designs include the fundamental analysis tools for each. The ambiguity function details the waveform design and associated range resolution performance parameter. It along with the theoretical signal-to-noise ratio (SNR) analysis provides a means of estimating the performance of the direct-conversion correlation signal processing implemented in the receivers, and ultimately their localization accuracy. The multistatic data fusion processing requires understanding of the monostatic and bistatic and subsequent design of experiments. The multistatic geometries extend the performance metrics to 2-dimensions. Finally, the general multistatic signal model completes the underlying theory for system operation used in the development of the signal and data processing software, as well as predictions of system performance.

### 2.2 Transmitter Theory

#### 2.2.1 Continuous Random Noise.

The most common monostatic radar uses a pulsed radio frequency (RF) waveform to measure the time delay between transmitting the pulse and reception of the target/environment-reflected pulse. Therefore, by converting the measured time delay scale to range scale using the known speed of electromagnetic (EM) propagation in free-space, the sensed range,  $R$ , is given by

$$R = \frac{1}{2}c\tau \quad (2)$$

where  $c$  is equal to the speed of light and  $\tau$  is the measured two-way time delay of the pulsed RF signal. The transmitter used in the AFIT NoNet radar is designed to emit a continuous RF noise signal, placing it in the category of the continuous wave (CW) radar. In order for a CW radar to measure range, the transmit signal must be imprinted with some measurable code or modulation scheme used for estimating the two-way time delay of the received signal [33]. While conventional CW waveforms, such as the periodic linear frequency modulated CW waveform, are deterministic, the AFIT NoNet radar uses a truly random code by transmitting the RF output of a solid-state thermal noise generator. Originally discovered by Johnson and thereafter explained by Nyquist, thermal noise is a result of the variance in electron conduction caused by temperature induced agitations within the conducting material. A thermal noise random process is best described by its statistical behavior, often summarized by the descriptors white and Gaussian. White Gaussian thermal noise is nearly uniform in its power spectral density (PSD), though with some non-uniformity at the high optical frequencies. Temporally, it conforms to the Central Limit Theorem and its second-order statistics further classify it as a wide-sense stationary random process. It has a root mean square (RMS) voltage,  $n_t$  given by [23]

$$n_t = \sqrt{4k_B T r B}, \quad (3)$$

where  $k_B$  is Boltzmann's constant ( $1.381 \times 10^{-23}$  joules per Kelvin),  $T$  is the absolute temperature in Kelvin of the conductive equivalent load,  $r$  (in Ohms), over a defined noise bandwidth  $B$  (in Hertz). While it is conventional to represent the RMS noise voltage and average noise power using  $\sigma$ , the  $\sigma$  symbol is reserved for a target's radar

cross-section (RCS).

The two key elements of thermal noise exploited in the multistatic UWB-RN radar are its inherent broadband (though band-limited) and stochastic qualities. The remainder of this section expounds the theoretical details of each. Ambiguity theory is introduced first however, due to its fundamental importance in analyzing the theoretical performance limits of a radar waveform.

### **2.2.2 Radar Ambiguity Function.**

For all radar waveform designs, certain trade-offs exist in the signal structure. From a signal processing perspective, the critical properties of a signal's time-bandwidth product, periodicity, and the underlying modulation structure are critical in specifying the theoretical parameter estimation performance bounds of the system. The receiver processing of the designed waveform then delivers the actual performance levels in terms of range and velocity detection and estimation metrics. These performance metrics include the radar's measurement of target range and velocity in terms of unambiguous coverage extents, accuracy, resolution, and tolerance. Although this research focuses specifically on the range accuracy and resolution performance metrics, all are linked in the waveform/system design. In fact, radar engineers analyze the time-delay, Doppler shift and mutual coupling characteristics of the waveforms with a single analysis tool. Using the radar ambiguity function (AF), the magnitudes, locations and shapes of both range and velocity uncertainties, or ambiguities, are simultaneously evaluated. Not only does the AF allow visualization of waveform performance and associated trade-offs, but the output of the AF is also used in the mathematical derivations for computing a radar's theoretical range resolution and range accuracy.

Originally formulated by Woodward to compare resolution performances of various

waveforms, the AF models the output of a matched filter by expressing its time-Doppler dependencies due to the temporal and spectral structure of the waveform [56]. The information contained in an Ambiguity Diagram graphically details the impacts of time delay offsets and target Doppler shifts, again from the perspective of an ideal matched filter. Therefore, the model of the matched filter output,  $g(t)$ , is a common starting point in the AF derivation. Let a point target response of a transmitted signal that is  $t$  time-delayed and  $f_d$  Doppler-shifted be expressed as [38]

$$g(t) = \int_{-\infty}^{\infty} s(x) s^*(x - t) e^{j2\pi f_d x} dx, \quad (4)$$

where  $s^*$  denotes the complex conjugate of the waveform of interest described by the time dependent signal  $s(x)$ . The time-reversed version of Equation (4), where  $t$  is replaced with  $-\tau_d$ , is precisely the correlation of  $s(x)$  (often referred to as the time-frequency autocorrelation function (TFACF)) and is given by [33, 41]

$$\chi(\tau_d, f_d) = g(-\tau_d, f_d) = \int_{-\infty}^{\infty} s(x) s^*(x + \tau_d) e^{j2\pi f_d x} dx. \quad (5)$$

Finally, the ambiguity function can be defined as the squared magnitude of this time-frequency autocorrelation function, that is,  $|\chi(\tau_d, f_d)|^2$  [33, 38]. Figure 8 shows the waveform ambiguity diagram, a common form of the AF output. Here, the AF is computed for a 15-bit pseudorandom binary phase coded waveform.

Explorations into the various utilities of the delay-Doppler AF are extensive [6, 33, 56]. Here, it is used to present the theory behind implementing a random noise signal

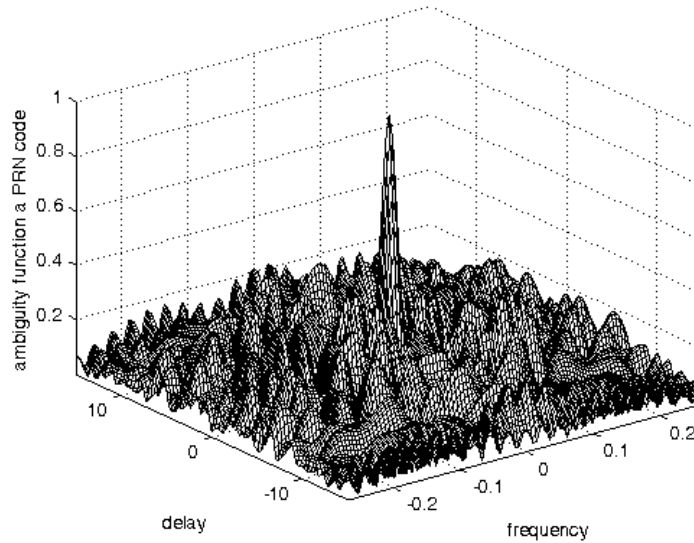


**Figure 8.** The Ambiguity Function output of a 15-bit pseudorandom binary phase coded waveform depicted in a delay-Doppler ambiguity diagram (reproduced from [35]).

as a radar transmit waveform. This rationale is primarily based on the waveform’s potential for high range resolution, low error variance in its accuracy, inherent LPI characteristics and spectral orthogonality qualities making it well-suited for covert, multistatic operations [15].

### 2.2.3 Range Resolution with UWB Random Noise.

As the *UWB* and *continuous random noise* transmit signal characteristics imply, a broadly spread spectrum processed for relatively lengthy durations is analogous to the large time-bandwidth products that conventional pulse compression techniques are designed to offer. In theory, thermal noise used as the signal source has infinite bandwidth, that is, the random oscillations of electron carriers can and do occur at all measurable frequencies [23]. Measurements must be taken for finite bandwidths due to physical constraints of hardware. Similarly, the noise radar is band-limited by design (using band-pass filters and other band-limited hardware), both in the receiver hardware chain and the transmitter and transmit replica chains. The following

theory derives how a radar's range resolution, one of the most critical characteristics describing its imaging performance, rests in the occupied bandwidth,  $B$ , of the radar waveform.

Woodward was first to formulate the “time resolution constant”, a well-known application of the radar AF. To simplify the computation of the time resolution constant, a zero-Doppler cut of the TFACF is taken, which makes it simply the time autocorrelation function (ACF). Again using the example of the pseudorandom binary phase coded waveform, Figure 9 shows the graphical representation of the ACF. This is similar to the projection of the TFACF of a highly Doppler-tolerant waveform, which short-pulse UWB waveforms are known to be. Another physical interpretation occurs when the target of interest is stationary [6] relative to the radar. When this  $f_d=0$  condition is satisfied, the time resolution constant,  $T_R(0)$ , is given by [56]

$$T_R(0) = \frac{\int_{-\infty}^{\infty} |\chi(\tau, 0)|^2 d\tau}{|\chi(0, 0)|^2}. \quad (6)$$

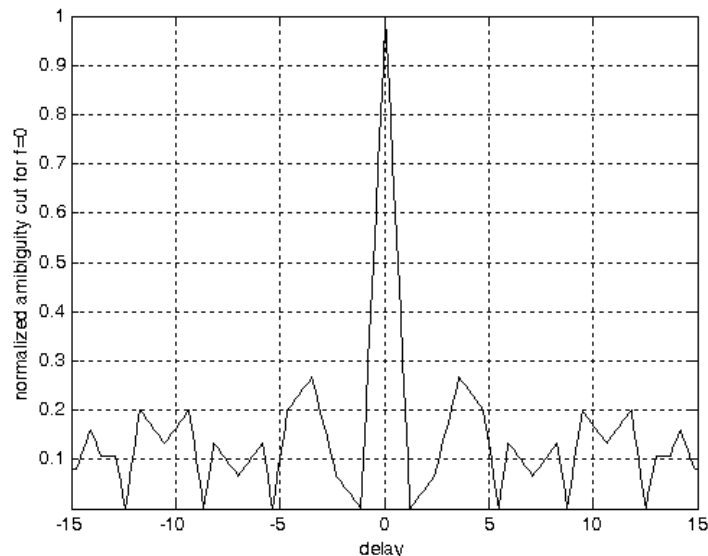


**Figure 9.** The zero-Doppler, Autocorrelation Function output of a 15-bit pseudorandom binary phase coded waveform (reproduced from [35]).



Woodward's theory explains that the smaller the time resolution constant, the greater the inherent potential of the waveform for discriminating between two targets via a time delay measurement of return signals. Using Parseval's theorem, which states that the total energy,  $E$  associated with a real signal,  $s(t)$ , is

$$E = \int_{-\infty}^{\infty} |s(t)|^2 dt = \int_{-\infty}^{\infty} |S(f)|^2 df. \quad (7)$$

Therefore, Equation (6) can also be formulated in terms of the signal's spectrum,  $S(f)$ , which means the time resolution constant becomes [56]

$$T_R(0) = \frac{\int_{-\infty}^{\infty} |S(f)|^4 df}{\left[ \int_{-\infty}^{\infty} |S(f)|^2 df \right]^2}. \quad (8)$$

Using the calculus of variations, Cook and Bernfeld show that the smallest  $T_R(0)$  is attained from waveforms that uniformly fill a large band with uniform magnitude, much like the UWB-RN signal [56]. It also reduces  $T_R(0)$  to simply the inverse of the occupied bandwidth or  $\frac{1}{B}$ . Therefore, the signal bandwidth determines the theoretical lower bound of the time resolution constant. As a result, a monostatic radar's ability to discriminate two targets due only to downrange separation is bounded from below by [46]

$$\Delta R = \frac{c}{2B}, \quad (9)$$

where the monostatic range resolution,  $\Delta R$ , now accounts for the two-way time delay, and  $c$  is the speed of EM propagation through the assumed homogeneous medium of free-space.

Besides the time resolution constant, another important design factor given by the ACF is based on the size, shape and location of the waveform dependent range sidelobes. Ambiguity arises when energy in the range sidelobe of a target response

results in a false target or when that energy masks the presence of a smaller target that is nearby. Mitigation of range sidelobe errors is a primary driver in waveform design as well as the focus of many signal processing techniques performed in the receiver.

#### 2.2.4 Correlation of UWB Noise.

The model of the ACF can also be applied to analysis of stochastic signals, such as UWB thermal noise. Described as random processes that are wide-sense stationary, zero-mean, and Gaussian, the joint behavior of a pair of thermal noise signals  $X$  and  $Y$  is best described by their second-order joint moment,  $E[XY]$ , where  $E$  is the expected value [32]. This joint statistic is most commonly referred to as the *cross-correlation* of  $X$  and  $Y$ , which hereafter is denoted by  $R_{XY}$ . Because they are zero-mean processes,  $R_{XY}$  is said to be centered, and is therefore equivalent to the covariance of  $X$  and  $Y$ . Furthermore, a correlation coefficient  $\rho$ , which simply normalizes the already centered  $R_{XY}$ , can be used to quantify from 0 to 1 the degree of correlation between the two random processes, with 0 being perfectly uncorrelated [23]. One of the primary goals in MIMO multistatic radar waveform design is waveform decorrelation in the shared coverage area. When the correlation of two random processes approaches 0, their spectra are said to have the quality of orthogonality. Orthogonality by design, minimizes the average cross-power spectral density of the signals in a receiver processor [34]. A key feature of large time-bandwidth signals is their potential for very low cross-power spectral densities - the quality inherent in UWB random noise. In the next section, the utility of cross-power spectrum estimation forms the basis of the receiver processor theory and is ultimately exploited in the AFIT NoNet multistatic design.

### 2.3 Receiver Theory

The standard in radar receiver processing is the super-heterodyned matched filter. In a conventional pulsed-Doppler radar, this process uses narrowband analog amplifiers, mixers and filters designed to precondition the signal for the matched filtering. The noise radar receiver design takes a quite different approach, one that is modeled closely after the software defined radio. Rather than heterodyning and matched filtering, the AFIT NoNet radar receiver is based on the concepts of direct-conversion and digital correlation as seen in the block diagram in Figure 10. This section provides the general theory on correlation processing and how it is implemented in the design. The focus is on the key elements leading to design of experiments and subsequent performance analysis of the system's range accuracy.

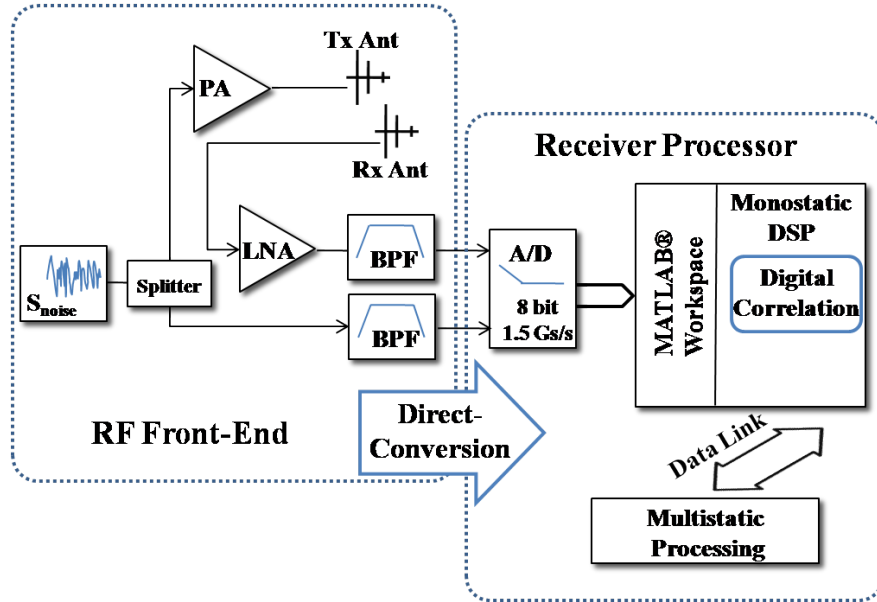


Figure 10. Block Diagram of the noise radar node detailing the receiver's direct-conversion, digital correlation design.

### 2.3.1 Direct-Conversion.

Direct-conversion to a digital signal format simultaneously simplifies the design while expanding the flexibility of the receiver processing, following the concept of the software defined radio [50]. The direct-conversion concept bypasses the typical super-heterodyne receiver architecture, which mixes the receive signal with coherent oscillators and stationary local oscillators one or more times before A/D conversion [12]. Likewise, the noise radar receiver design does not use the standard in-phase and quadrature channels created by the hybrid splitter and dual mixer architecture in many coherent receivers. The theory is that limiting the amount of RF front-end hardware not only reduces the complexity of receiver calibrations, it removes the undesired noise inherent with in-phase/quadrature channel imbalances and drifts in the reference oscillator's phase. Minimizing the number of components also increases the reliability of the overall system. Finally, minimal analog processing of both the received and replica UWB signals, reduces the UWB signal distortions caused by dispersive RF components.

As detailed in Figure 10, the 3.0 Giga-samples per second (GSa/s) analog-to-digital conversion (A/D) is interleaved to sample each channel at 1.5 GSa/s. With the two-channel mode implemented in the current design, the A/D meets the highest frequency Nyquist-rate constraint covering the DC to 750 MHz spectral band. Besides the maximum sampling rate bounding from above the usable bandwidth, the A/D also determines the key radar receiver performance parameter of dynamic range. The dynamic range is best understood in context of the overall operating environment, so it is addressed in the calibration methodology section of Chapter III. The band pass filter (BPF) is designed for a half-power bandwidth of approximately 400 MHz on each signal channel. The high pass side of the BPF serves as the anti-aliasing filter, the low pass of the BPF mirrors the lowest passed frequency of the antenna, which

is approximately 400 MHz. The primary purpose of these filters is to condition the transmit replica and received signal spectra prior to conversion and correlation processing. Note that multiple low noise amplifiers (LNA) are used to amplify the signal prior to transmission and immediately upon reception. With only minor variations, this direct-conversion design is a replication of the Pennsylvania State University noise radar design, as documented in [30].

Critical to a comprehensive understanding of the direct-conversion design is the internally generated receiver noise that corrupts the received signal. This noise figure limits many of the overall radar performance metrics, particularly the radar's measurement accuracy. The statistical characteristics of the receiver's thermally generated noise are identical to those presented in the transmitter theory. Therefore, the RMS noise voltage,  $n_t$ , computed in Equation (3) applies to each of the components in the total cascaded receiver noise figure. Because the A/D noise is a combination of its thermal and quantization noise, discussion of the noise figure requires an overview of quantization noise theory.

Quantization noise is the direct result of the error between the digital and continuous time representations of the analog signal. Based in part on the number of discrete quantization levels (or bits) of the digitizer, the distribution of the quantization noise also depends on the input signal's amplitude distribution and spectral characteristics (unlike other thermal noise which is not generally a function of the input signal itself).

For the noise radar receiver, understanding both the distribution and cross-correlation of the quantization error for each digital signal channel is critical. The quantization noise not only corrupts each signal, lowering the correlated target response, but any coloring or deterministic features in the noise can produce undesired high cross-correlations between two signals. As a result, the correlation receiver's noise floor

is elevated, reducing the available SNR for target estimation purposes, and potentially increasing the probability of false alarms. However, if adequately uncorrelated, the coherent and non-coherent integration methods employed in the digital signal processing would reduce quantization noise in a similar manner to that of the white Gaussian thermal noise.

The quantization noise spectrum for a band-limited, white Gaussian input signal has been analyzed and presented in [54]. According to Widrow and Kollár the PSD,  $S_q$ , of the quantization noise for such a signal can be modeled as [54]

$$S_q \approx \frac{q^2}{4\pi^3 B} \sqrt{\frac{3\gamma}{2\pi}} \eta \left( \frac{3\gamma f^2}{8\pi^2 B^2} \right) \quad (10)$$

where the input signal of bandwidth  $B$  is quantized at a quantum size,  $q$ , and  $\gamma$  is the quantum size normalized by the input signal's mean power (or  $\gamma = q^2/\sigma_x^2$ ). The power series expansion term,  $\eta$ , is defined as [54]

$$\eta(y) = \sum_{n=1}^{\infty} \frac{e^{\frac{-y}{n^2}}}{n^3}.$$

As seen in Figure 11, for our bandwidth normalized frequency range of interest (nominally from 1.8 to 4.0 on the plotted x-axis scale) a white-like quantization noise spectrum is estimated. This flat region of the model output along the 8-bit curve is based on a white Gaussian input signal of mean power,  $\sigma_x^2$ , where the  $-4\sigma_x$  to  $4\sigma_x$  levels of the input signal are equivalent to the full input dynamic range of the A/D. In other words, the signal is “filling” the dynamic range with approximately  $8\sigma_x$  of its energy, which is an effective use of all available bits for this type of input signal. Note the sloping tail in the plot, showing that even the 8-bit quantization noise becomes dispersive (i.e. colored) at higher relative frequencies or for narrower relative bandwidths. Assuming then that such input signal conditions exist, the quantization

noise is nearly white, and as a result, uncorrelated.

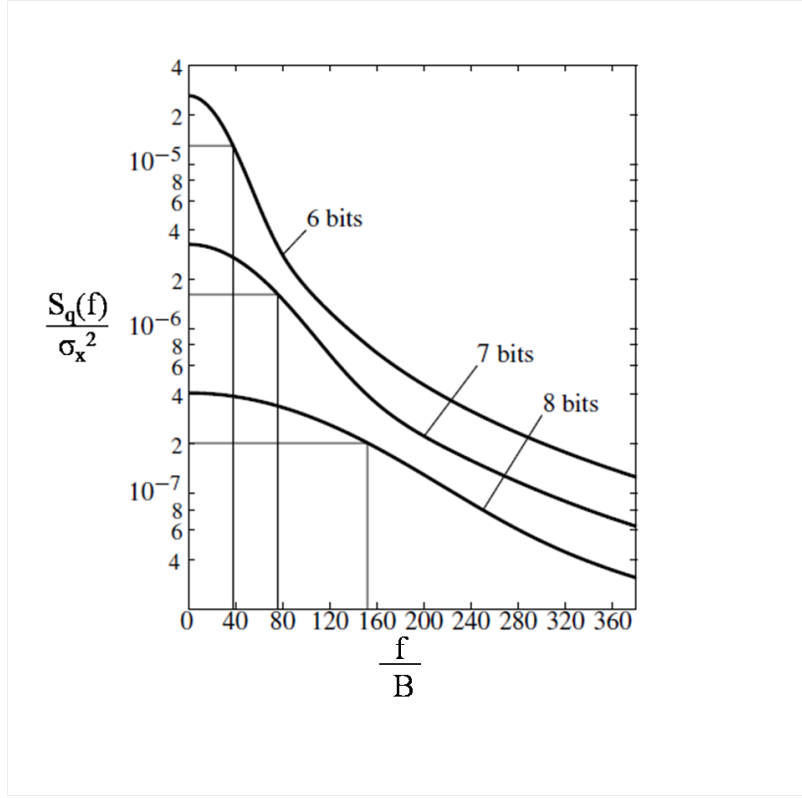


**Figure 11.** Normalized quantization noise spectra modeled for various A/D bits using Equation (10). The model variables are specified by a white Gaussian input signal of mean power,  $\sigma_x^2$  and quantized across an A/D with nominal dynamic range of  $-4\sigma_x$  to  $4\sigma_x$ . (reproduced from [54]).

Based on these theories, the RMS voltage,  $n_q$ , of the uncorrelated quantization and thermal noise will simply add as a cascaded network to the other receiver thermal noise RMS voltages in the total receiver noise figure [46]. The critical theoretical conclusion is that the quantization noise spectra of the A/D will have near-uniform power spectral density. Consequently, it should not be a source of any erroneously high cross-correlations in the measurements. These theoretical assumptions will be tested in the system characterization measurements in Chapter III, where the multiple channel output signals of the A/D will be analyzed using estimates of their auto and cross correlations.

### 2.3.2 Digital Correlation.

In a correlation receiver, the received input signal is convolved with a delayed replica of the transmitted waveform. One of the most powerful tools in signal processing is the use of the Fourier Transform property of convolution, depicted in its discrete form in Figure 12. Essentially, the property allows computation of time-domain signal convolution via complex signal multiplication in the frequency domain. Because the transmit signal,  $s(t)$  and received signal  $r(t)$  are jointly wide-sense stationary processes, their cross-power spectrum,  $S_{sr}(f)$  can be approximated using their discrete Fourier Transform (DFT) spectra such that

$$S_{sr}[k] = S[k] R^*[k], \quad (11)$$

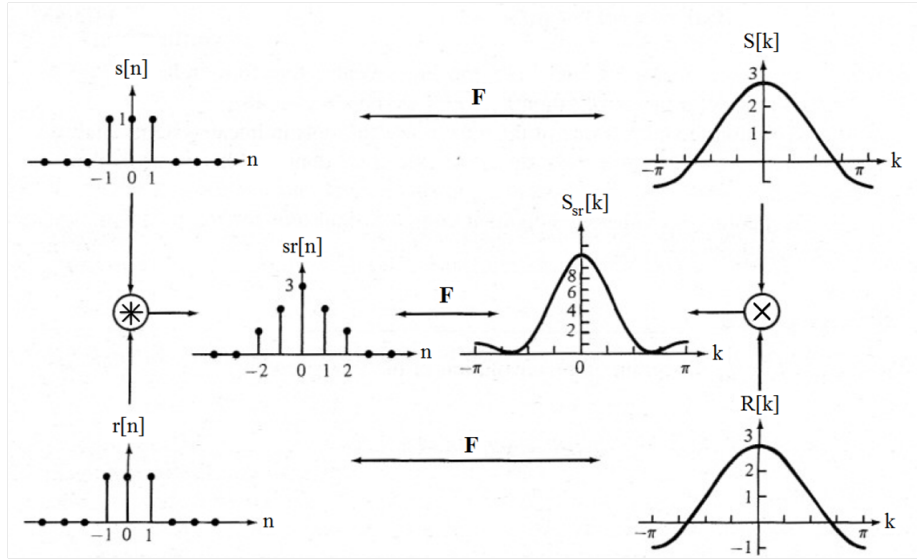


Figure 12. Graphical Representation of the Fourier Transform property of convolution adapted from [40].

where the  $*$  denotes the complex conjugate. In a digital correlation receiver, the Nyquist satisfied spectral estimates of the transmit and receive signals for  $N$  length records tested at each frequency,  $k$ , spanning the double-sided Nyquist bandwidth



are given by

$$S[k] = \sum_{n=0}^{N-1} s[n] e^{-\frac{j2\pi nk}{N}} \quad (12)$$

and

$$R[k] = \sum_{n=0}^{N-1} S[n] e^{-\frac{j2\pi nk}{N}}, \quad (13)$$

respectively. Based on the Wiener-Khintchine-Einstein Theorem, one valuable utility of obtaining the cross-power spectral estimate of the transmit and receive signals (as seen in Equation (11)) is computing the discrete cross-correlation,  $R_{sr}[n]$  given by [23]

$$R_{sr}[n] = \frac{1}{N} \sum_{k=0}^{N-1} S_{sr}[k] e^{\frac{j2\pi nk}{N}}, \quad (14)$$

that is, the inverse discrete Fourier Transform (IDFT) of their cross-power spectral density estimate. As was shown in the radar AF section, the  $R_{sr}[n]$  output of this correlation process is also a time-reversed version of the matched filter operation. Therefore, the AFIT NoNET processor mimics in its design the very correlation algorithm used to assess a waveform's performance bounds as defined by the AF.

With its reduced processing time and ease of implementation in the MATLAB<sup>®</sup> environment, the DFT and IDFT are computed using the Fast Fourier Transform (FFT) and Inverse Fast Fourier Transform (IFFT), respectively (as depicted in Figure 13). Reference to this digital signal processing, specifically for radar applications, is detailed by Mahfza and Elsherbeni in [35]. There, it is defined as a form of synthetic ranging by means of the fast convolution process. This exact algorithm is the primary digital signal processing (DSP) routine performed using MATLAB<sup>®</sup> in the AFIT NoNET design. Using the *xcorr* function, an unbiased, cross-correlation  $R_{sr}[n]$  is estimated for target localization in the time domain. This DSP is part of the distributed processing performed at each radar node to compute its monostatic channel response, whereas

bistatic channel cross-correlations are estimated by the central processor.

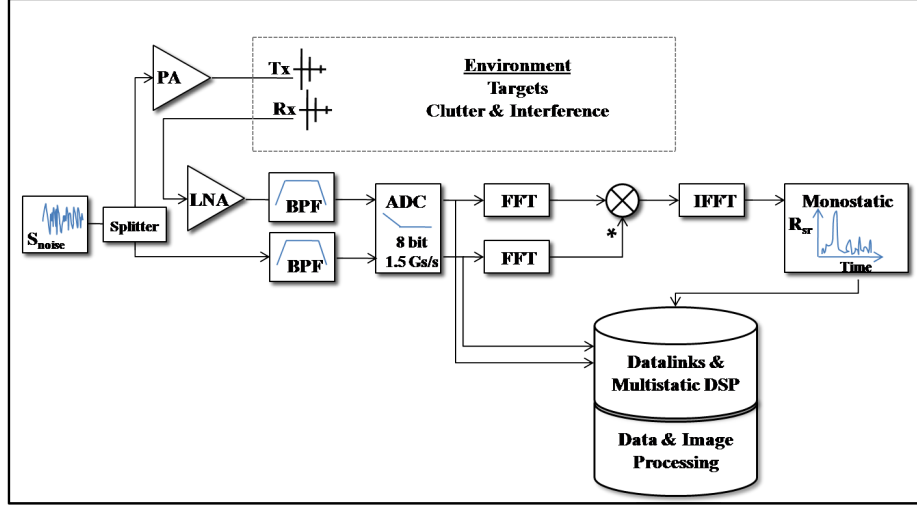


Figure 13. AFIT NoNET radar system block diagram including the cross-correlation DSP which details the spectral estimation method of ranging.

### 2.3.3 Theoretical Range Accuracy.

Borrowed from information theory, the Cramér-Rao Lower Bound (CRLB) is a common method used in estimating various theoretical performance limits of sensors, including radars. By choosing a single measurement parameter of an unbiased estimator,  $\tau$  (here set as the two-way time delay to a target) the CRLB estimates the lowest attainable variance in the error of that time delay measurement for a given system. The CRLB is an application of the Fisher Information Matrix (FIM), which defines the estimation fidelity of a set of desired parameters, based on the measurement's orthogonal sensitivity to a set of nuisance, that is, interfering parameters. Specifically, this lower bounded inequality of the error variance is the inverse of the determinant of the FIM,  $|J(\Phi)|^{-1}$ , such that [42]

$$CRLB = E [(\hat{\tau} - \tau)^2] \geq \frac{1}{|J(\Phi)|}, \quad (15)$$

where  $\Phi$  is a vector of the parameters to be estimated. If  $z(\Phi)$  is the measured

data taken by the system, it is assumed to be corrupted by various sources and types of interference, like clutter, internal thermal noise, or even external jamming signals. Because the FIM is the expected sensitivity of the measured data's probability density,  $p(\mathbf{z}(\Phi))$  with respect to a change in the parameters of interest, it can be modeled as [42]

$$J(\Phi) = E \left[ \left( \frac{\partial}{\partial \Phi} \log p(\mathbf{z}(\Phi)) \right) \left( \frac{\partial}{\partial \Phi} \log p(\mathbf{z}(\Phi)) \right)^T \right]. \quad (16)$$

Bernfeld and Cook point out the obvious complication in Equation (16), which requires the *a priori* probability density functions of the parameters being estimated in the measurement [6]. However, it is often valid to assume the aggregate of all interferers be modeled as zero mean white Gaussian noise (as is the case for a radar receiver that is thermal noise limited). Therefore, when envelope detection from a matched filter is employed, the theory presented in [6] reduces the error variance model for a monostatic time-delay measurement into the form

$$E[(\hat{\tau} - \tau)^2] \geq \frac{1}{B_{rms}^2 (2E/N_o)}, \quad (17)$$

a relationship with two known measurement attributes: the signal energy to noise spectral density ratio,  $E/N_o$  and an RMS bandwidth parameter,  $B_{rms}$ . The signal's  $B_{rms}$  is defined by [2]

$$B_{rms} = \sqrt{\frac{\int_{-\infty}^{\infty} (2\pi f)^2 |S(f)|^2 df}{\int_{-\infty}^{\infty} |S(f)|^2 df}}, \quad (18)$$

where  $S(f)$  constitutes the voltage signal spectrum of the desired signal energy passed by the receiver front-end. As modeled by Equation (18), the spectral shape of the transmit waveform will govern the value of  $B_{rms}$ . Where a waveform of near-uniform spectral density is employed, like the rectangular shape of a  $B$  band-limited white noise,  $B_{rms}$  is approximately equal to  $\pi B/\sqrt{3}$  or  $1.81B$  [6].

In the context of radar performance, the more commonly used notation (and that which is followed in later computations) is the standard deviation of the time delay measurement error,  $\sigma_\tau$ . Therefore, Equation (17) can be expressed as [2]

$$\sigma_\tau \geq \frac{1}{B_{rms} \sqrt{2 \frac{E}{N_o}}}. \quad (19)$$

It is important to note that this relationship is the optimum estimation. As such, it assumes the pulse-integrated SNR at the output of a *perfectly matched filter* can be used to approximate the  $E/N_o$  term. Nathanson cautions that the  $E/N_o$  be factored by a matching loss which is only equal to 1 when a perfectly matched filter is employed [2]. The lower bound is also specific to the case in which *internal* receiver thermal noise is limiting the measurement sensitivity [2]. When other sources of measurement interference are setting that limit, whether it be strong clutter, external noise, or even closely spaced targets, the true  $E/N_o$  is much more variable, and typically smaller. A common practice is to estimate the accuracy based on the expected  $E/N_o$  in a particular target/clutter engagement. This expected  $E/N_o$  is similar to the threshold set for declaring a target detection and the common practice in target tracking and sensor fusion algorithms. The characterization experiments detailed in Chapter III measure the expected system response and nominal  $E/N_o$  for the AFIT NoNET, which is used in predicting the system's range accuracy. Additional details of the CRLB as it applies to Doppler estimation error and the radar uncertainty principle can be found in [6].

## 2.4 Multistatic Theory

Of prime interest in implementing a multistatic radar design is the theory that it can improve the localization estimates of targets in a remotely sensed environ-

ment. The improvement is a result of illuminating and collecting with geographically distributed sensors. By introducing spatial diversity in the target observations, cross-range accuracy and resolution are attained and any spatially unique target scattered energy is exploited. Therefore, the basic geometry and the associated impacts on parametric measurements are critical theories to develop.

#### **2.4.1 Multistatic Geometry and Measurement Parameters.**

To simplify the resulting geometries and subsequent fusion algorithms, the multistatic geometry is limited to a 2-dimensional problem, where all sensors and targets are coplanar. Figure 14 depicts an example of a single-transmitter, multiple-receiver (1x4) multistatic radar output, which is a multilateration of four channel images used to localize a target in Cartesian space. Areas of higher intensity occur due to the linear combination of the four images, each containing a spatially unique isorange contour (where the circular isorange contour is a monostatic channel and the three elliptic are bistatic). Intuitively, a point or region of intersection, and therefore greater intensity, represents the location of a possible target or multiple targets spaced within a resolution cell. This basic multilateration technique is simulated through the use of a linear image combination as the primary data fusion algorithm. Note that target ghosts, similar to a radar false alarm, are potentially detected and estimated wherever the azimuth-ambiguous, multi-isorange contours intersect, yet where no target actually exists. It has been shown that the quantity of target ghosts in multistatic radar is often reduced by adding additional channels. A superior method of reducing target ghosts is by improving the range resolution of each channel, which further rationalizes the use of UWB waveforms in the multistatic design [55].

Because the multistatic measurement is comprised of multiple bistatic channels, the bistatic geometry seen in Figure 15 is the basis for theoretical multistatic perfor-

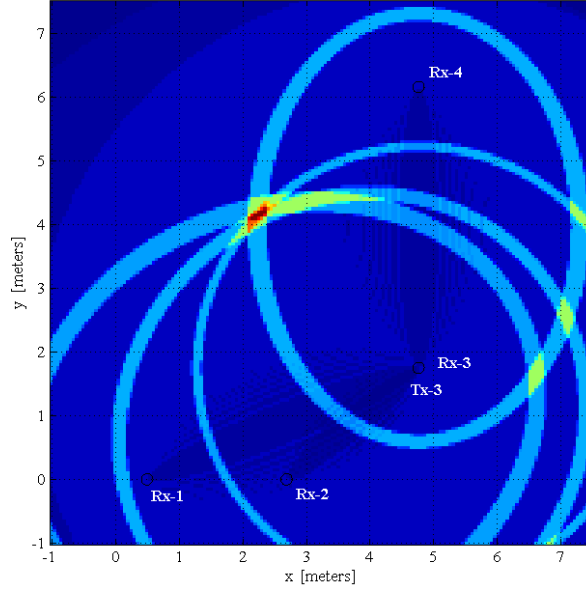


**Figure 14. Example of a 1x4 (single transmitter/multiple receiver) multistatic localization estimate using multilateration of isorange contours for target position. Note three low power target ghosts are formed between 6 and 7 meters (in the x-dimension).**

mance. When omni-directional transmit and receive antennas are utilized, the down-range representation of a bistatic channel with multiple responses in 2-dimensional Cartesian space forms a set of confocal ellipses or isorange contours.

As seen in the North-referenced coordinate grid in Figure 15, the transmitter location,  $tx_m$ , and receiver location,  $rx_k$  are endpoints that define the bistatic baseline vector of length,  $L_{m,k}$ . Note that the monostatic channel is a special case of the bistatic geometry when the transmitter and receiver are co-located ( $L_{m,k} = \beta = 0$ ), and the two-way path length becomes the well-known  $\frac{1}{2}c\tau$  expressed in Equation (2). Each ellipse represents a constant time delay of the bistatic channel and establishes the total channel path length,  $R_{m,k} = R_m + R_k$ , from transmitter  $m$  to receiver  $k$  by way of any and all scatterers located on the ellipse, such as  $(x_0, y_0)$ . Inserting the path lengths shown in Figure 15 into the general equation for an ellipse in Cartesian coordinates gives [25]

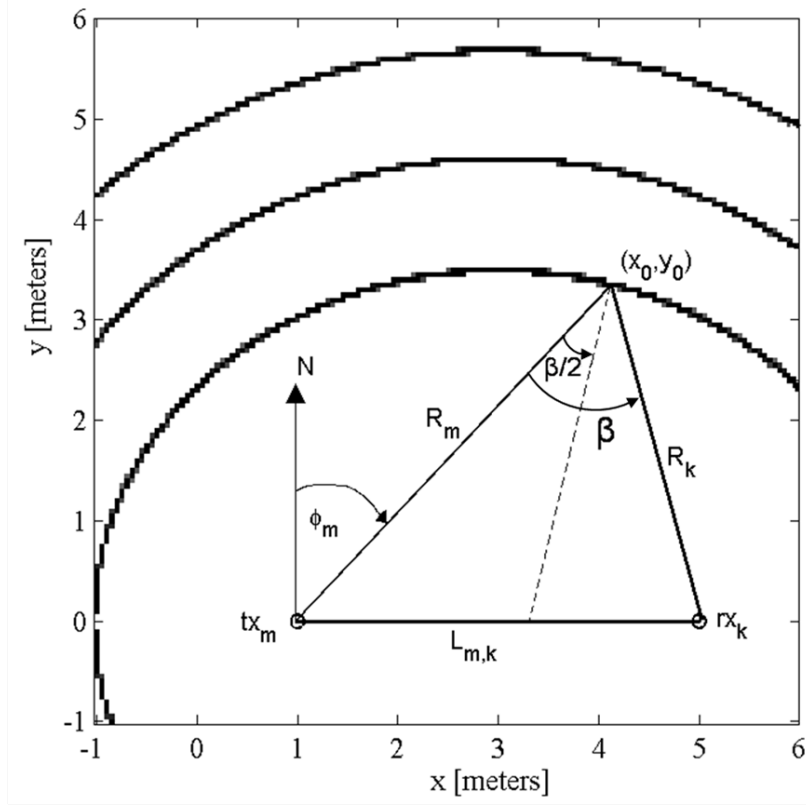


Figure 15. The geometry of the planar bistatic measurement. The bistatic baseline of length,  $L_{m,k}$  defined by transmitter location,  $tx_m$ , and receiver location,  $rx_k$  are used to produce the 2-dimensional bistatic images characterized by elliptic isorange contours [25].

$$\frac{x^2}{R_{m,k}^2} + \frac{y^2}{R_{m,k}^2 - L_{m,k}^2} = 4. \quad (20)$$

For accurate target localization and fusion of multiple downrange bistatic images, translation must be performed to a known reference, such as the location of the transmitter,  $tx_m$ . By converting to polar coordinates, the isorange ellipse is given by [25]

$$R_m(\phi_m) = \frac{R_{m,k}^2 - L_{m,k}^2}{2(R_{m,k} - L_{m,k} \sin \phi_m)}, \quad (21)$$

where  $\phi_m$  is the angle with respect to the North reference standard (parallel to the positive y-axis). As seen in Figure 15,  $R_m(\phi_m)$  is now the polar distance from the

transmitter to the ellipse at the angle  $\phi_m$ .

The bistatic range resolution is directly influenced by the geometry of the measurement, and is modeled as a geometric dilution of the monostatic resolution defined by Equation (9). The downrange resolution,  $\Delta DR$ , as seen along the bisector angle,  $\beta/2$ , is given by,

$$\Delta DR = \frac{c}{2B \cos(\beta/2)}. \quad (22)$$

Clearly, at small bistatic angles the downrange resolution (in the direction along the bisector,  $\beta/2$ ) approaches the monostatic range resolution. Furthermore, near the bistatic baseline where the largest of bistatic angles are encountered, all resolution along the bisector is lost.

As seen in Figure 16, the cross-range (or angular) resolution capability of this multistatic radar is a direct result of the wide spatial diversity of the measurements. When performing multilateration of the system's channels, the upper bound of the cross-range resolution is simply the monostatic range resolution, developed in the previous section. As a result, the smallest downrange and cross-range resolution cell is formed by two distributed monostatic isorange contour measurements that are spatially orthogonal with respect to a resolution cell containing the target of interest.

Similar geometric influences can be seen with the theoretical bistatic range accuracy, as the downrange error variance also approaches that of the monostatic at smaller bistatic angles. When the angle is not small, the other key factor in the multistatic localization accuracy is the geometry-dependent SNR of the bistatic channel.

Some of the key geometric factors can be seen in the basic bistatic radar range equation expressed for the target signal received power. At the input to the receiver,  $rx_k$  from a bistatic channel originating at transmitter,  $tx_m$ , the input power  $P_k$  of the desired target-scattered signal is given by [34]



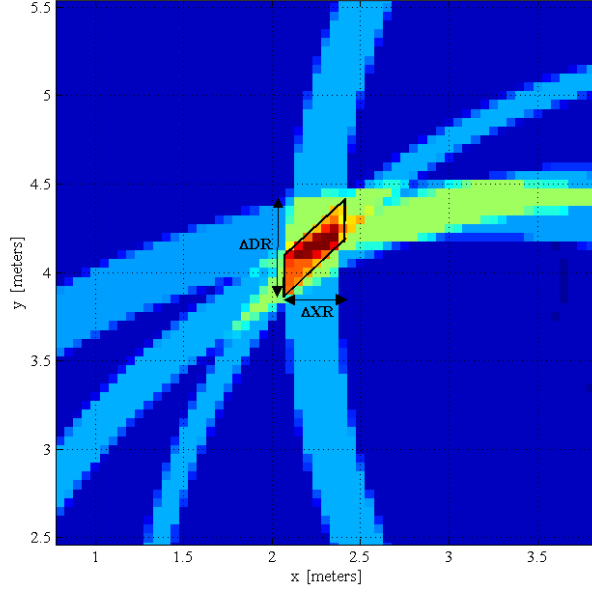


**Figure 16.** The fused downrange images of widely separated multistatic radar produces varying degrees of cross-range resolution. The fused image resolution cell is the aggregate of small and large downrange resolution cells across the shared coverage area and is based on the position of the radar nodes and the respective geometries of their isorange contours.

$$P_k = \frac{P_m G_m(\Omega) G_k(\Omega) \lambda_c^2 \sigma_b(\beta) F_k(\Omega) F_m(\Omega)}{(4\pi)^3 R_m^2 R_k^2} \quad (23)$$

where  $P_m$  is the transmitter power,  $G_m(\Omega)$  and  $G_k(\Omega)$  are the channel's angle-dependent directivity gains of the transmit and receive antennas, and  $F_k(\Omega)$  and  $F_m(\Omega)$  are the angle-dependent propagation factors. Here,  $\lambda_c^2$  is the wavelength of an UWB signal's center frequency, and  $\sigma_b(\beta)$  is the angle-dependent distribution of the target's bistatic RCS. A good example of the angle-dependent (elevation in this case) propagation impacts on the received signal power is the single and/or double bounce ground plane effects as depicted in Figure 17 [27]. When considering direct,  $D$ , and indirect,  $I$ , ground plane propagation, there are four possible round trip paths that the signal can travel. The resulting interference patterns are strongly dependent upon the electrical path lengths of EM propagation driven by the values of antenna

height,  $h_a$ , target height,  $h_t$ , and range,  $R$ . Also critical are the complex reflectivities of the target and ground at the grazing angle,  $\theta$ . As the recent studies on multistatic diversity gains have shown, bistatic propagation factors and RCS distributions can neutralize the negative geometric effects like target scintillation, glint, or multipath-induced target fading that greatly affect target detection probabilities [31]. For brevity, this simplified version of the range equation (Eq. (23)) is used to highlight the core geometric implications of the available received power from the target. However, other key geometric considerations in modeling the available SNR, like the distributions associated with multistatic clutter [10], the degree of spatial correlation of external noise sources [48], and even UWB Doppler-spreading losses caused by high radial velocity targets [37], while certainly at play, are not critical to the basic theory presented in this discussion.

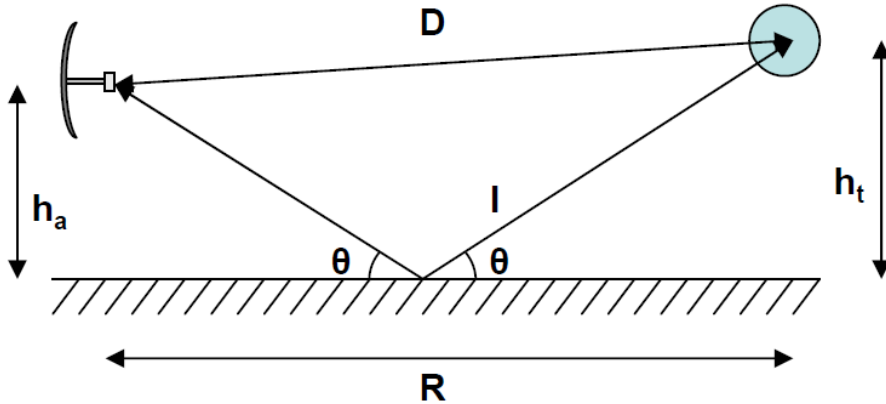


Figure 17. The ground plane multipath effect is one example of the geometry dependent propagation factors impacting both monostatic and bistatic channels (Reproduced from [10]).

As one of the core principles in potential multistatic enhancements, observing a target from different aspect angles enables diverse monostatic and bistatic RCS characteristics to be measured simultaneously. As a rule of thumb, the bistatic RCS of simple specular scatterers at small bistatic angles can be estimated from the monos-

tatic RCS at the bisector angle [5]. However, for more complex scatterers or for larger bistatic angles ranging from  $30^\circ$  and greater, the monostatic-to-bistatic equivalence theorems lose their fidelity and the RCS is best attained via measurement [3]. Furthermore, beyond approximately  $165^\circ$  the forward scatter region is known to produce significant increases in RCS, from 10 to 25 dB being reported [17, 19, 55]. Ironically, it is the coverage region on and very near the baseline, where the theoretical range accuracy and resolution becomes indeterminate, that the enhanced forward scatter RCS,  $\sigma_F$ , is observed. Originally identified by Siegel, the enhancement is a unique result of the constructive interference produced by the incident and scattered EM fields in the shadow region of a target [18]. Using physical optics, which is valid for incident wavelengths,  $\lambda$ , much smaller than the target dimensions,  $\sigma_F$  is approximated as [7]

$$\sigma_F \approx \frac{4\pi A^2}{\lambda^2} \quad (24)$$

where  $A$  is the target's shadow area, or silhouette. The theoretical radiation pattern of the forward scatter can be modeled after a uniformly illuminated aperture having the same area as the target's shadow area. Therefore, the lower the frequency of the incident wave, the broader the main forward scatter lobe becomes, and the phenomenon is observable for larger ranges of  $\beta$ .

While this region may provide signal enhancements, the forward scattered clutter and strong line-of-sight transmit signal can also add significant interference to the measurement. As is discussed in Chapter 3, the multistatic performance experiments seek to explore such phenomenology in their design. Furthermore, the impact of these various geometric dependencies on multistatic channel SNR must be considered and adequately captured when deriving a multistatic receive signal model, like that presented in the next section.

### 2.4.2 Multistatic Signal Model.

Each radar receiver of a multistatic system is designed to collect the RF signal and perform some level of initial processing on it. A critical design trade is in the amount of information that will be sent via communication link to the central processor. Based again on the overarching system CONOPS, design trades are made between distributed and central processing, command and control, and datalink bandwidths in light of the detection and estimation fidelity requirements of the system. Therefore, one of the key descriptors of a multistatic system becomes the signal and data processing architecture it employs. Common to most architectures is a general mathematical model of the combined receive signal of the distributed active sensors. Using similar notation and procedure to that of a recent publication on MIMO radar signal processing [34], the model provides a useful framework for the design and analysis of multistatic channels. To begin, a variation of the bistatic radar range equation (Eq. (23)) is modified to capture all angle dependencies associated with the  $m, k$  channel geometry (as depicted in Figure 15). Therefore, all channel specific gains and losses described in Equation (23) are reduced to a single coefficient,  $\alpha$ , representing the received voltage from each target scattered channel. With functional dependency on  $\sigma_b$  to highlight the impact of the bistatic RCS on its value,  $\alpha_{m,k}$  is defined as [34]

$$\alpha_{m,k}(\sigma_b) = \sqrt{\frac{P_m G_m G_k \lambda_c^2 \sigma_b F_m F_k}{(4\pi)^3 R_m^2 R_k^2}} e^{-j2\pi\Psi}, \quad (25)$$

where

$$\Psi = \frac{\gamma R_{m,k}}{\lambda_c} \quad (26)$$

has been included to combine the signal's phase shift due to the path length,  $R_{m,k}$ , and potential complex reflectivity,  $\gamma$ , of the bistatic target scattering. Therefore, a

multistatic receive signal is given by [34]

$$r_k(t) = \sum_{m=1}^M [H_{0/1} \alpha_{m,k}(\sigma_b) s_m(t - \tau_{m,k}) + c_{m,k}(t - T_{m,k})] + j_k(t) + n_k(t), \quad (27)$$

where the  $k$ th receiver and  $m$ th transmitter together form the  $m, k$ th channel path for a total of  $MK$  channels. The time-delays associated with target,  $\alpha_{m,k}(\sigma_b) s_m$ , and clutter,  $c_{m,k}$ , scattering are  $\tau_{m,k}$  and  $T_{m,k}$ , respectively. External interference, such as a noise jammer, is accounted for with  $j_k(t)$ , while  $n_k(t)$  describes the total internal noise of the  $k$ th receiver (including thermal and quantization noise). One assumption made in the model is that a target be simultaneously visible (unobstructed by terrain or other obstacles) in each transmitter-receiver channel. Therefore, the target presence binomial,  $H_{0/1}$ , assumes the visibility factor is satisfied, as well [25].

Assuming a direct-conversion digitization of the transmit and received signal at the  $k$ th receiver allows further model development in discrete form. The digital correlation processing, denoted by the  $\otimes$  symbol, is performed with each of the  $M$  digitized transmit replicas,  $s_h[n]$ , such that

$$x_{h,k}[n] = r_k[n] \otimes s_h[n]. \quad (28)$$

In Equation (28),  $x_{h,k}$  can be thought of as the combined output of a bank of digital correlators designed to

1. segregate the  $s_m$  transmissions mixed during free-space propagation,
2. produce a discrete time delay response for each of the correlated signals,
3. suppress internal noise and external interference, and
4. isolate in time the clutter signals from the desired target signal.

To support these theories the signal model must be expanded by distributing the correlation across the three primary components of the digital receive signal. By plugging Equation (27) into Equation (28) and assuming a digital time sampling rate of  $t_s$ , the output of the multistatic digital correlation receiver can be modeled as

$$\begin{aligned}
x_{h,k}[n] &= H_{0/1} \sum_{m=1}^M (\alpha_{m,k}(\sigma_b) s_m[n - \tau_{m,k}/t_s] \otimes s_h[n]) \\
&\quad + \sum_{m=1}^M (c_{m,k}[n - T_{m,k}/t_s] \otimes s_h[n]) \\
&\quad + (j_k[n] + n_k[n]) \otimes s_h[n], \tag{29}
\end{aligned}$$

$$\begin{aligned}
&= H_{0/1} \alpha_{m,k}(\sigma_b) R_h[n - \tau_{m,k}/t_s] + \sum_{m \neq h}^M H_{0/1} \alpha_{m,k} R_{m,h}[n - \tau_{m,k}/t_s] \\
&\quad + R_h[n - T_{m,k}/t_s] + \sum_{m \neq h}^M R_{m,h}[n - T_{m,k}/t_s] \\
&\quad + R_j[n] + R_n[n]. \tag{30}
\end{aligned}$$

It can be seen that when a target is present and visible by all  $M$  channels (i.e. condition  $H_1$ ), the auto-correlation term  $R_h[n - \tau_{h,k}/t_s]$  will be the desired dominant contributor in the  $x_{h,k}$  output signal. Competing with that signal are the  $M-1$  other signal and clutter cross-correlations, i.e. both  $R_{m,h}$  summation terms for  $m \neq h$ . As discussed in the waveform section, a key principle in a multistatic network is the use of orthogonal transmit waveforms. Here, that theory extends to produce low cross-correlations in external noise source correlations,  $R_j[n]$  and internal receiver noise correlations,  $R_n[n]$  terms of Equation (30). In practice, each of these will have a specific degree of orthogonality to  $s_h$ , the aggregate of their correlation setting the noise floor in the receiver. As for the single  $m = h$  clutter correlation term, because the AFIT NoNET is a stationary high resolution multistatic design, the effective response of the clutter auto-correlation,  $R_h[n - T_{h,k}/t_s]$ , can be mitigated in

two ways. First, the high range resolution creates range bins associated with smaller physical areas of each downrange clutter ring (or isorange clutter contour). Therefore, not only is the strong clutter often resolved in range from the target, the overall strength of each clutter patch that is co-range with the target (i.e. when  $T_{h,k} = \tau_{h,k}$ ) is reduced. Furthermore, techniques such as background subtraction (when training data is available) and non-coherent change detection (when moving targets are of interest) can further aide in suppressing the stationary clutter. Although, multistatic clutter has not been extensively studied, it is known to have significant geometric dependencies and must be considered in multistatic designs [4].

## 2.5 Chapter Conclusion

The underlying theories that support the monostatic design and subsequent multistatic operations have been presented. The enabling features of using continuous random noise as a transmit waveform were expressed using the theory of the AF, from which the key performance parameter of range resolution was derived. The simplicity of the AFIT NoNET receiver originates from its direct-conversion, digital correlation design. Using minimal RF front-end components, the cross-power spectral density of the spectral estimates of the digitized transmit replica and receive signals provide the basis for measuring their cross-correlation. The next chapter tests the validity of these enabling theories, characterizes the critical parameters of the system architecture, and establishes the methodology for assessing the target localization performance of the monostatic and multistatic system configurations.

## III. System Characterization and Experimental Design

### 3.1 Chapter Overview

This chapter defines the scope of experimentation, describing the methodology used to perform a system characterization and the design of system performance experiments. Using the traditional guidelines of the scientific method, the following general procedure is followed to characterize, demonstrate and evaluate the performance of the AFIT NoNET system.

- Predict theoretical performance
- Design and calibrate measurement systems
- Design and conduct experimental measurements
- Process collected data and analyze results

Based on the theory presented in Chapter II, the system characterization and calibration measurements in Section 3.2 provide the data necessary to compute the theoretical predictions for the range resolution and accuracy performance metrics. A description is given of each measurement used to characterize and calibrate each noise radar node in its operating environment. In addition, the distributed and central signal and data processing parameters and architecture are presented. The processing algorithms developed under this architecture are used to compute the monostatic and multistatic channel cross-correlation estimates and transform them into the high resolution range profiles necessary for image quality target localization. The plans to collect the monostatic and multistatic localization performance measurements with this fully characterized and calibrated system are described in Section 3.3. The rationale and objectives in the design of each experiment is discussed, and a test matrix



provides details for the specific system configuration, target types and measurement geometries for each trial. To conclude the chapter, a discussion on risk mitigation plans, a review of evaluation methods, and a summary of experiment goals are presented.

## 3.2 System Characterization

System characterization is the focus of the initial design of experiments. Required to compute the predicted performance of the system, the characterization provides a measurement of the system's noise floor along the receive chain, the system's effective bandwidth, and available signal-to-noise ratio (SNR) based on the implemented receiver processing architecture. Additionally, the characterization identifies the critical calibration points for both the single node and network level of operations. Lower level (i.e, RF component level) characterizations have been performed on the AFIT NoNET radar module and documented in previous research [43]. Rather than repeat that level of characterization, the approach is to build on that work, with a focus on system operating levels.

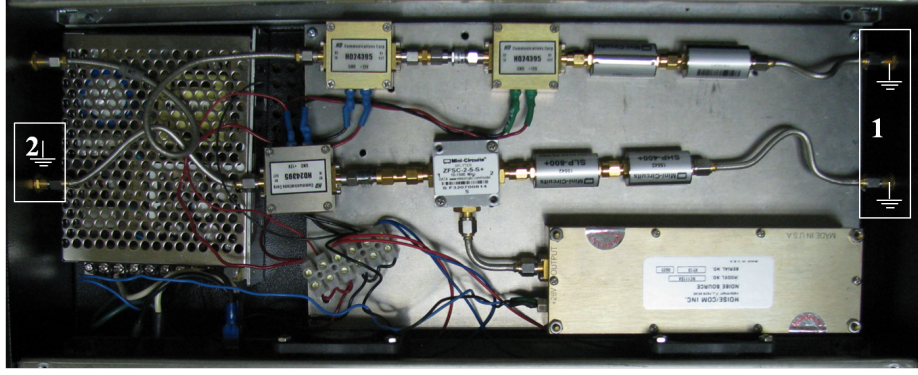
The actual performance of the AFIT NoNET monostatic and multistatic modes and realistic predictions of those metrics are based on two key system architecture characteristics. These include the calibrated system response, which is a direct result of the receiver front-end operating characteristics, and the distributed and central signal and data processing architecture, which utilize both coherent and non-coherent digital processing algorithms. Therefore, the system characterization is scoped for measurements, calibrations and processing descriptions that will support a systematic design and execution of the subsequent localization performance experiments.

### 3.2.1 System Response and Calibration Experiments.

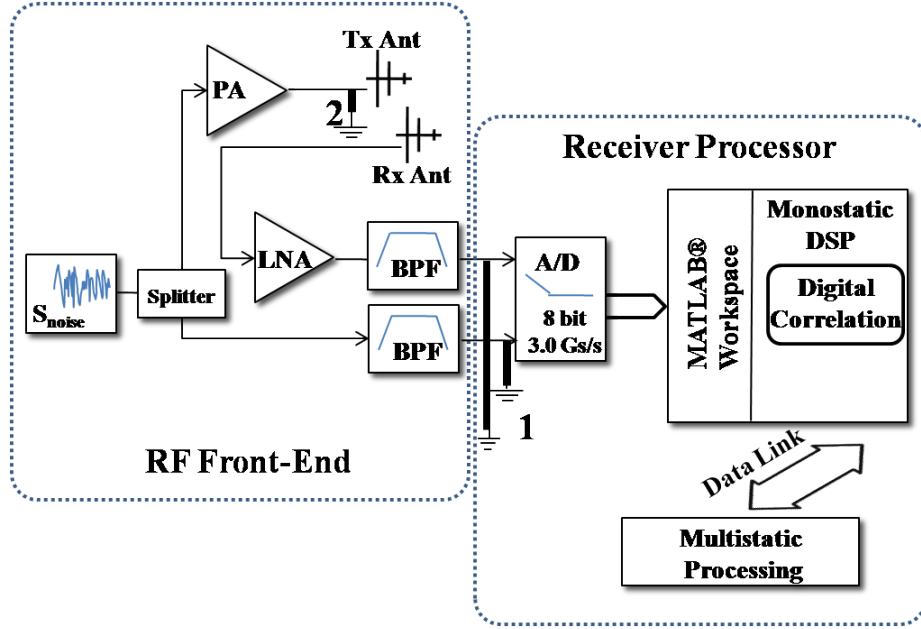
Like all radar receivers, the basic receiver operating characteristics of the noise radar constitute the aggregate response of the receive chain hardware components. Effective calibrations insure a linear system response, predictable receiver noise power spectral densities, and accurate receiver processing conversion from correlation sample space to the downrange domain. The first two measurements listed in Table 1 correspond to the annotated test point terminations in Figure 18. These initial experiments are used to verify theoretical and documented receiver front-end performance, inclusive of the A/D thermal and quantization noise characteristics as discussed in Section 2.3.1. This includes analysis of the power spectral densities and second-order statistics of the noise along the receive chain followed by total system response measurements in its nominal operating environment. The full system response measurements and subsequent range calibrations are designed for two reasons. The first is to establish input power calibration procedures insuring appropriate linear use of the receiver's dynamic range and accurate conversion of the target response to a time-delay domain via a two point range calibration. The second purpose is to measure the received signal bandwidth and calibrated target response SNR for use in the theoretical range resolution and range accuracy performance computations.

**Table 1.** Measurements are taken along the receive hardware chain of NTR6 for an operating system response characterization. The multi-system characterization and 2-pt range calibration measurements are used to calibrate receiver dynamic range and time-delay conversion algorithms. All measurements are taken in the AFIT RCS Range.

| Trial       | System | Comments   |
|-------------|--------|--|
| <i>P0_1</i> | NTR6   | Rx front-end off, source off; termination point 1        |
| <i>P0_2</i> | NTR6   | Rx chain on, source on; termination point 2              |
| <i>P0_3</i> | NTR6   | Both chains on; A/D, LNA, chamber, coupling, and clutter |
| <i>P0_4</i> | NTR6   | Both chains on; adds NTR1, NTR2, NTR3 external noise     |
| <i>P0_5</i> | NTR6   | 3.089 m - close range <i>dihedral-1</i>                  |
| <i>P0_6</i> | NTR6   | 9.045 m - far range <i>dihedral-3</i>                    |



(a)



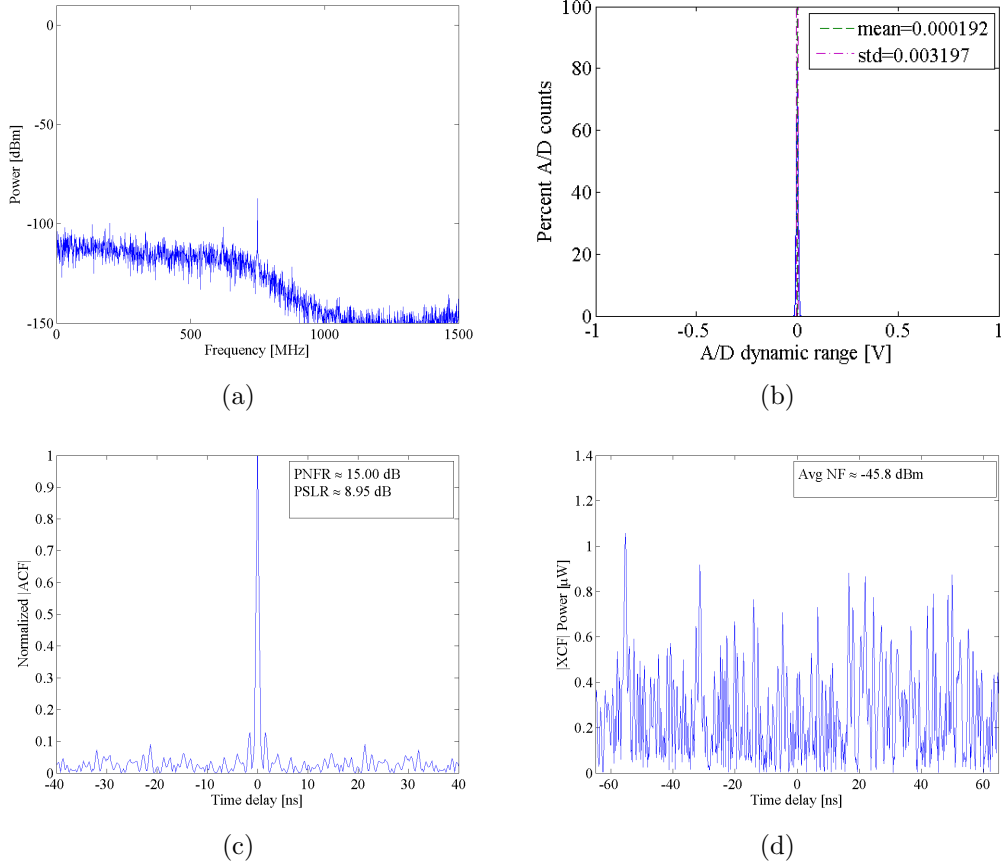
(b)

Figure 18. Experimental set-up of NTR6 characterization, where (a) depicts the actual system hardware and (b) is a block diagram annotated with the corresponding measurement termination points as listed in the test matrix.

The first and second measurements are used to characterize the impacts of the A/D, LNA, and internal coupling noises on the lower bound of the receiver's dynamic range and compare the correlation statistics to the theoretical assertions presented in Chapter II. The power spectral density and relevant first and second order statistics of the A/D receive channel's quantized thermal noise are graphed in Figure 19. Three important features are noted upon inspection. First, in Figure 19(b) at the input

range of  $\pm 1 V_{pp}$  the noise is approximately zero-mean, and toggles the central bits of the linearly quantized A/D (that is, the least significant quantization levels of  $\pm 7.81$  mV having a 3.20 mV standard deviation). Secondly, the broad, nearly-uniform power spectrum within the Nyquist bandwidth in Figure 19(a) corresponds to the expected strong, narrow peak that results in both a high peak-to-sidelobe ratio peak-to-sidelobe ratio (PSLR) and peak-to-noise-floor ratio (PNFR), as seen in the autocorrelation function (ACF) plotted in Figure 19(c). As was discussed in the ambiguity theory, this narrow peak and high PSLR provides the greatest potential for high range resolution measurements, and maintaining a high PNFR is necessary for accurate measurements. As is common practice, the  $|ACF|$  of this receiver channel measurement is normalized by its zero-delay peak magnitude. The low mean noise floor (NF) power and noise-like cross-correlation (XCF) results seen in Figure 19(d) is early evidence that the A/D channels are sufficiently isolated on the board, and that they operate with negligible spurious and harmonic distortions when digitizing band-limited thermal noise. These are all important initial indicators that the low end of the A/D dynamic range is adequately balanced and sensitive, and that the quantization noise will be uncorrelated for normal radar operations.

In an ideal case, the low end of the receiver's dynamic range would be toggled by simply the thermal and quantization noise of the A/D cascaded with the LNA thermal noise [38]. However, internal coupling of the transmitter source and possible external RF interference (RFI) must also be factored, so measurement *P0.2* is used to characterize the response due to these. Figure 20(a) shows the impact of the band-limited LNA thermal noise, internal coupling from the transmitter, and chamber RFI on the total power of the receiver's noise floor. Likewise, the band pass filtering, coloring within that occupied bandwidth, and the internal RF coupling is effecting the signal correlation statistics. As expected, the more narrow and less uniform



**Figure 19.** System Response and statistical analysis data of characterization measurement  $P0.1$  are collected using the radar's digital receiver processor as the instrumentation device. Subfigure (a) is the single-sided spectrum estimate and (b) is the histogram of percentage of A/D counts with respect to the quantized dynamic range. Subfigure (c) is a plot of the normalized  $|ACF|$  of the receive channel computed using the full  $1 \mu s$  record but only showing the central  $-40$  to  $40$  ns discrete time delays. The data's PNFR and PSLR are annotated. Time delays from  $-65$  to  $65$  ns of the two A/D channel's  $|XCF|$  is similarly plotted in (d) showing the expected low level of correlation and average noise floor.

spectrum in the effective bandwidth of the signal has widened the peak of the  $|ACF|$  and lowered the PSLR and PNFR, respectively (as seen in Figure 20(c)). The strong cross-correlations right of center in the channels'  $|XCF|$  is indicative of cross-talk (i.e. RF coupling or ringing) occurring inside the RF front-end module. This can be expected and tolerated to some degree, but ferrite absorber has been inserted between the channels to aid in keeping this to a minimum.

While transmitting into the environment, the power spectral density of the re-

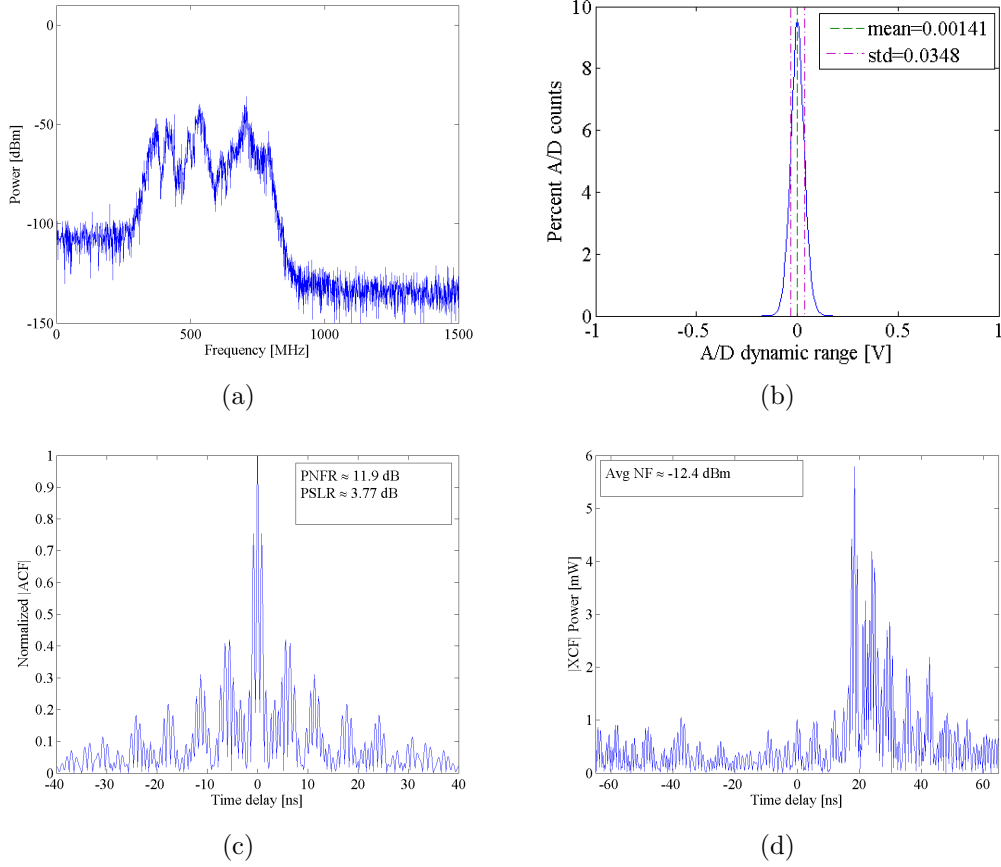


**Figure 20.** System Response and statistical analysis data of characterization measurement *P0.2* are collected using the radar’s digital receiver processor as the instrumentation device. Subfigure (a) is the single-sided spectrum estimate and (b) is the histogram of percentage of A/D counts with respect to the quantized dynamic range. Subfigure (c) is a plot of the normalized  $|ACF|$  of the receive channel computed using the full  $1 \mu s$  record but only showing the central  $-40$  to  $40$  ns discrete time delays. Time delays from  $-65$  to  $65$  ns of the two A/D channel’s  $|XCF|$  is similarly plotted in (d) and reveal larger than expected correlations and average noise floor.

ceive signal includes all of the previous plus any antenna coupling and target/clutter scattered energy collected by the receive antenna. Measurement *P0.3* is taken to capture the receiver’s response in this monostatic operating mode and to understand the impacts on the receiver’s dynamic range. Additionally, these conditions determine the mean power of the noise floor, against which the desired monostatic signal will have to compete. The spectral and statistical results of the measured response are shown in Figure 21. The power spectrum estimate plotted in Figure 21(a) is of

significant interest in that it represents the receive signal bandwidth of the end-to-end system response. By capturing and analyzing this response using the identical spectral estimation hardware and digital signal processing algorithms used in the direct-conversion, digital correlation receiver, more realistic predictions in the radar's performance can be made. Using a 3-dB cut-off bandwidth criteria (as opposed to the 10-dB roll-off standard used for channel isolation purposes), the effective receive signal bandwidth is found to be 185 MHz centered at 430 MHz. Because the radar range performance metrics are inversely proportional to the received signal bandwidth, it will be shown that these findings directly support performance predictions presented in the analysis of results in Chapter IV.

One other important observation is made during this measurement. By varying the elevation and elevation angle of the transmit and receive antenna, it is found that the close-in clutter (specifically, the antenna spillover) increases the received signal power in such a way as to cause clipping by the A/D at its peak voltage input range of -1 to 1 V. The transmit-to-receive antenna RF spillover is a known limitation in noise modulated CW systems, and additional background information on the phenomenon can be found in [45]. By adding 3 dB of attenuation at the input to the receiver RF front-end, the A/D clipping is mitigated while maintaining a proper fill in the dynamic range as seen in Figure 21(b) (std=0.2895 V). This depth of quantization effectively uses the 8-bits for band-limited Gaussian input signals, following the model presented in Section 2.3.1. Furthermore, the standard power calibration procedure used for the AFIT NoNET is to pad each receiver front-end input as required until the standard deviation of the centered input signal voltage constitutes approximately 12.5% of the full input dynamic range of the A/D. Lastly, these findings show that the upper bound to the receiver's linear dynamic range is the A/D board, even when using the full A/D input range. This is because the maximum (useful) input signal

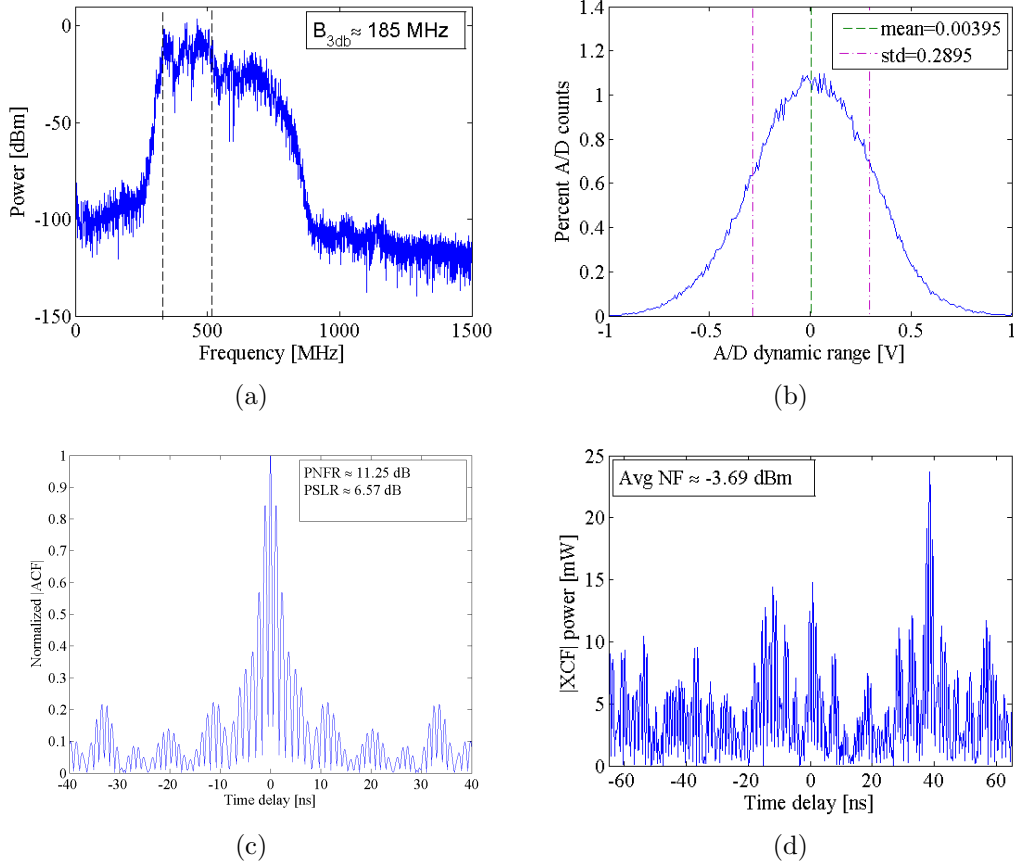


**Figure 21.** System Response and statistical analysis data of characterization measurement *P0.3* are collected using the radar’s digital receiver processor as the instrumentation device. Subfigure (a) is the single-sided spectrum estimate and (b) is the histogram of percentage of A/D counts with respect to the quantized dynamic range. Subfigure (c) is a plot of the normalized  $|ACF|$  of the receive channel computed using the full  $1 \mu\text{s}$  record but only showing the central  $-40$  to  $40 \text{ ns}$  discrete time delays. The data’s PNFR and PSLR are annotated. Time delays from  $-65$  to  $65 \text{ ns}$  of the two A/D channel’s  $|XCF|$  is similarly plotted in (d) and reveal larger than expected correlations and average noise floor.

level of the A/D board is reached well before the  $+17 \text{ dBm}$ , 1-dB compression point of the LNA.

The effects of clutter on the receive signal power is a critical constraint in the design of the performance experiments. For the goal of multistatic operations, the number of nodes, geometries, and multistatic clutter power must be considered during experimental design and calibrations to insure the direct conversion processing is not degraded due to signal power levels beyond the dynamic range of the receivers.



Therefore, the receiver response in measurement *P0\_4* is taken while operating three additional noise radar transmitters in the planned multistatic experiment configuration (as seen in Figure 27 later in the chapter). The combined average power of the spillover, clutter, RFI, and now external noise radiating from the additional sensors are evaluated. It is found experimentally that an additional 2 dB of attenuation is needed to maintain the high effective number of bits without signal clipping in the A/D. The spectral and statistical characteristics were found to be very similar to the previous trial, once properly calibrated. As expected, the calibration procedures are necessary to offset the effects of the geometric positioning of the distributed nodes. For the multistatic experiments, added attenuation requirements range from 1 to 9 dB to properly condition the input signal at each node. A potential design enhancement would be an incorporation of a voltage controlled variable attenuator at the input to the receiver RF front-end. In conclusion, this measurement establishes the final power calibrations in the multistatic configuration as all potential signals of the multistatic received signal model presented in Section 2.4.2 are accounted for, less the actual target signal. The results highlight the challenge now left to the multistatic receiver processor - isolating a relatively weak target scattered noise signal from a strong mixture of interfering noise signals.

### **3.2.1.1 Signal Processing Architecture.**

The AFIT NoNET system is operated using a software interface developed in MATLAB®. The software consists of 6 modular functions, 3 of which perform the distributed control and processing at the individual radar nodes while the other 3 are utilized by the central processor. The modularity of the hardware and software allows the central processing functions to be performed by any of the nodes within the multistatic cluster or by a stand-alone processor. Figure 22 represents the architectural

structure and gives a short description of each of the core functions.

A node's local interface with the A/D board is established within MATLAB<sup>®</sup> using Microsoft<sup>®</sup> .NET 3.0 Framework<sup>TM</sup> and the .NET assembly supplied by the board manufacturer, Acquisition Logic. To streamline the receiver signal processing, the digitized waveforms are read into the MATLAB<sup>®</sup> workspace via direct memory access (DMA) of the A/D board. This same interface is used to initialize the signal collection parameters, like sampling frequency, number of records per trigger, input voltage range, etc, for each measurement.

The A/D board samples at a maximum rate of 3.0 GSa/s, which provides the 2-channel interleaved rate of 1.5 GSa/s. By default the board's FPGA synthesizes 3 additional interpolated samples per actual sample, a feature that was left enabled after preliminary testing showed the smoother correlation responses were easier to interpret. Furthermore, it is confirmed that using a coherent digital correlation of the maximum  $1 - \mu s$  record length provides the greatest SNR response [43]. For additional SNR gains via response averaging, the multi-trigger capability of the A/D board is used to collect a total of 40 full waveforms per channel (i.e. 40 of the  $1 - \mu s$  receive signals and 40 of the  $1 - \mu s$  transmit replica signals). Therefore, a single DMA call imports 480 Kbytes via Peripheral Component Interconnect Express (PCIe) into the local MATLAB<sup>®</sup> workspace. Because the onboard flash memory of the A/D board allows up to 512 Mbytes to be stored and accessed by a single DMA call, future AFIT NoNET DSP designs should continue to weigh the latency/throughput trades specific to the sensing application.

The core of the distributed DSP design is the digital correlation of the full 6000 samples of each of 40 receive and replica waveform pairs. Those 40 correlations are then averaged, and the monostatic response of the DSP integration interval is ready for data post-processing. If the node is part of a distributed cluster of nodes tasked

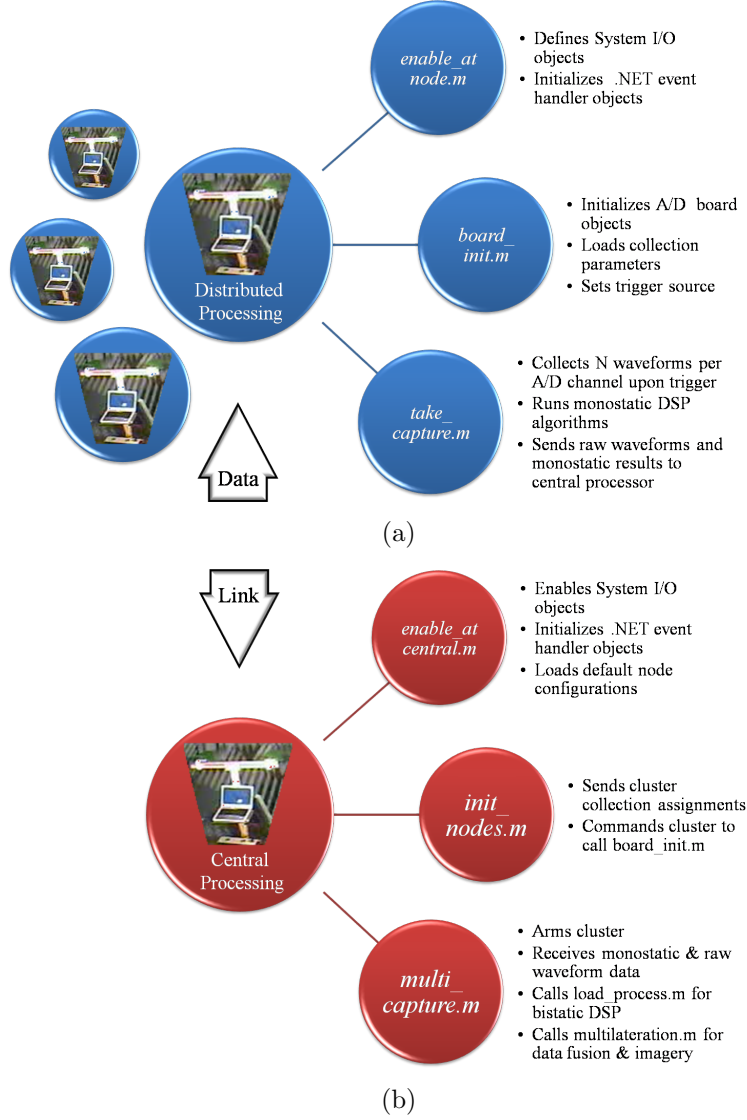


**Figure 22.** The multistatic signal processing architecture consists of both (a) distributed and (b) central processing functionality. Three primary communication, control and DSP Matlab® functions are implemented at each level.

with providing a multistatic solution, the monostatic response and waveforms are datalinked to the central processor via a wireless access point. The DSP routines for each bistatic channel are then performed by the central processor. Details of the MATLAB® code and its implementation in a multistatic measurement with a cluster of nodes is found in Appendix A. Once all signals have been processed, a variety of post-processing functions can be implemented, including conversion to 1-D or 2-

D downrange profiles, peak detection, background subtraction, and of course, data fusion for netted-monostatic or multistatic imagery. While some of these processes will be discussed in detail in Chapter IV, execution of the 2-pt calibration relies on the 1-D downrange profile post-processing.

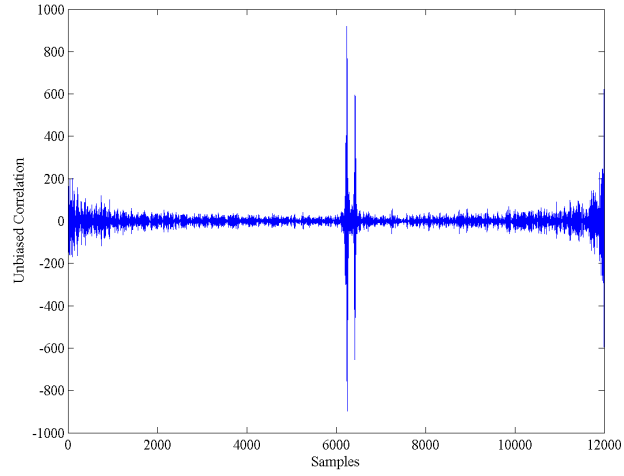
### 3.2.1.2 Range Calibration.

Post-processing of the raw correlation response is necessary to perform the 2-pt range calibration and subsequent performance experiments. Figure 23 depicts the evolution of the measurement at each stage of the data post-processing. The output of the digital correlation processing is shown in Figure 23(a), where samples 6000 to 11999 correspond to approximately 150 meters of downrange response based on the 0.1667 nanosecond per sample rate. The processing architecture allows tremendous flexibility in predefining or post-processing the specific range coverage of interest. For measurements taken inside the AFIT RCS chamber, only 10 meters of coverage is required ( $\sim 400$  samples). The monostatic channel data consistently occurs between the 200th sample lag,  $R_{sr}[200]$  and the 600th sample lag,  $R_{sr}[600]$  for the 10 meters of coverage. For bistatic channels, the relative timing of the trigger signal sent to each node (along with the channel specific internal RF path lengths) determines the correlated sample windows of interest. Experiments revealed a wide variety of both early (negative lag) and late (positive lag) windows of bistatic correlation that capture the range coverage of interest. The bistatic DSP is necessarily more dynamic, looking across a  $R_{sr}[-600]$  to  $R_{sr}[800]$  correlation field of view. Using the strong response occurring for the direct line of sight, the channel's unique time delay origin is located within this field of view. The subsequent conversion to range (mapping to the isorange contour geometry as detailed in Section 2.4.1) is made relative to the known bistatic baseline range. Details of this process are expounded upon in the introductions to

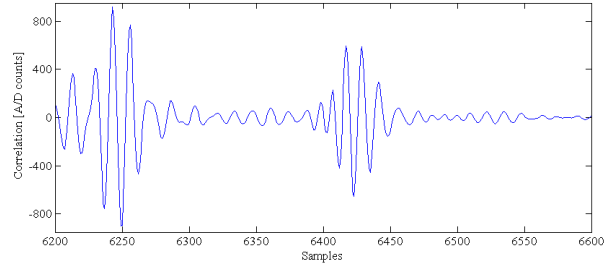
the multistatic analysis of results.

In Figure 23(b) the first (and usually strongest) peak response in a monostatic measurement is due to the combined direct line-of-sight and ground-bounced antenna spillover of the horizontally co-polarized transmit and receive antennas. The location of this spillover represents the total EM path length of (1) the transmitter hardware chain (minus the path length that the transmit replica travels before digitization), (2) the free-space direct and single bounce propagations from the transmit antenna to the receive antenna, and (3) the receive hardware chain. Each node’s antennas and antenna crossbar fixtures were positioned the same for all performance experiments (maximum separation in azimuth between horizontally polarized transmit and horizontally polarized receive antennas and maximum height above ground). Analysis of the locations and magnitudes of these spillover responses measured over the course of many experiments provides insight into the stability and uniqueness of each system’s response.

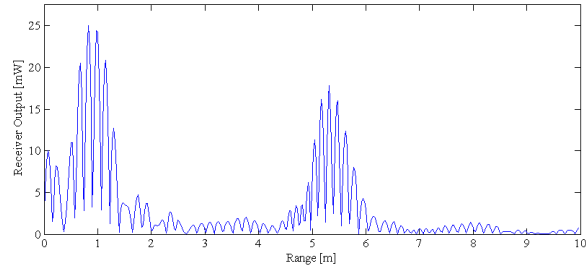
As seen in Table 2, the statistics of the spillover peak show the consistency from measurement to measurement for each node. However, the sample locations and peak power of the spillover vary from system to system. Such variations are expected. While the systems are built-up from identical component part numbers, physical dimensions, and nearly identical RF plumbing, the experiments reveal that each node has a unique (hardware inherent) response completely independent of the other temporally and spatially unique factors in a measurement. This system uniqueness also impacts each transmit-receive bistatic channel in the multistatic system, where each channel’s unique hardware is part of the measured time delay for that channel. As seen in Figure 23(c), the final monostatic data processing routine takes into account these internal time delays of the channel and converts the time-delay based samples to the downrange domain using Equation (2). Though original multistatic processing



(a)



(b)



(c)

**Figure 23. Response features and post-processing evolution of the target response developed for range calibration and performance evaluations.**

designs used the strong spillover peaks to serve as real-time reference points for the conversion to time-delay (i.e. downrange), the 2-point calibration technique is a more precise process for range calibration and is therefore the method used in subsequent experiments.

**Table 2.** Statistics of the antenna spillover response peaks are based on 28 individual background measurements taken with each system spread throughout two weeks of experiments. Antenna heights are fixed on each node, but node locations within the chamber vary. Peak magnitudes represent the output power response of the digital receiver correlator. Though the peak locations (in samples) are relatively stable from measurement to measurement, the system to system variance is noted.

| System             |             | NTR1  | NTR2  | NTR3  | NTR6  |
|--------------------|-------------|-------|-------|-------|-------|
| location (samples) | mean sample | 250   | 250   | 227   | 230   |
|                    | std sample  | 1.6   | 3.7   | 0.2   | 2.6   |
| magnitude (mW)     | mean power  | 25.11 | 15.32 | 25.82 | 17.46 |
|                    | std power   | 0.88  | 0.84  | 0.56  | 0.97  |

The 2-point range calibration measurement establishes the appropriate time origin of the system's response by calibrating out any time delay that is not due to free-space EM wave propagation to and from scatterers in the environment. The procedure must also account for the implications seen in the accuracy theory developed in Chapter II. Because the standard deviation of range error is inversely proportional to the square of the available SNR, range measurement accuracy of a constant RCS target degrades as it moves farther out in range [13]. The method of using both a small and large RCS target provides similar SNR values at close and far ranges, insuring consistent levels of range accuracy during the calibration procedures. The hip-pocket RCS equation of a rectangular dihedral is used to design the corner reflectors needed in the calibration. The RCS can be approximated by

$$\sigma \approx \frac{8\pi a^2 b^2}{\lambda^2}, \quad (31)$$

where  $a$  and  $b$  are the dimensions of the reflector sides and  $\lambda$  is the center wavelength of the incident wave. This RCS approximation and the radar range equation are used to compute two target RCS's for a constant received power, one for the 3-meter range and one for the 9-meter range. As seen in Figure 24, **dihedral-1** (2.0 dBsm) for the close range measurement and **dihedral-2** (26.5 dBsm) for the far range measurement

are constructed. Finally, a nominal SNR prediction can be made using the average

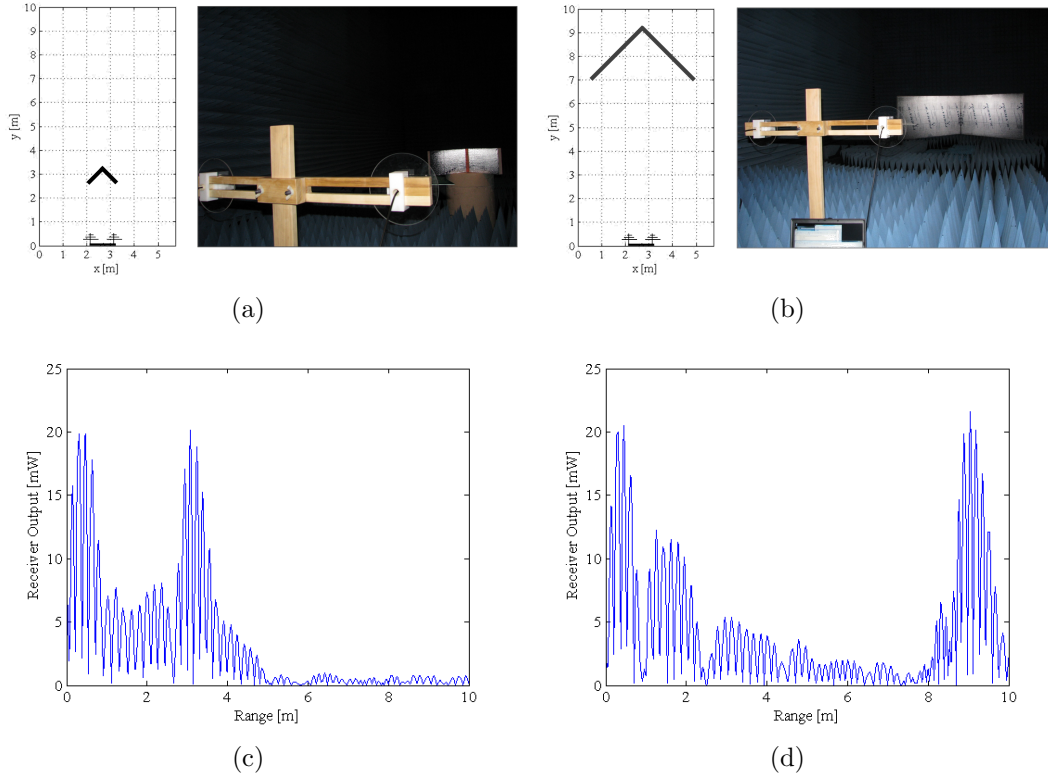


**Figure 24.** Experimental set-up with (a) dihedral-1 and (b) dihedral-2 for the mono-static 2-pt range calibration measurements and associated calibrated results showing post-processed downrange target profiles at (c) 3.089 meters and (d) 9.045 meters with target truth range uncertainty of  $\pm 0.39$  cm using the laser range finder.

power of the peak target responses measured in the 2-pt range calibration, 20.12-mW at the close range and 21.93 mW at the far range. The ratio of the 21.03-mW signal power to the 0.43-mW mean noise power found in measurement *P0\_3*, is 48.91 or 16.89 dB. This, along with the RMS bandwidth of the received signal, are carried forward for the range accuracy performance prediction in Chapter IV.



### 3.3 Monostatic Localization Performance

#### 3.3.1 Range Resolution Experiment.

Using a single radar node, a series of monostatic measurements are taken. The primary purpose is the evaluation of the AFIT NoNET monostatic range resolution. Two dihedral corner reflectors (`dihedral-1`) and (`dihedral-3`) serve as targets. Figure 25 shows the physical layout of the experiment and Table 3 captures the test matrix. Initially, the upper `dihedral-3` is stacked vertically aligned with the lower `dihedral-1`, allowing for a co-range measurement. With each subsequent trial, `dihedral-3` is repositioned at approximately 12.5 centimeter steps increasing in downrange distance from the radar, while `dihedral-1` remains at its initial range. By using non-moving targets having a similar RCS, the experiment is designed to

**Table 3.** Monostatic responses of a two target scene are used to assess the range resolution of the AFIT NoNET. Target distances are measured downrange with respect to the radar node using a laser ranging device with a measurement standard deviation of +/- 0.39 cm.

| Trial          | Systems | dihedral-1 (m) | dihedral-3 (m) | Comments                |
|----------------|---------|----------------|----------------|-------------------------|
| <i>P1bkg1</i>  | NTR6    | -              | -              | target supports/chamber |
| <i>P1res1</i>  | NTR6    | 5.282          | 5.291          |                         |
| <i>P1res2</i>  | NTR6    | 5.282          | 5.445          |                         |
| <i>P1res3</i>  | NTR6    | 5.282          | 5.558          |                         |
| <i>P1res4</i>  | NTR6    | 5.282          | 5.761          |                         |
| <i>P1res5a</i> | NTR6    | 5.282          | 5.881          | decreased to 5cm steps  |
| <i>P1res5b</i> | NTR6    | 5.282          | 6.067          |                         |
| <i>P1res5c</i> | NTR6    | 5.282          | 6.103          |                         |
| <i>P1res5d</i> | NTR6    | 5.282          | 6.154          |                         |
| <i>P1res5e</i> | NTR6    | 5.282          | 6.209          |                         |
| <i>P1res6</i>  | NTR6    | 5.282          | 6.332          | resume 12.5cm steps     |
| <i>P1res7</i>  | NTR6    | 5.282          | 6.462          |                         |
| <i>P1res8</i>  | NTR6    | 5.282          | 6.686          |                         |
| <i>P1res9</i>  | NTR6    | 5.282          | 6.726          |                         |
| <i>P1bkg2</i>  | NTR6    | -              | -              | target supports/chamber |

isolate target range as the single means of discrimination. The collected data from

all 13 resolution trials are analyzed to determine the minimum range difference in which the two targets are distinguishable. The resolvability assessment is based on the half-power resolution criteria, which requires a discernible 3-dB roll-off between target peaks to declare the targets resolved [6].

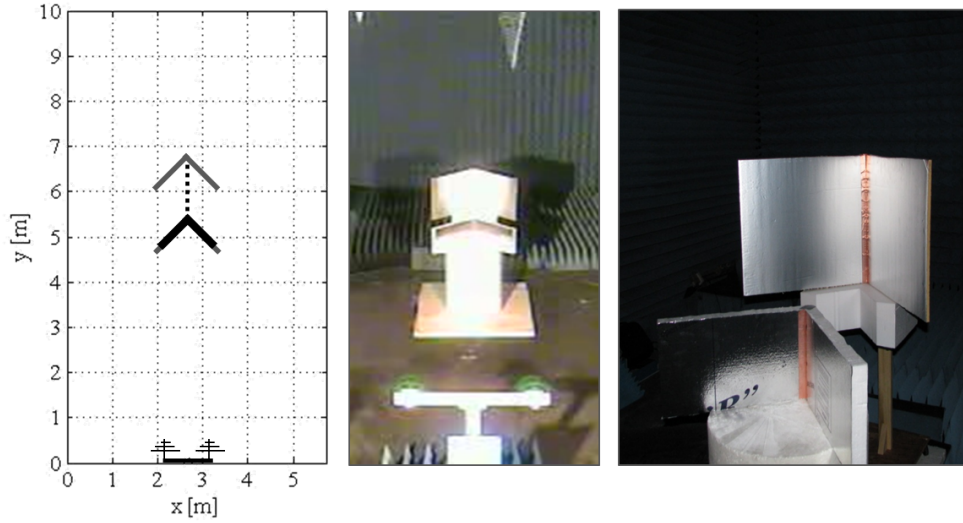


**Figure 25.** Experimental set-up of the monostatic range resolution measurements with both a top view of the experiment layout in the AFIT RCS Range and photo of the actual target scenario.

### 3.3.2 Range Accuracy Experiment.

The primary objective of the experiment is to assess the monostatic range accuracy of an individual sensor. In this series of experimental trials, NTR3 operates as a monostatic radar node and is used to measure the downrange location of **dihedral-1**. Table 4 captures the test matrix and Figure 26 shows the corresponding physical layout of the experiment. To gather the necessary statistical data to compute the accuracy in terms of an error standard deviation, **dihedral-1** is maintained in a single position for 11 measurements (the *P2acc3* trials, as seen in the test matrix).

Table 4. Monostatic responses of scene with a single target are used to assess the range accuracy of the AFIT NoNET. Target distances are measured downrange with respect to the radar node using a laser ranging device with a measurement standard deviation of  $\pm 0.39$  cm.

| Trial          | System | dihedral-1 (m) | Comments            |
|----------------|--------|----------------|---------------------|
| <i>P2bkg1</i>  | NTR6   | -              | support and chamber |
| <i>P2acc1</i>  | NTR6   | 5.674          | hold position       |
| <i>P2acc2</i>  | NTR6   | 5.723          |                     |
| <i>P2acc3a</i> | NTR6   | 5.774          |                     |
| <i>P2acc3b</i> | NTR6   | 5.774          |                     |
| <i>P2acc3c</i> | NTR6   | 5.774          |                     |
| <i>P2acc3d</i> | NTR6   | 5.774          |                     |
| <i>P2acc3e</i> | NTR6   | 5.774          |                     |
| <i>P2acc3f</i> | NTR6   | 5.774          |                     |
| <i>P2acc3g</i> | NTR6   | 5.774          |                     |
| <i>P2acc3h</i> | NTR6   | 5.774          |                     |
| <i>P2acc3i</i> | NTR6   | 5.774          | resume increment    |
| <i>P2acc3j</i> | NTR6   | 5.774          |                     |
| <i>P2acc3k</i> | NTR6   | 5.774          |                     |
| <i>P2acc4</i>  | NTR6   | 5.825          | range cal check     |
| <i>P2acc5</i>  | NTR6   | 5.871          |                     |
| <i>P2acc6</i>  | NTR6   | 5.922          |                     |
| <i>P2acc7</i>  | NTR6   | 6.412          | support and chamber |
| <i>P2bkg2</i>  | NTR6   | -              |                     |

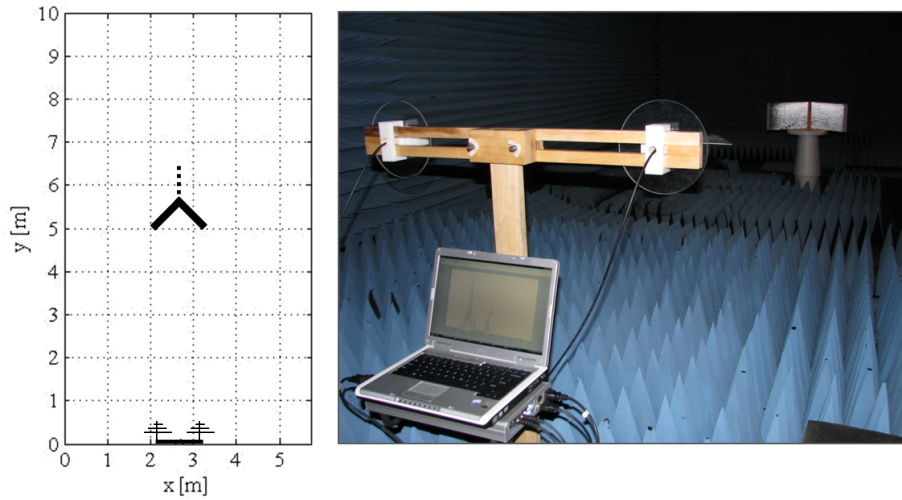


Figure 26. Experimental set-up of the monostatic range accuracy measurements with both a top view of the experiment layout in the AFIT RCS Range and photo of the actual target scenario.

### 3.4 Multistatic Localization Performance

The multistatic localization performance of the AFIT NoNET is assessed by evaluating the imagery products of the system's central fusion processing when the network is comprised of widely distributed nodes. These series of experiments are designed to demonstrate the 2-dimensional accuracy and resolution performance for a specific node configuration while also exploring the impact of target types and locations in the netted monostatic and multistatic radar imagery. The underlying constraint in the design of the multistatic experiments is the total noise power within the limited shared coverage area of the AFIT RCS range. Based on findings while performing the multistatic calibration experiment in the system characterization, the azimuthal directivity of the antenna only reduces the interference noise power between nodes by 1-6 dB depending on the bistatic geometries. This limited directivity combined with the basic  $1/R^2$  power losses aid in suppressing the total noise power in the environment to a manageable (via attenuation padding) level. Through a series of preliminary tests, a 4-node network could be distributed within the chamber and maintain linear operating power levels at each receiver.

When brought into a 2-dimensional coordinate system established within the AFIT RCS chamber, the performance metrics of downrange and cross-range are best understood relative to that system. Knowing that the performance results would be highly dependent upon the distributed locations of the nodes, the scoping principle of a single configuration of nodes with a variety of target positions is employed. Furthermore, the non-uniformly distributed AFIT NoNET nodes with respect to target positions within a shared coverage area is designed to provide a wide range of channel resolutions and accuracies in each multistatic image. Diversely intersecting isorange contours (both in terms of their signal strengths and geometry-dependent resolutions) provide varying degrees of spatial orthogonality between channel responses. Their or-

thogonality and associated monostatic and bistatic resolutions ultimately deliver the performance bounds of cross-range accuracy and resolution, which are specific to the given node-target geometries (as discussed in Section 2.4.1).

The corner reflectors were designed to provide highly directional backscatter responses for the monostatic experiments. Here, the rotationally symmetric cylinder positioned vertically provides the wide specular scattering that is well suited for multistatic measurements in the horizontal plane of interest. To investigate the potential gains associated with multistatic imaging of more complex targets, a missile shaped target is used in the accuracy performance trials. Here, the impacts of the bistatic RCS, including the effects of the bistatic channel’s forward scatter region are explored.

### 3.4.1 Downrange and Cross-Range Resolution Experiment.

The primary objective of this experiment is to assess the multistatic range and cross-range resolution performance of the AFIT NoNET. In this series of experimental trials, NTR1, NTR2, NTR3, and NTR6 (the four nodes with the most similar operating characteristics) function in a multistatic mode to produce 2-D imagery of three vertically standing cylindrical targets, `cylinder-1`, `cylinder-2`, and `cylinder-3`. Although the electrical circumference (that is, the scattering object’s dimension relative to the incident wavelength) is small for physical optics methods, the general RCS hip- pocket formula is still a valid starting point for specular scattering approximations. The RCS of a singly curved surface like the cylinder is given by [27]

$$\sigma \approx \frac{2\pi r l^2}{\lambda_c}, \quad (32)$$

where  $r$  is the radius of curvature and  $l$  is the length of the cylinder. Each has a radius of 7.63 cm, with the backscatter RCS of the taller 1.727-m `cylinder-1` being approximately 4.56 dBsm. The backscatter RCS of each of the shorter 1.525-m

`cylinder-2` and `cylinder-3` target is approximately 3.48 dBsm. In close proximity to one another and in their vertically standing orientation, three additional scattering mechanisms are expected to contribute to the cylinder’s actual RCS. Because of the incident waves horizontal polarization a traveling wave will propagate along the circumference of the cylinder launching additional RF energy into the bistatic channels. With the circumference being on the order of the center wavelength, this surface wave is expected to become a creeping wave and backscatter into the monostatic channel, as well. The second additional scattering mechanism is the corner-like multiple reflection area the cylinder makes with the ground. It will act similar to a dihedral with a reduced affective area, but will also have bistatic scattering components due to the curvature of the cylinder. Thirdly, multiple bounces between the cylinders are expected to produce additional late scattering energy in the receivers. Although the AFIT NoNET does not resolve these late scattering centers from the initial specular returns, they generally increase the aggregate RCS of the target scene and are expected to distort the accuracy and reduce the resolution of the localization measurements.

As seen in Figure 27, the physical layout of the experiment begins with the cylinders co-located near the center of the joint coverage area. The next 4 trials incrementally displace the two shorter cylinders by approximately 30 cm, `cylinder-2` in the negative y direction and `cylinder-3` in the positive x direction. Table 5 captures the corresponding test matrix. Analysis of the 2-D imagery, which is the data fusion product of 16 multistatic channels, is used to assess the separation at which the cylinders are resolved in range and cross-range in the image.

**Table 5.** Multistatic measurements using NTR1, NTR2, NTR3, and NTR6 are taken to assess the range and cross-range resolution of the AFIT NoNET. Target distances are measured with respect to a local coordinate system within the AFIT RCS chamber and taken with a laser ranging device with a measurement standard deviation of  $\pm 0.39$  cm.

| Trial         | Systems    | cylinder-1<br>( $x, y$ ) [m] | cylinder-2<br>( $x, y$ ) [m] | cylinder-3<br>( $x, y$ ) [m] | Comments |
|---------------|------------|------------------------------|------------------------------|------------------------------|----------|
| <i>P3bkg1</i> | NTR1,2,3,6 | -                            | -                            | -                            | chamber  |
| <i>P3res1</i> | NTR1,2,3,6 | (2.716, 4.085)               | (2.870, 3.915)               | (2.894, 3.946)               |          |
| <i>P3res2</i> | NTR1,2,3,6 | (2.716, 4.085)               | (2.870, 3.411)               | (3.398, 3.946)               |          |
| <i>P3res3</i> | NTR1,2,3,6 | (2.716, 4.085)               | (2.870, 3.106)               | (3.703, 3.946)               |          |
| <i>P3res4</i> | NTR1,2,3,6 | (2.716, 4.085)               | (2.870, 2.802)               | (4.007, 3.946)               |          |
| <i>P3res5</i> | NTR1,2,3,6 | (2.716, 4.085)               | (2.870, 2.498)               | (4.311, 3.946)               |          |
| <i>P3bkg2</i> | NTR1,2,3,6 | -                            | -                            | -                            | chamber  |

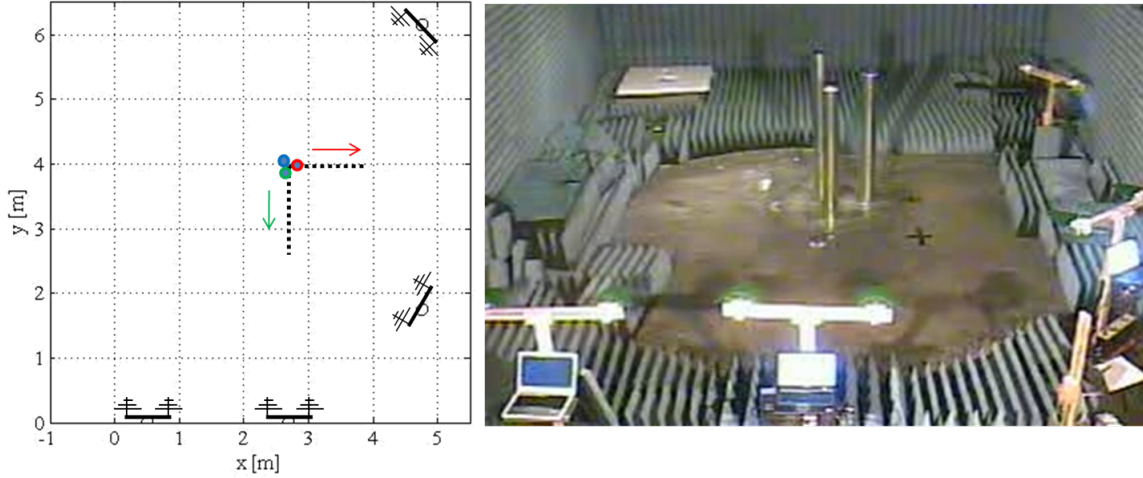


**Figure 27.** Experimental set-up of the multistatic resolution measurements, with both a top view of the experiment layout in the AFIT RCS Range and photo of the actual target scenario.

### 3.4.2 Downrange and Cross-Range Accuracy Experiment.

The primary objective of this experiment is to assess the multistatic range and cross-range accuracy of the network of widely distributed noise radars. In this series of experimental trials, NTR1, NTR2, NTR3 and NTR6 operate as a network of multistatic radar to produce 2-D imagery of the AFIT-missile target. Figure 28 shows the physical layout of the experimental trials and Table 6 captures the corresponding

test matrix.

**Table 6.** Multistatic experimental trials with nodes NTR1, NTR2, NTR3, and NTR6 used to assess the range and cross-range accuracy of the AFIT NoNET. Target locations are measured with respect to a local coordinate system within the AFIT RCS chamber and taken with a laser ranging device with a measurement standard deviation of  $\pm 0.39$  cm.

| Trial         | Systems    | AFIT-missile $(x, y)$ [m] | Comments            |
|---------------|------------|---------------------------|---------------------|
| <i>P4bkg1</i> | NTR1,2,3,6 | -                         | support and chamber |
| <i>P4acc1</i> | NTR1,2,3,6 | (1.441, 2.862)            |                     |
| <i>P4bkg2</i> | NTR1,2,3,6 | -                         | support and chamber |
| <i>P4acc2</i> | NTR1,2,3,6 | (1.976, 4.110)            |                     |
| <i>P4bkg3</i> | NTR1,2,3,6 | -                         | support and chamber |
| <i>P4acc3</i> | NTR1,2,3,6 | (2.692, 4.110)            |                     |

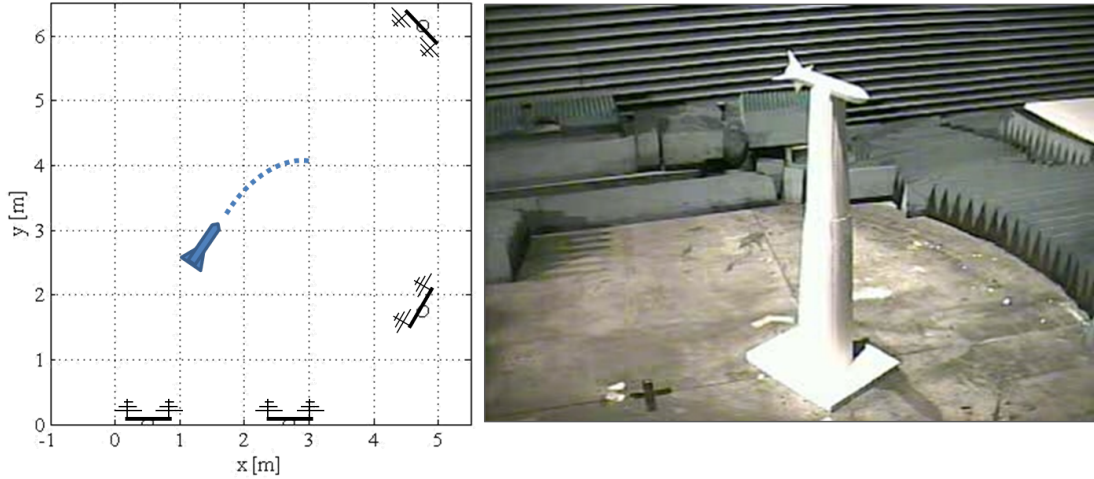


**Figure 28.** Experimental set-up of the multistatic localization accuracy measurements, with both a top view of the experiment layout in the AFIT RCS Range and photo of the actual target scenario using the foam-supported AFIT-missile.

### 3.5 Risk Reduction

In an effort to reduce some of the risk associated with these forms of measurements, two likely sources of experimental error are identified for mitigation prior to conducting the measurements. These potential sources of significant error are the accuracy in target truth data and the interpretation error of the raw target re-



sponse. To minimize the error in physically measuring target locations, the average of three calibrated laser range finder measurements is computed for each trial, which over the course of all experiments had a standard deviation of  $\pm 0.39$  cm. Secondly, the error associated with the interpretation of the raw radar data is mitigated by a post-processing method that performs a target envelope peak detection, a topic that introduces the analysis of results in Chapter IV.

### **3.6 Chapter Conclusion**

An operating level characterization was performed, including RF front-end and direct conversion noise and system response measurements, receiver input power and range calibration procedures. In addition, the results of the characterization will support the computations of theoretical performance predictions in the next chapter. The implementation of monostatic and multistatic distributed and central signal and data processing architectures were described - enabling accuracy and flexibility in the radar operations required for subsequent performance measurements. Finally, designs were presented for demonstrating and evaluating the single node and multistatic localization accuracy and resolution capabilities of the system.

## IV. Analysis of Results

### 4.1 Chapter Overview

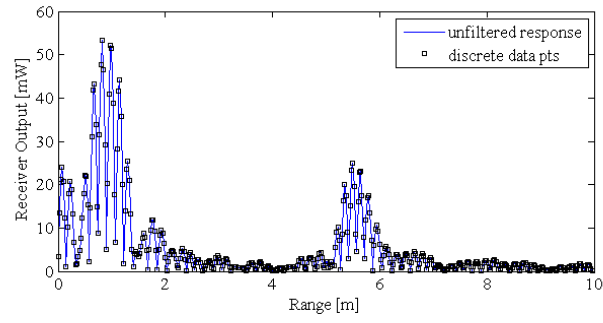
Using the theory presented in Chapter II and the results of the system characterization experiments in Chapter III, predictions of the theoretical range resolution and range accuracy performance are computed. The comparative analysis is performed with respect to those predicted accuracy and resolution performance metrics as each set of experimental data collected in the AFIT RCS chamber is presented. A thorough analysis begins with a clear understanding of some of the additional post-processing developed for the system configurations, which allow more systematic and repeatable evaluations. Additionally, the performance assessments in each section include analysis and discussion of any discrepancies with respect to the predicted performance. The possible impacts that various forms of post-processing and calibration techniques have on the overall system performance are also highlighted. The monostatic evaluation is based on standard accuracy and resolution criteria. Utilizing the imagery analysis tools available in MATLAB<sup>®</sup>, a 2-D localization and resolution performance assessment is conducted. Additionally, both a quantitative and qualitative comparative analysis between multistatic and netted monostatic imagery is performed where the impacts of target ghosting and late scattering phenomenon are assessed.

### 4.2 Monostatic Performance

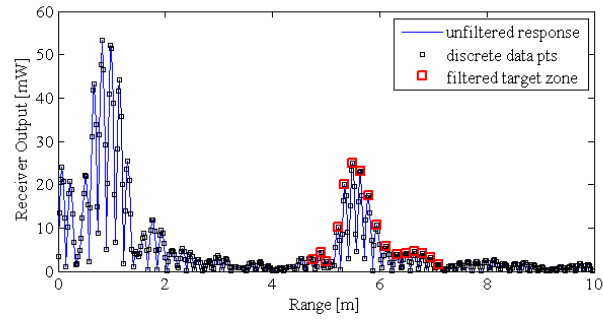
#### 4.2.1 Processing for Evaluation.

For each of the range accuracy and range resolution measurements, a data conditioning tool implemented in MATLAB<sup>®</sup> provides a repeatable estimation process in locating the peak of a target return. As seen in Figure 29, a digital envelope detector filters the high frequency components (using a peak finding function) of the

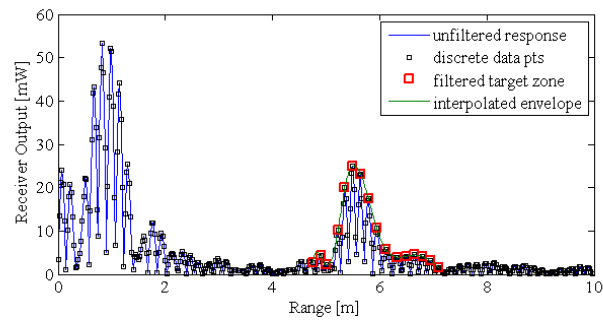
normalized response within the expected target region, smooths the target return via a 300-point spline interpolation to systematically locate the target peak in a response. In addition, two forms of the receiver output are analyzed. The first group is a fully post-processed data set, which incorporates background subtraction to reduce the impacts of the correlated stationary clutter in the measurement. The second is post-processed without the clutter suppression implemented. Experimental results, including descriptive examples of each type of post-processing are presented in the next section.



(a)



(b)



(c)

Figure 29. Features and post-processing evolution of the target response developed for systematic target peak determination required for performance evaluations.

### 4.2.2 Monostatic Range Resolution.

The system response results of the characterization experiment detailed in Section 3.2.1 found the effective bandwidth of the signal to be 185 MHz. Using Equation (9) to solve for the theoretical range resolution,  $\Delta R$  is predicted to be 81.0 cm. The overall results of the range resolution experiment for each type of post-processing are found in Table 7. Figure 30 shows four progressive plots capturing the downrange monostatic target response as the two targets in the scene become resolvable.

As expected the range ambiguity theory of two targets unresolved in range is demonstrated in Figures 31(a) and 31(b), where `dihedral-1` and `dihedral-2` are only separated downrange first by 27.6, then by 78.5 cm. As the position of `dihedral-2` is incremented in range, the point at which a half-power resolution (with respect to truth data) is obtained at  $87.2(\pm 0.8)$  cm and is shown in Figure 31(c). Figure 31(d) then shows a subsequent measurement, when the targets are fully resolved to the noise floor. When background subtraction is not implemented in the post-processing, similar results are measured, but indicate only a slight degradation in resolution performance as seen in Table 7 data. The selected trials in Figure 31 display the same trend with respect to target separation, resulting in a half-power resolution of 92.7 cm without the clutter suppression.

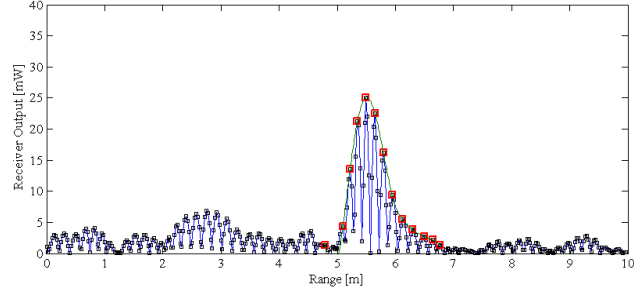
For the measurements obtained using the clutter suppression, the actual distance at which resolution of the two targets is attained is the *res8* trial at a  $87.2(\pm 0.8)$  cm separation. Because a discrete step size is used in the experimental trials, the actual truth-based resolution uncertainty inherits the step size and associated truth data measurement uncertainty as its limiting source of uncertainty, that is  $5.1(\pm 0.8)$  cm. Therefore, the experimentally measured range resolution of the monostatic AFIT NoNET is assessed to be  $87.2(\pm 5.9)$  cm. This is only 6.2 cm larger (just outside the  $\pm 5.9$  cm uncertainty in the measurement) than the theoretical range resolution of

**Table 7.** Monostatic AFIT NoNET range resolution measurement results for both the clutter suppressed measurement, MEAS\*, and the non-clutter-suppressed response measurement, MEAS. As seen in the result columns, the data post-processing identifies peaks that are resolved by at least half power. The target location truth data represents the average of several measurements per location taken with a calibrated laser ranging device accurate to  $\pm 0.39$  cm (based on its average standard deviation across all measurements).

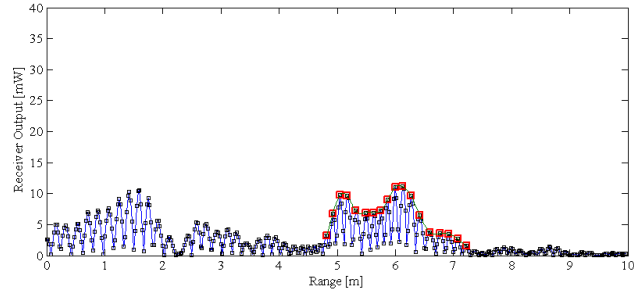
| Run          | dihedral-1<br>[m] | dihedral-2<br>[m] | MEAS* [m] |          | MEAS [m] |          |
|--------------|-------------------|-------------------|-----------|----------|----------|----------|
|              |                   |                   | 1st peak  | 2nd peak | 1st peak | 2nd peak |
| <i>res1</i>  | 5.282             | 5.291             | 5.252     |          | 5.309    |          |
| <i>res2</i>  | 5.282             | 5.445             | 5.408     |          | 5.394    |          |
| <i>res3</i>  | 5.282             | 5.558             | 5.511     |          | 5.538    |          |
| <i>res4</i>  | 5.282             | 5.761             | 5.324     |          | 5.462    |          |
| <i>res5</i>  | 5.282             | 5.881             | 5.776     |          | 5.766    |          |
| <i>res6</i>  | 5.282             | 6.067             | 6.051     |          | 5.650    |          |
| <i>res7</i>  | 5.282             | 6.103             | 6.165     |          | 5.689    |          |
| <i>res8</i>  | 5.282             | 6.154             | 5.214     | 6.193    | 6.172    |          |
| <i>res9</i>  | 5.282             | 6.209             | 5.270     | 6.179    | 5.382    | 6.145    |
| <i>res10</i> | 5.282             | 6.332             | 5.177     | 6.371    | 5.617    | 6.350    |
| <i>res11</i> | 5.282             | 6.462             | 5.229     | 6.518    | 5.422    | 6.482    |
| <i>res12</i> | 5.282             | 6.686             | 5.230     | 6.514    | 5.367    | 6.524    |
| <i>res13</i> | 5.282             | 6.726             | 5.187     | 6.734    | 5.513    | 6.718    |

81.0 cm. As developed in Chapter II, the theoretical prediction is expected to be a performance lower bound in resolution, so this larger measured resolution is expected.

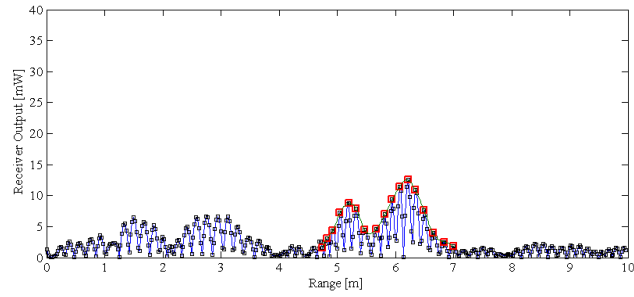
When not performing the background subtraction the measured resolution is 98.9( $\pm 6.3$ ) cm. There are two likely reasons for the reduced resolution when the clutter suppression processing is not employed. The first is the reduced SNR (where the mean noise power is inclusive of clutter, interference, and noise) which reduces the accuracy of the measurements. In addition, the resolved clutter that exists within the ranges of interest impacts the shaping of the target envelopes and peak location estimation. More importantly, clutter could be co-located with the range sidelobes between the target responses, adding to their apparent power and reducing the target resolvability.



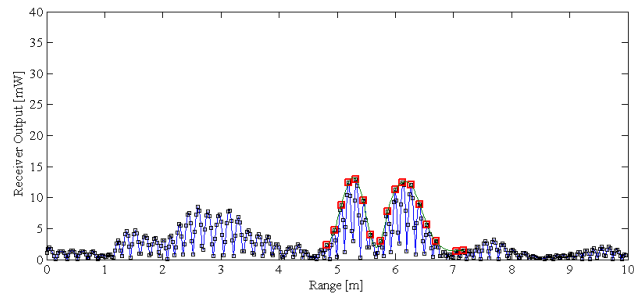
(a)



(b)

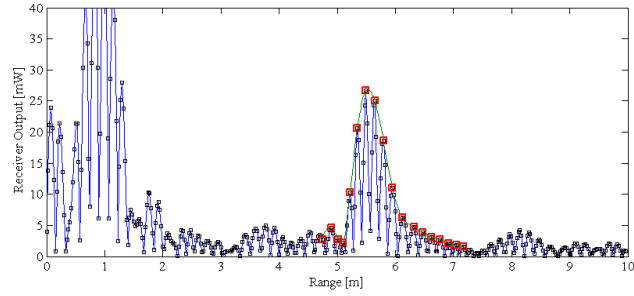


(c)

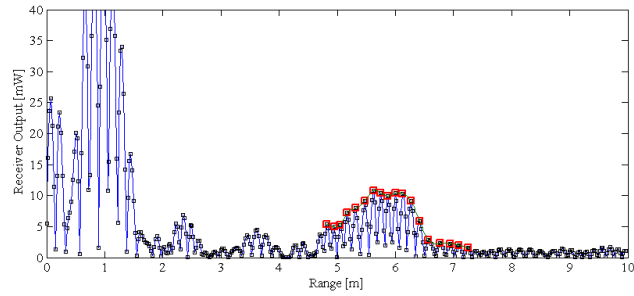


(d)

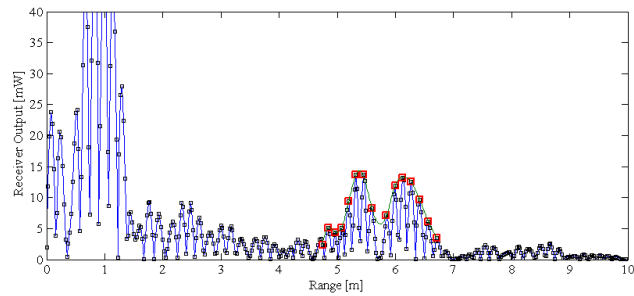
Figure 30. Monostatic range resolution results without clutter suppression when dihedral-1 and dihedral-2 are separated by a true distance of (a)  $27.6(\pm 0.8)$  cm when the skirts of their main peaks still combine with enough power to maintain a single smooth peak, (b)  $78.5(\pm 0.8)$  cm and prior to being resolved, (c)  $87.2(\pm 0.8)$  cm at the point of being resolved with respect to the half-power criteria, and (d)  $92.7(\pm 0.8)$  cm demonstrating fully resolved targets.



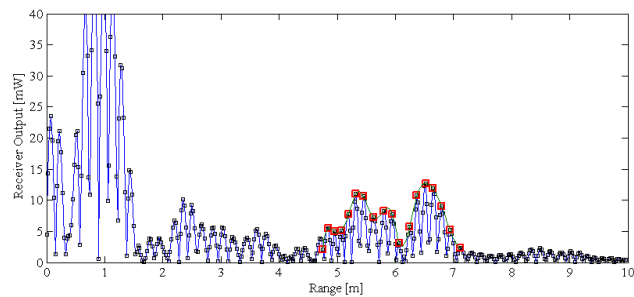
(a)



(b)



(c)



(d)

Figure 31. Sample monostatic range resolution results with clutter suppression disabled and dihedral-1 and dihedral-2 are separated by (a)  $27.6(\pm 0.8)$  cm where both of their main peak skirts still combine with enough energy to maintain an apparent single smooth peak, (b)  $78.5(\pm 0.8)$  cm and prior to being resolved, (c)  $92.7(\pm 0.8)$  cm at the point of being resolved with respect to the half-power criteria, and (d)  $1.404(\pm 0.8)$  m fully resolved and showing a potential false target due to ground bounce multipath from dihedral-1.



### 4.2.3 Monostatic Range Accuracy.

Predicted monostatic range accuracy of the noise radar is based on the estimate of the Cramér-Rao Lower Bound developed in Chapter II. The results of the system characterization experiments for effective 3-dB bandwidth ( $B = 185$  MHz) is used to compute a  $B_{rms} = 1.81B = 335$  MHz. This  $B_{rms}$  and the calculated SNR of the calibrated target response of 19.0 dB are used to solve for the inequality expressed in Equation (19). The theoretical lower bound of the standard deviation in time delay error,  $\sigma_\tau$ , is predicted to be 0.302 ns.

The overall results for the two processing conditions are presented in Table 8. The results are consistent with the expected uncertainty present in radar range measurements, demonstrated by the existence of random-like error in the measurements. Of great interest is a comparison with the predicted lower bound of the range accuracy. It is found that the standard deviation of the measurement error satisfies the CRLB-derived inequality given by Equation (17). Figure 32 is a graph of the *acc3* measurements from Table 8 converted to the measured time delay, where the standard deviation of time delay error,  $\sigma_\tau$ , is found to be 0.319 ns (or 4.78 cm). For direct comparison of the predicted vs measured accuracy performance, the graph shows the measured data statistics plotted along with the measurement truth data and CRLB predicted time delay error. Furthermore, a negative (early) mean error bias of -37 ps (or -0.55 cm) is measured. When not utilizing the clutter suppression,  $\sigma_\tau$  of the measured data is 0.453 ns (or 6.79 cm), and shows a positive mean error bias of +0.422 ns (or +6.32 cm). Several examples of the monostatic range accuracy measurements are shown in Figure 33.

As discussed in the range accuracy theory of Chapter II, derivation of the CRLB-based estimate assumes the radar an unbiased estimator. The impact of any bias not removed in the system calibrations or introduced in the post-processing results

**Table 8.** Monostatic range accuracy measurement results for both the post-processed (clutter suppression and peak detection) measurement, MEAS\*, and the measured peak detection without background subtraction, MEAS. The target location truth data represents the average of three measurements per trial taken with a calibrated laser ranging device accurate to  $\pm 0.39$  cm (based on its average standard deviation across all measurements)

| Run          | dihedral-1 [m] | MEAS* [m] | MEAS [m] |
|--------------|----------------|-----------|----------|
| <i>acc1</i>  | 5.674          | 5.678     | 5.753    |
| <i>acc2</i>  | 5.723          | 5.754     | 5.801    |
| <i>acc3a</i> | 5.774          | 5.757     | 5.701    |
| <i>acc3b</i> | 5.774          | 5.746     | 5.701    |
| <i>acc3c</i> | 5.774          | 5.831     | 5.706    |
| <i>acc3d</i> | 5.774          | 5.752     | 5.685    |
| <i>acc3e</i> | 5.774          | 5.773     | 5.712    |
| <i>acc3f</i> | 5.774          | 5.790     | 5.712    |
| <i>acc3g</i> | 5.774          | 5.724     | 5.702    |
| <i>acc3h</i> | 5.774          | 5.781     | 5.701    |
| <i>acc3i</i> | 5.774          | 5.796     | 5.764    |
| <i>acc3j</i> | 5.774          | 5.662     | 5.681    |
| <i>acc3k</i> | 5.774          | 5.841     | 5.755    |
| <i>acc4</i>  | 5.825          | 5.860     | 5.821    |
| <i>acc5</i>  | 5.871          | 5.830     | 5.807    |
| <i>acc6</i>  | 5.922          | 5.924     | 5.925    |
| <i>acc7</i>  | 6.412          | 6.398     | 6.437    |

in a reduction in range accuracy relative to the CRLB. As previously mentioned, analysis of the co-range measurements 3a-3k reveal some error bias in the measurements. Whether the measured bias is a true bias is not certain. The laser ranging measurement used as the experimental truth data has a  $\pm 0.39$  cm uncertainty in its measurements, which is less than the measured mean error of 0.55 cm. Therefore, this assessed bias is likely a true system bias that has not been adequately calibrated out. Another assumption made when forming the CRLB estimate, and one that is contributing to the larger measured accuracy error, is the  $B_{rms}$  estimate. The assumption is made that the shape of the spectrum is rectangular (that is, band-limited and having uniform power spectral density within its occupied bandwidth). The non-uniformly filled spectrum of the received signal results in the true  $B_{rms}$  being less than

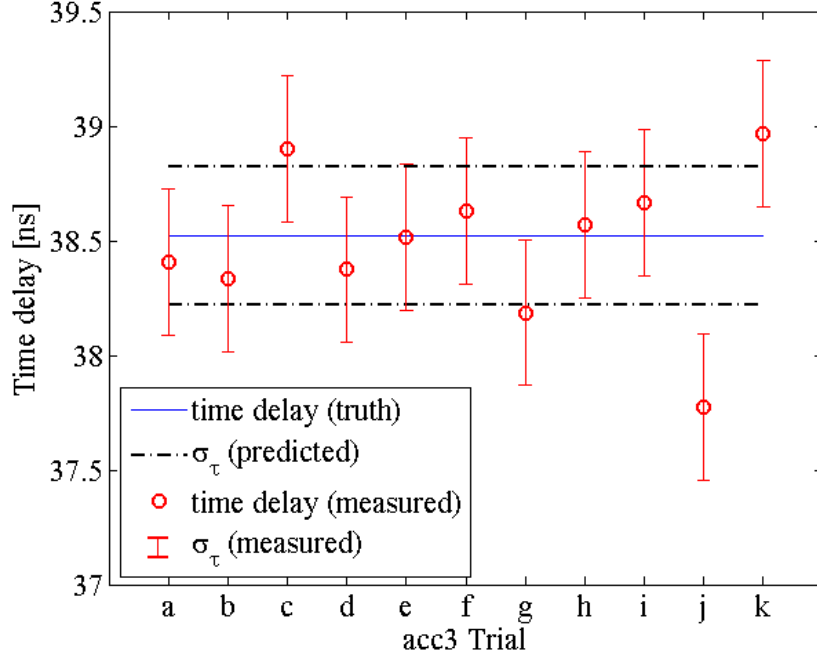
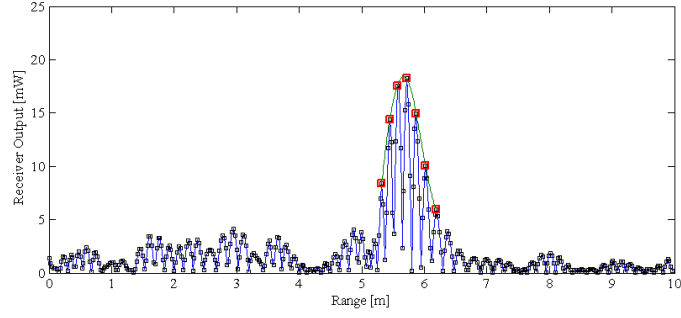
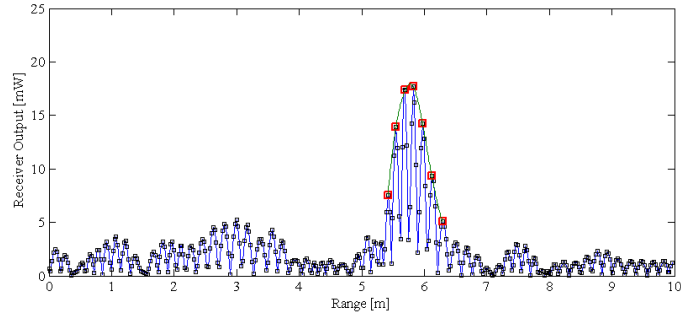


Figure 32. Plot of the range accuracy results of the *acc3* trials presented in time delay units. Included for comparison, the error bars show the measured and CRLB-predicted standard deviations of the time delay error. Though not shown in the figure, the truth data gathered with the laser ranging device has an experimentally computed standard deviation of  $\pm 0.39$  cm (or 0.03 ns in time delay units).

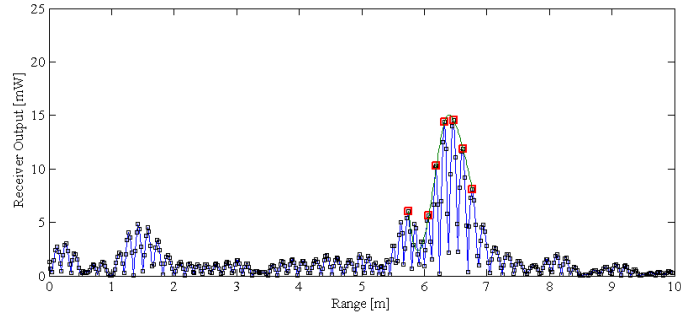
that used in the theoretical computation, which would produce an optimistic accuracy prediction. But these less than ideal parameters can be expected in real-world systems and validate the *lower bounded* quality of the analytic prediction.



(a)

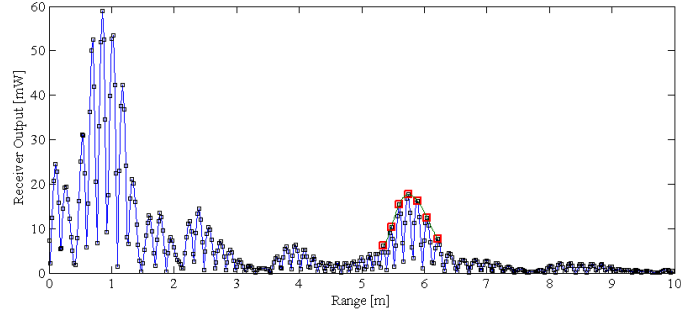


(b)

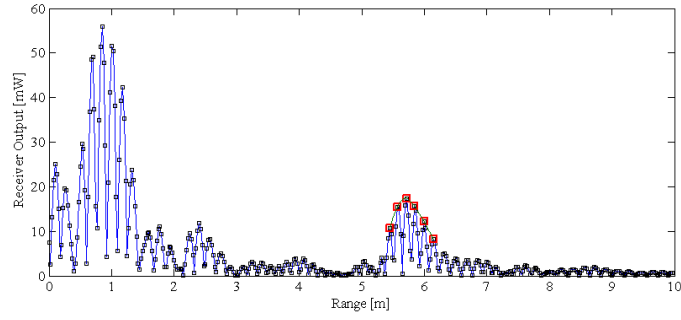


(c)

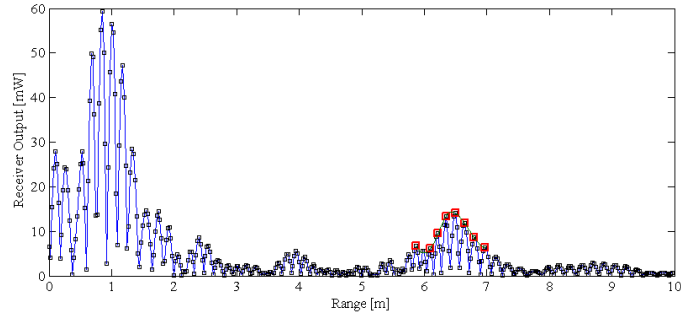
Figure 33. Several range accuracy results of monostatic measurements using with clutter suppression post-processing and test target dihedral-1 downrange at (a) 5.674 m, (b) 5.774 m, and (c) 6.412 m (each with a  $\pm 0.39$  cm standard deviation).



(a)



(b)



(c)

Figure 34. Range accuracy monostatic measurements using NTR3 with clutter suppression and test target dihedral-1 downrange at (a) 5.674 m, (b) 5.774 m, and (c) 6.412 m (each with a  $\pm 0.39$  cm standard deviation).

### 4.3 Multistatic Performance

The results of the multistatic experiments are evaluated to assess the 2-dimensional localization performance of the AFIT NoNET when operating with four radar nodes. Post-processing, including clutter suppression via background subtraction and digital envelope filtering, is implemented on the data for each individual multistatic channel prior to converting the downrange profile to the referenced 2-D coordinate plane formed by the AFIT RCS chamber. Using the geometry computations presented in Chapter II and knowledge of each node's position, the multistatic isorange response is mapped into the chamber coordinate plane at the central processor, translating and rotating each channel's isorange contours as necessary. An example of the array of 2-dimensional images formed from each discrete channel is seen in Figure 35. The multilateration image fusion technique invokes the linear combination function available as part of the Image Processing Toolbox<sup>TM</sup> in MATLAB<sup>®</sup>R2009a. In terms of imagery processing, no compensations are made for the propagation  $1/R^4$  power density loss in the radar measurements. While future studies may investigate possible advantages in this form of balancing, the natural weighting that these losses provide may be beneficial. Simply stated, the shorter range channels will tend to have higher available SNR, and therefore the more accurate measurements will weigh into the image with more intensity. Therefore, the full multistatic image product consists of a linear combination of the 4 monostatic images and 12 bistatic images. To compare the results to another common form of distributed radar systems, results are also presented for the netted monostatic response, where only the 4 monostatic channels are linearly combined to form the image product. To be clear, the same data collected from each trial is being processed in two different capacities - the multistatic central processing fuses the additional bistatic channels with the monostatic channels (those being used by the netted monostatic processing).

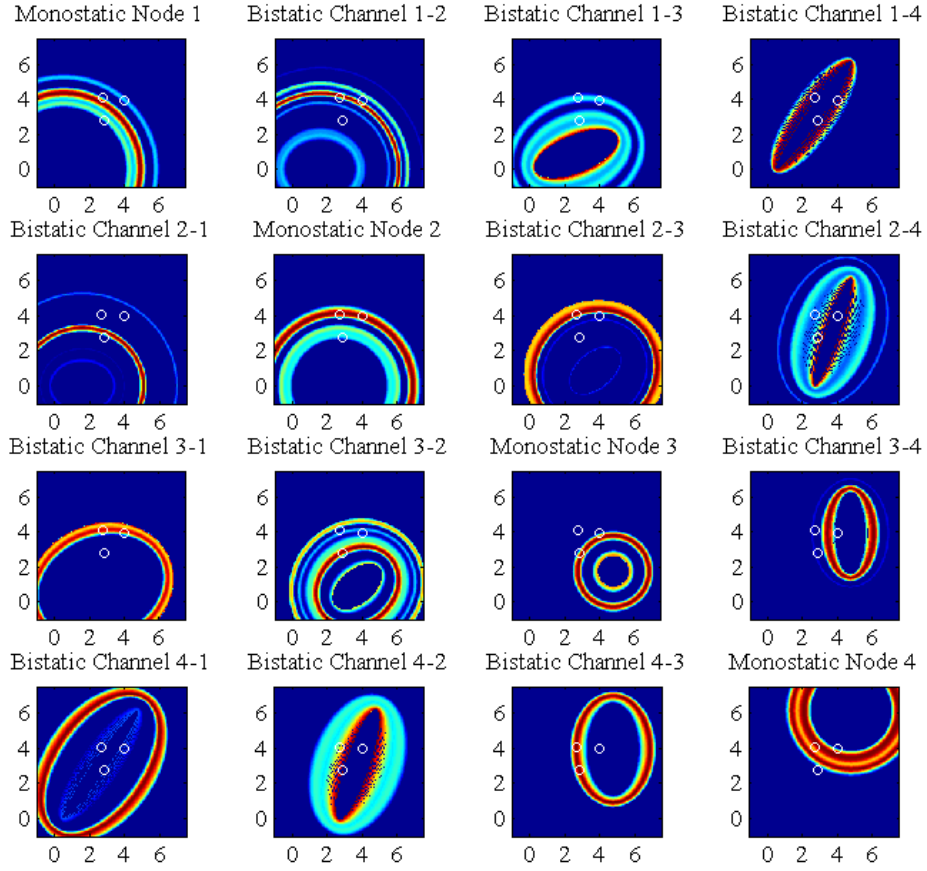


**Figure 35.** An example array of the discrete images showing each of the available 16 multistatic channels prior to central processing fusion. Target locations are represented by white circles.

Tools for locating nearest maximum pixel intensities to a specified target location and basic image thresholding performed with colormap scaling are also available in the MATLAB<sup>®</sup> toolbox. These are used to objectively assess the performance of target estimation metrics in the multistatic and netted monostatic images. Because non point-like targets are used in this series of experiments coupled with the image fusion from diverse aspects, a simplification in determining truth target location is required. A single pixel is identified as a target's center of mass and all error measurements are assessed with respect to that pixel.

Finally, an important distinction must be reiterated before assessing the results. Distributed estimation represents a separate class of measurement objectives than distributed detection [8]. The core principle of detection theory, which focuses on maximizing signal-to-noise ratio at various stages of processing for a final decision regarding target presence, is greatly concerned with energy on target and energy received with respect to mean noise energy. Distributed estimation, which is the focus of this research, assumes the target is detected and is concerned with target parameter estimation. Therefore, analysis only includes general observations regarding target detection, the issues of potential target ghosts (false targets), and power levels in the imagery. Certain aspects of the localization performance assessments that account for power, like half-power resolution criteria, are assessed.

#### **4.3.1 Assessment of Range and Cross-Range Resolution.**

The series of multistatic images seen in Figures 36-40 demonstrate the target resolution capabilities of the AFIT NoNET and are used to assess the range and cross-range resolution performance of the configuration. For a comparative analysis, the corresponding netted monostatic imagery is also shown for each trial.

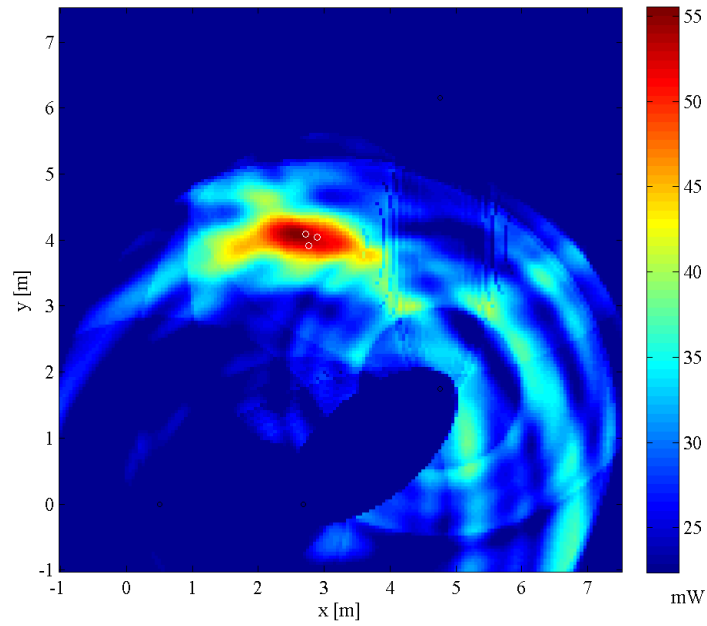
For each type of processing in this series of resolution-focused trials, the imagery products are displayed with an intentionally dynamic colormap power scale using the built-in *caxis* functions in MATLAB<sup>®</sup>. In general, implementing a continuous false alarm rate (CFAR) algorithm in the image fusion processing (a candidate for future research in AFIT NoNET distributed detection) would allow a more dynamic thresholding, and therefore impact the resolution assessment. Here, the dynamic scaling is used to aid in assessing the half-power target resolution criteria. The maximum of the scale is set by the highest power level and the minimum set by an estimate of the average noise floor for that image (a basic CFAR-like post-processing).



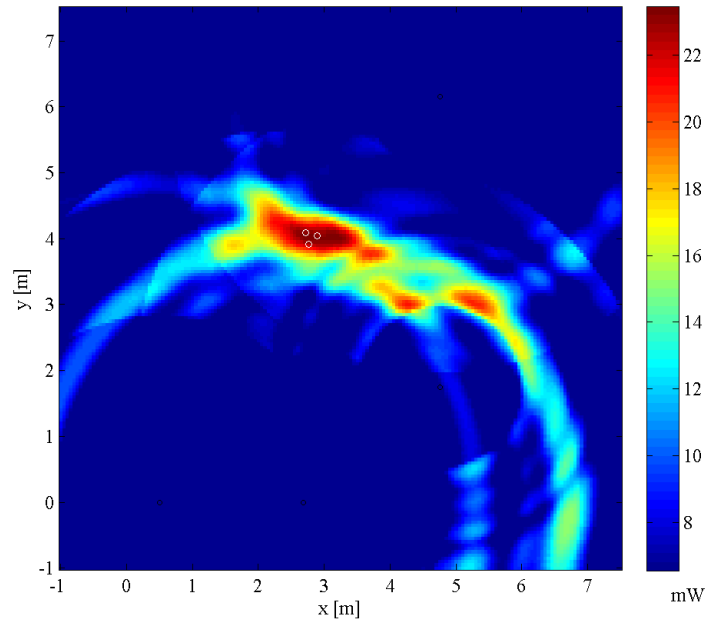
Based on a strict half-power resolution criteria, downrange discrimination between `cylinder-1` and `cylinder-2` does not occur until Trial 5 for both the multistatic and netted monostatic processing, where the targets are separated by approximately 1.45 m. Cross-range discrimination is only attained with the netted monostatic configuration during Trial 4, when `cylinder-1` and `cylinder-3` are separated by approximately 1.29 m. Although obvious multiple target peaks exist and are clearly discernible in the imagery, the multistatic configuration does not achieve a cross-range resolution of `cylinder-1` and `cylinder-3` as defined by the half-power criteria. If a more robust CFAR algorithm were implemented, or simply an intelligent qualitative assessment of the imagery, the targets are discernible for the multistatic processing in Trial 4. This pertains to a cross-range resolution of approximately 1.29 m, like that of the netted monostatic.

There are several possible reasons for this outcome, all of which pertain to the design of the experiment. As was expected, the complex multi-target scene creates a variety of scattering mechanisms that prove quite dynamic through the progression of the trials. The sheet metal ducts used as the target cylinders are not perfectly cylindrical, nor could they be made to stand in the same vertical plane for each trial. Additionally, the simultaneous repositioning of `cylinder-2` and `cylinder-3` create a dynamic target scene that appears to bring the backscatter and forward scattering components in and out of neighboring target channels, while late scattering mechanisms form target ghosts in several instances. Another reason for not obtaining a half-power depth of resolution may simply be a SNR issue. At such large wavelengths and being horizontally polarized, the RCS predictions may be overly optimistic for these cylinder diameters. This would further explain some of low power levels measured in several of the trials, which make the half-power depth of resolution criteria difficult to attain.

Possible improvements to the resolution performance experiments would be the use of the chamber's string system for hanging target spheres and performing the downrange and cross-range experiments independently. Finally, the test scenario could be staged to have sets of perfectly orthogonal aspect angles with respect to the target to insure earliest possible target discrimination. However, that ideal case was intentionally avoided to create a more realistic engagement.

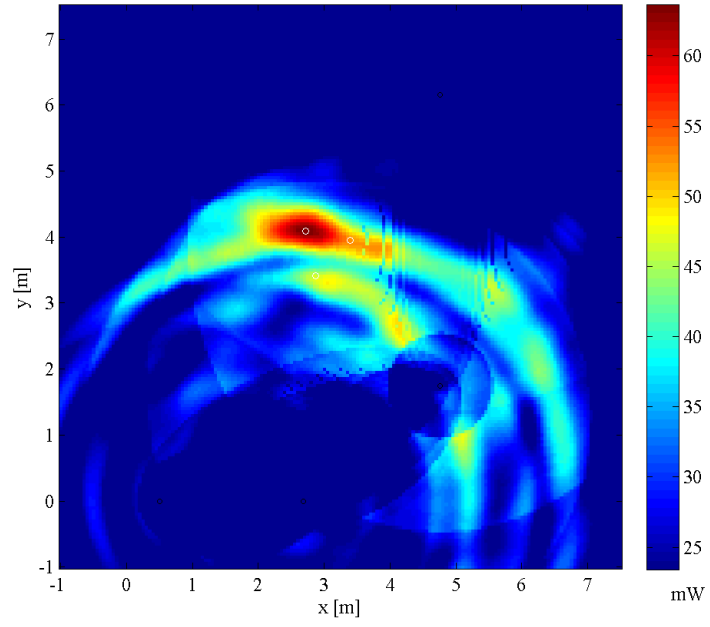


(a)

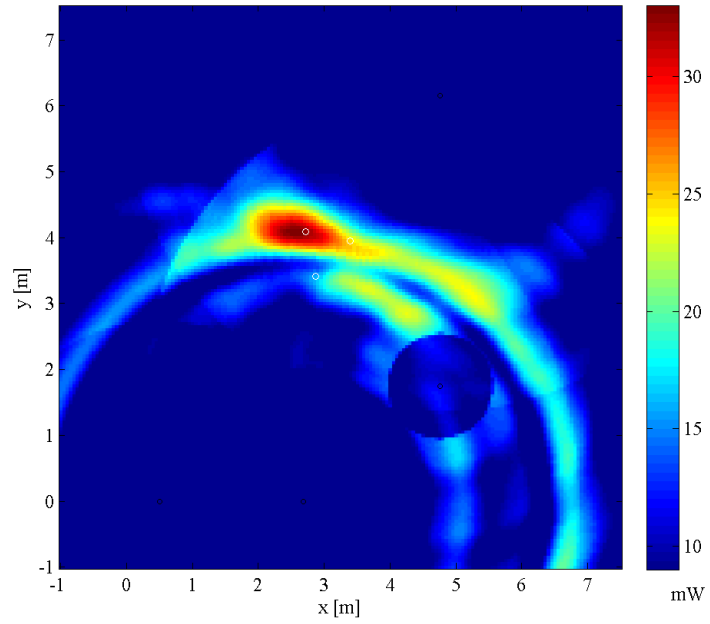


(b)

Figure 36. Experiment *P3res1* (Trial 1) imagery products of the (a) multistatic and (b) netted monostatic measurements used to assess the range and cross-range accuracy of the AFIT NoNET. The locations (but not sizes) of the three cylinder targets are represented by the white circles and the radar nodes by black circles.

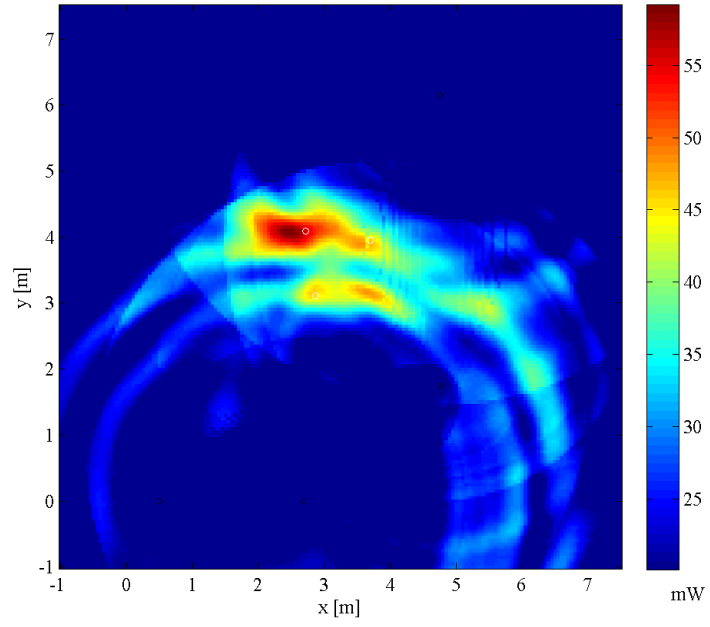


(a)

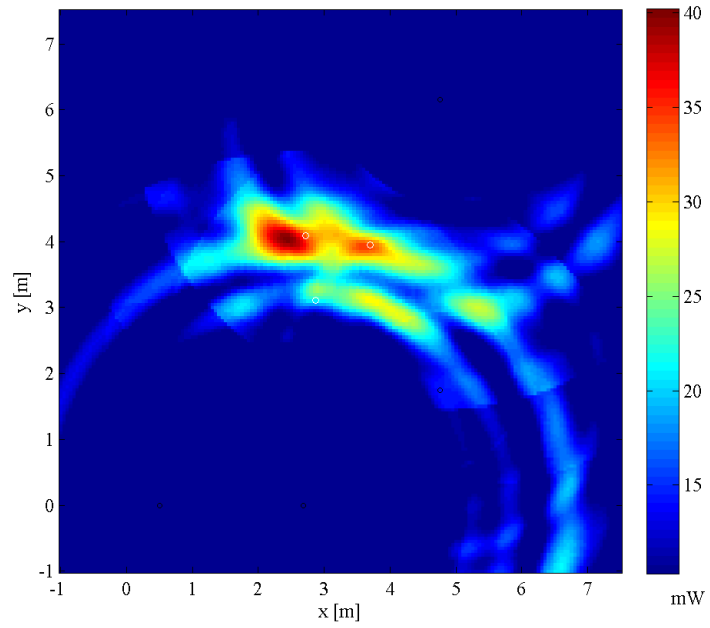


(b)

**Figure 37.** Experiment *P3res2* (Trial 2) imagery products of the (a) multistatic and (b) netted monostatic measurements used to assess the range and cross-range accuracy of the AFIT NoNET.

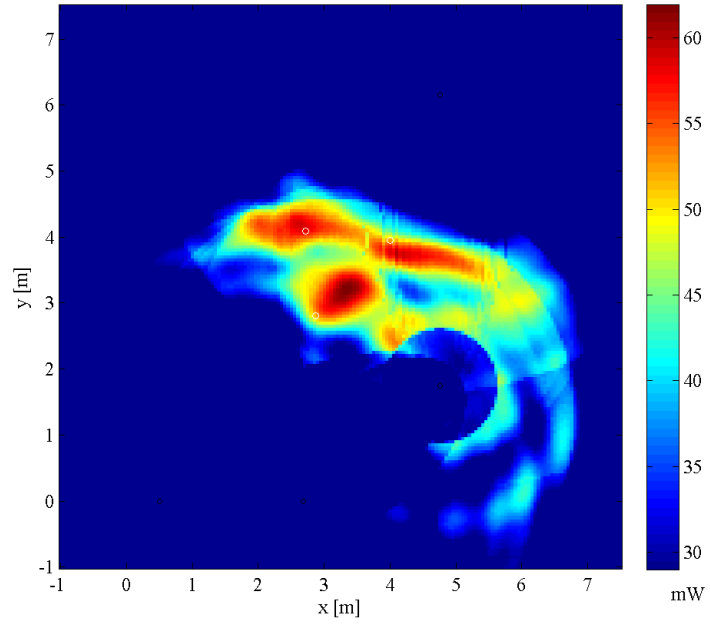


(a)

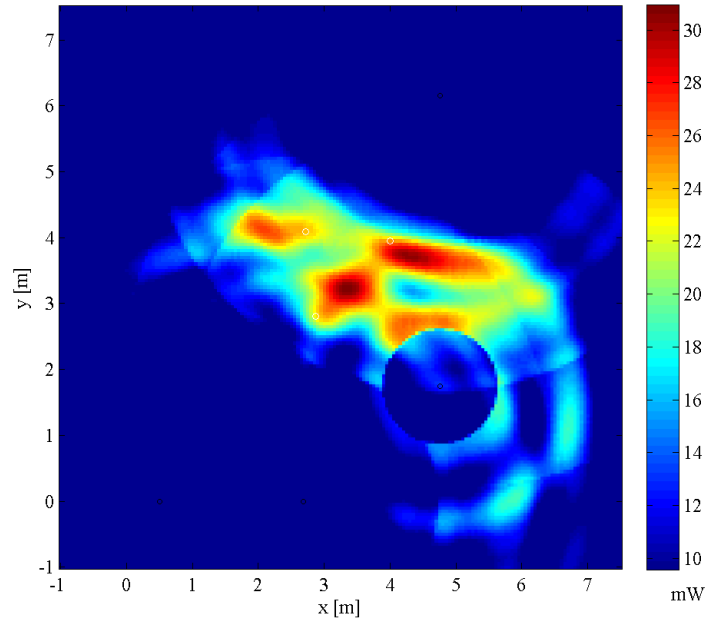


(b)

**Figure 38. Experiment  $P3res3$  (Trial 3) imagery products of the (a) multistatic and (b) netted monostatic measurements used to assess the range and cross-range accuracy of the AFIT NoNET.**

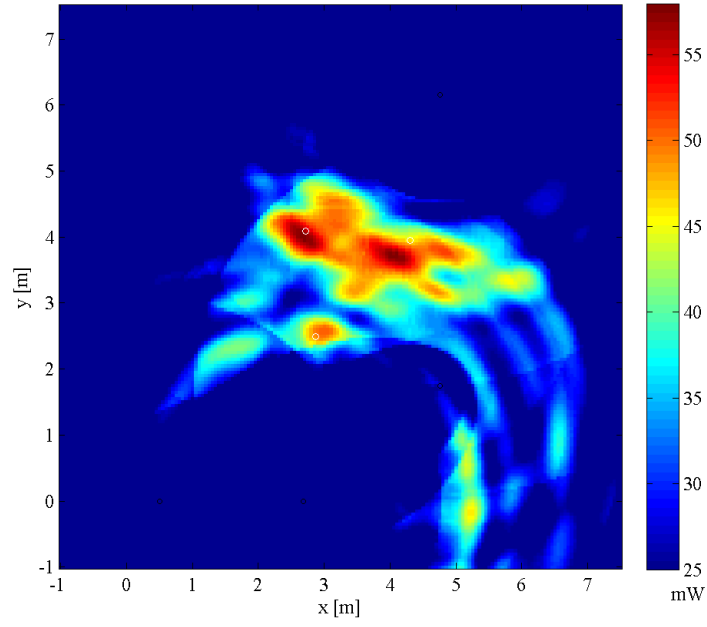


(a)

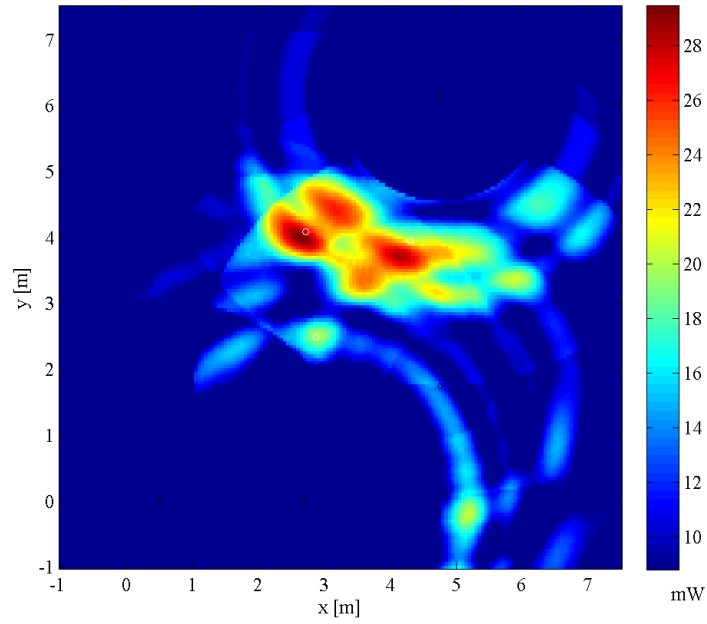


(b)

**Figure 39.** Experiment *P3res4* (Trial 4) imagery products of the (a) multistatic and (b) netted monostatic measurements used to assess the range and cross-range accuracy of the AFIT NoNET.



(a)



(b)

**Figure 40.** Experiment *P3res5* (Trial 5) imagery products of the (a) multistatic and (b) netted monostatic measurements used to assess the range and cross-range accuracy of the AFIT NoNET.

### 4.3.2 Assessment of Range and Cross-Range Accuracy.

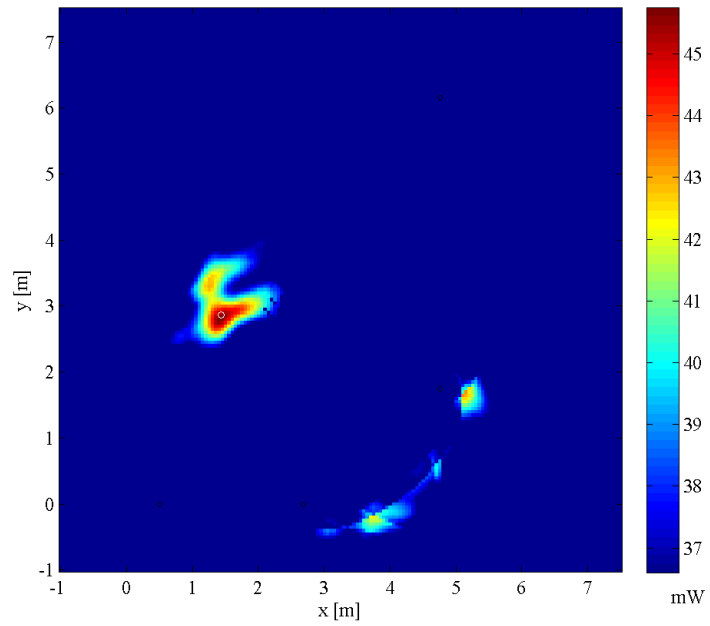
The imagery products of the 2-dimensional localization accuracy measurements are used to gather the downrange, cross-range, and distance error for each experimental trial. The multistatic images seen in Figures 41-43 are used to assess the the range and cross-range accuracy of the AFIT NoNET. Again, for direct comparison in each scenario the corresponding netted monostatic images are shown, as well.

For each type of processing in this series of accuracy-focused trials, the imagery products are displayed with a colormap scale minimum threshold of 0.7 of the imagery peak as emulation of a detection CFAR algorithm. The corresponding results of this series of tests are listed in Table 9. The resulting error statistics are computed for each of the types of measurements. As expected some of the previously described scattering phenomenon, like the multipath ground plane effect, appear in the imagery. The first trial is an obvious outlier for the netted monostatic processing, where a combination of two factors are assessed as skewing the results. First, the strong target ghost in Figure 41(b) at approximately (0.8, 3.3) is the product of the late scattered energy observed in both of the nearby monostatic channels, especially node 2 (as seen in Figure 44). This is assessed as a possible ground plane effect ghost target, based on the indirect path lengths for a 1.37-m target height and 1.21-m antenna heights at a range of only 2.90 m. The second problem with this particular measurement was the anomalous missed target estimation by node 3. This lack of data in one channel and strong, but late scattering information in two other channels skewed the fused target energy of the true target, which caused the large errors in the localization.

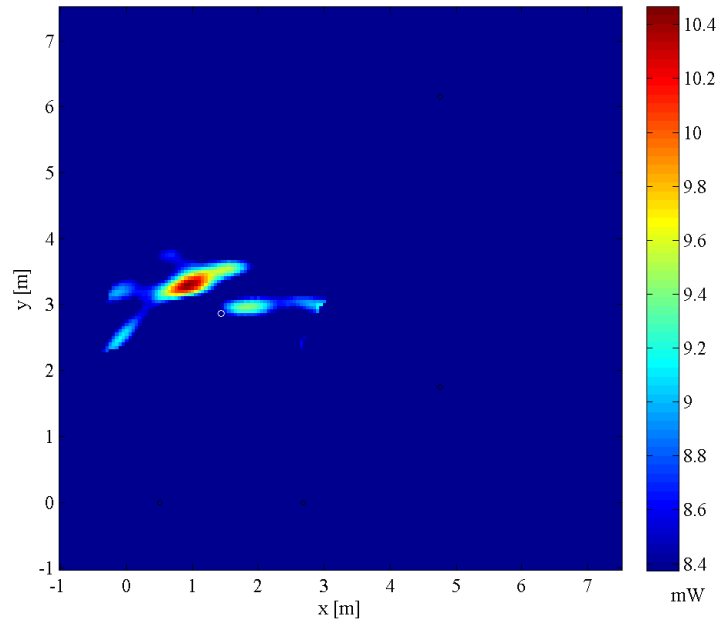


**Table 9.** Multistatic and Netted Monostatic measurement results are used to assess the downrange and cross-range accuracy of the system. The localization error is measured with respect to the pixel identified as the target’s center of mass for each run. Only the local peak with the greatest magnitude is considered in the assessment. The target location truth data represents the average of three measurements per trial taken with a calibrated laser ranging device accurate to  $\pm 0.39$  cm (based on its average standard deviation across all measurements)

| Multistatic  | Target<br>( $x, y$ ) [m] | Measured Peak<br>( $x, y$ ) [m] | power [mW] | Component Error<br>( $\Delta x, \Delta y$ ) [cm] | $ Error $<br>[cm] |
|--------------|--------------------------|---------------------------------|------------|--|-------------------|
| $P4acc1$     | (1.45, 2.85)             | (1.45, 2.85)                    | 45.8       | (−10, −5)  | 11                |
| $P4acc2$     | (2.00, 4.15)             | (2.00, 4.10)                    | 45.2       | (0, −5)  | 5                 |
| $P4acc3$     | (2.70, 4.15)             | (2.60, 4.20)                    | 39.5       | (−5, 5)  | 7                 |
|              |                          |                                 | mean error | (−5, −1.7)                                       | 7.7               |
|              |                          |                                 | std error  | (5, 5.8)   | 3.1               |
| Netted Mono. | ( $x, y$ ) [m]           | ( $x, y$ ) [m]                  | power [mW] | ( $\Delta x, \Delta y$ ) [cm]                    | [cm]              |
| $P4acc1$     | (1.45, 2.85)             | (1.45, 2.85)                    | 10.5       | (−50, 45)  | 67                |
| $P4acc2$     | (2.00, 4.15)             | (2.05, 4.10)                    | 9.7        | (5, 0)   | 5                 |
| $P4acc3$     | (2.70, 4.15)             | (2.65, 4.05)                    | 8.6        | (−5, −10)  | 11                |
|              |                          |                                 | mean error | (−16.7, 11.7)                                    | 27.7              |
|              |                          |                                 | std error  | (29.3, 23.6)                                     | 34.2              |

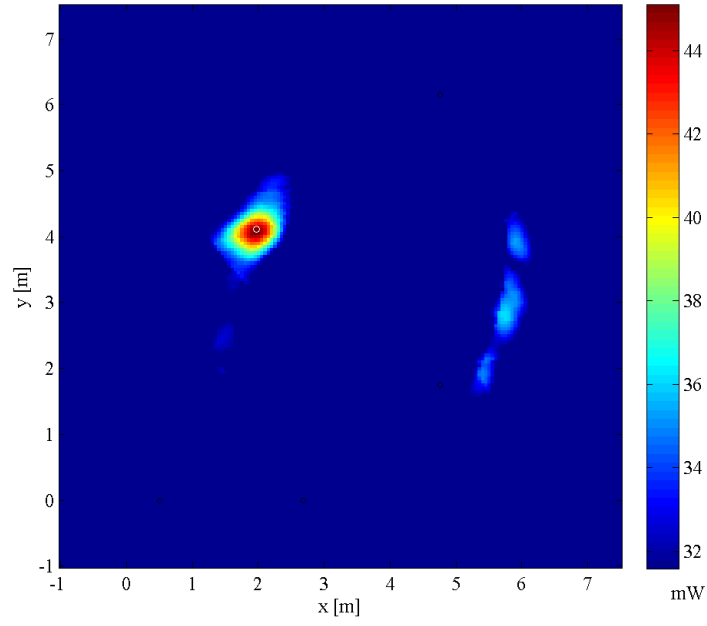


(a)

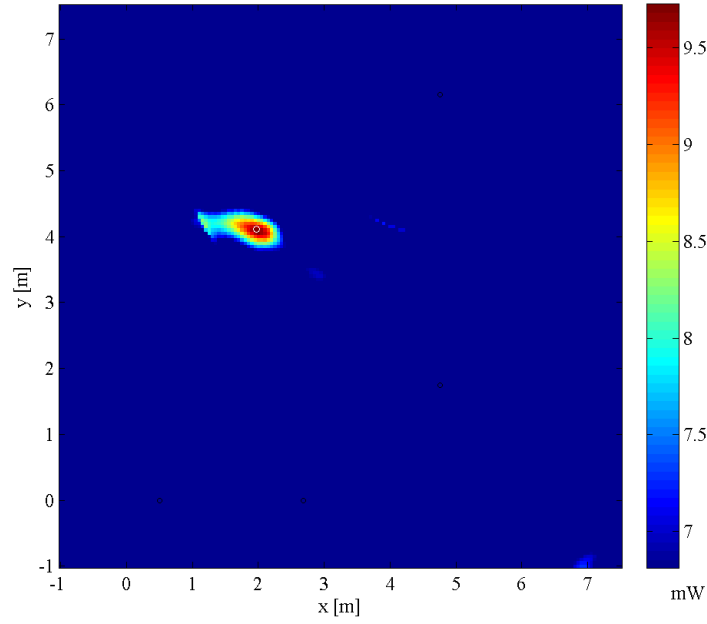


(b)

Figure 41. Imagery products of the first trial of (a) multistatic and (b) netted monostatic measurements used to assess the range and cross-range accuracy of the AFIT NoNET. The center of mass of the AFIT-missile target location is represented by the white circle at (1.441, 2.862). AFIT NoNET nodes are represented by the black circles.

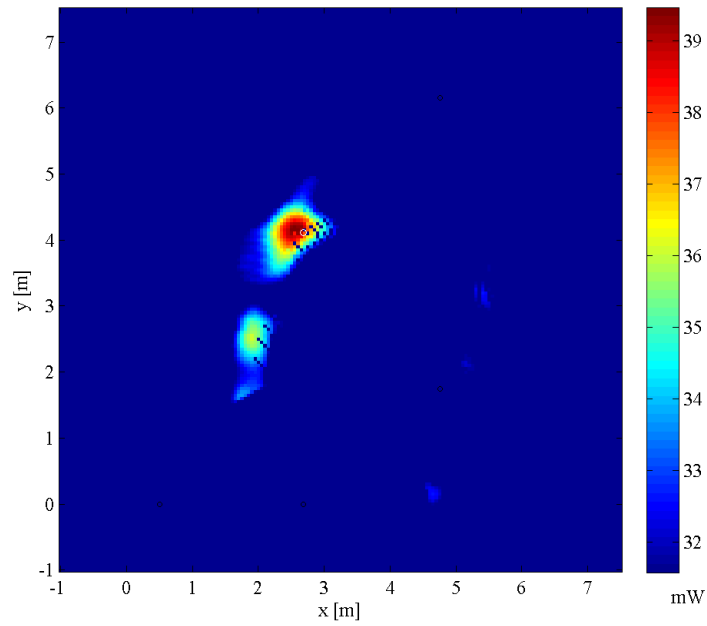


(a)

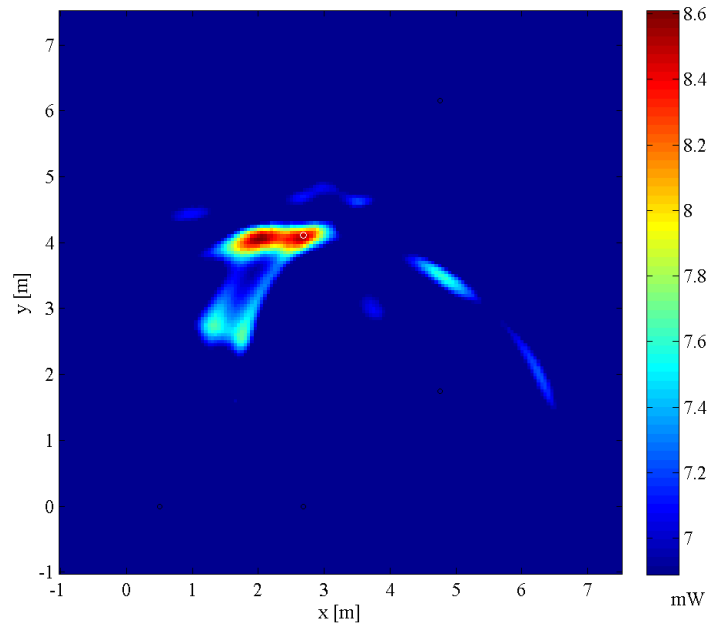


(b)

Figure 42. Imagery products of the second trial of (a) multistatic and (b) netted monostatic measurements used to assess the range and cross-range accuracy of the AFIT NoNET. The center of mass of the AFIT-missile target location is represented by the white circle at (1.976, 4.110). AFIT NoNET nodes are represented by the black circles.



(a)



(b)

**Figure 43.** Imagery products of the third trial of (a) multistatic and (b) netted mono-static measurements used to assess the range and cross-range accuracy of the AFIT NoNET. The center of mass of the AFIT-missile target location is represented by the white circle at (2.692, 4.110). AFIT NoNET nodes are represented by the black circles.

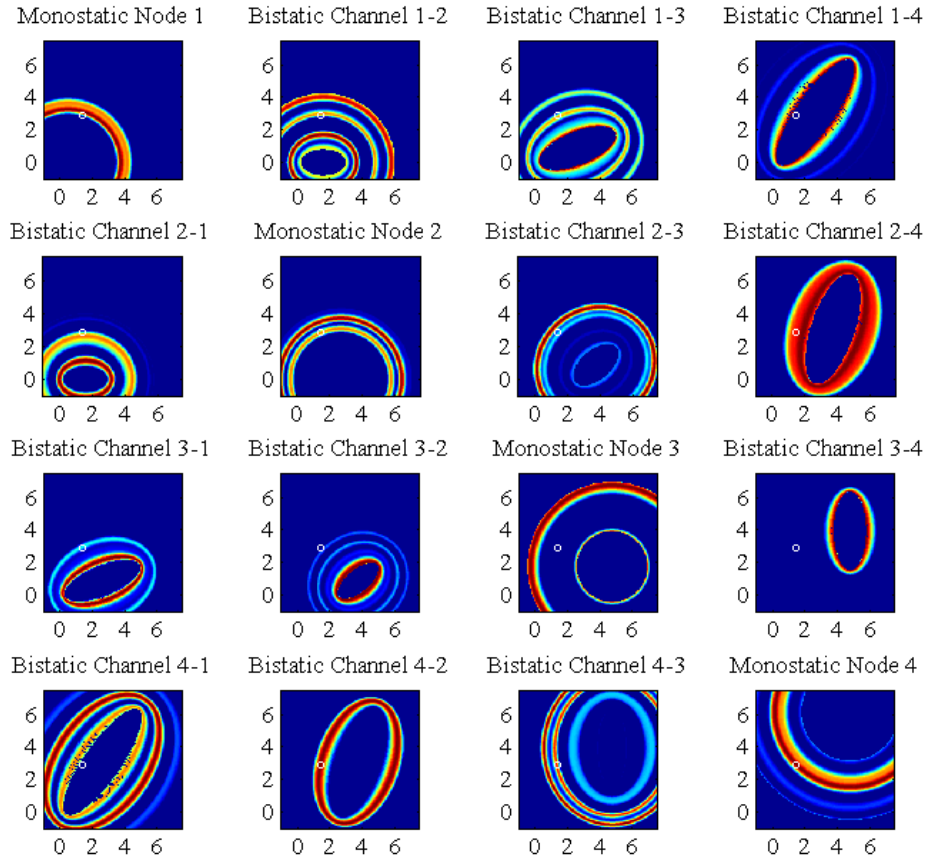


**Figure 44.** The discrete images of the first trial in the multistatic accuracy experiment using the AFIT-missile show each of the available 16 multistatic channels prior to central processing fusion. Of interest is the late scattering energy in Monostatic Nodes 1 and 2, and the anomalous miss by Monostatic Node 3. Some bistatic channels contribute negatively, for example channel 3-4, but are effectively averaged out when 16 channels are fused in the final multistatic image seen in Figure 41(a).

## 4.4 Chapter Conclusion

The overall localization performance evaluations of both the monostatic and multistatic system configurations were conducted. The results of the measured range resolution and range accuracy of the monostatic evaluations agreed well with the theoretical performance predictions. The results of the multistatic experiments demonstrated the additional 2-dimensional localization accuracy in cross-range, as well as strong indicators of the cross-range resolution potential of the AFIT NoNET design. Possible sources of error in the multistatic resolution experiment were identified for improvement. Similarly, specific observations in the discrete channel imagery were used to assess the significant sources of measurement error in the netted monostatic accuracy results. Overall, the findings demonstrate the tremendous localization performance of the AFIT NoNET and the advantages of exploiting all available multistatic channels as compared to a netted monostatic configuration.

## V. Conclusions

### 5.1 Chapter Overview

To see, yet not be seen - a skill as old as war. The problem of delivering accurate, target discriminating imagery with a simple, covert, distributed sensor architecture has been undertaken with a multistatic ultrawideband random noise radar design. After a review of the basic research propositions, key findings and implications are drawn from the results with a look toward possible future system upgrades and research topics.

### 5.2 Review of Objectives and Methodology

The primary goal of this research was to advance the corporate knowledge of and the architecture for a distributed sensing network of ultrawideband random noise (UWB-RN) radars capable of forming high resolution target scene imagery. At a top level, the plan was to characterize node parameters, predict and measure the monostatic range resolution and accuracy performance, design, implement and demonstrate a multistatic capability, and finally, measure the localization performance of that multistatic solution. A brief review of the methodology expounds the details in executing the research plan. The research began by establishing a firm foundation on the UWB-RN radar transmitter, receiver, and multistatic theory. System design and development required discovery of the key system characteristics. This system level characterization was used to verify theoretical assumptions, make realistic performance predictions, and design subsequent performance experiments. Several core software developments were undertaken, specific to meeting the objectives of multistatic operation, system calibrations, and performance analysis. A suite of deployable and central processing software modules were the key enablers in integrating the sys-

tem of systems, proving the feasibility of multistatic operations, and conducting the experimental trials. In addition to the core multistatic control and processing functions, calibration routines and quick-look/system health tools were implemented as required to carry-out the performance experiments. Finally, post-processing and imagery analysis tools are developed to objectively evaluate the range and cross range accuracy and resolutions measured in the experiments. Four sets of performance experiments were conducted to demonstrate and assess the target estimation capabilities of the various system configurations. The localization performance metrics of interest consisted of target resolution and accuracy for 1) the single node monostatic range measurement, and 2) the multistatic downrange and cross-range performance metrics.

### 5.3 Results and Contributions

The primary objectives of developing and evaluating the multistatic AFIT noise network (NoNET) were achieved by successfully demonstrating and assessing the target localization accuracy and resolution of both the system and system of systems. The major contribution of this research is the successful collection, multistatic processing and central fusion of all 16 available signal channels. It represents a first-ever distributed sensing capability using a network of active UWB-RN radars, specifically designed to exploit the bistatic channels of the system. This leap in demonstrated noise sensor technology essentially squares the available information for more accurate, higher resolution imagery. Additional contributions include the integration and evaluation of distributed signal and data processing software modules that allow direct memory access to the signal data at each node. The AFIT NoNET central controller and data processing architecture can now command the entire cluster of widely deployed radar nodes all via a single MATLAB<sup>®</sup> command window. Finally,



the detailed theoretical underpinnings, system operating level characterization, and performance assessment provides a benchmark for all future system enhancements and research into advanced AFIT NoNET applications.

## 5.4 Future Work

Numerous system improvements and possible future research topics exist in this broad study of noise radar technology. Some proposals stem from observations made during the system development, integration and experiments, while others come from interesting concepts discovered while researching the available technical literature. Suggested future research in the area of UWB-RN radar includes:

- Feasibility and benefits of multistatic UWB-RN radar for through-the-wall, through-the-roof, ground penetration, or foliage penetration missions
- SIMO and Passive bistatic radar using noise sources of opportunity
- Modeling and simulation of the AFIT NoNET system
- Evaluation of multistatic clutter characteristics [10]
- Research on the forward-scatter pattern of UWB-RN waveform for a variety of both simple and complex objects [19]
- Explore the existence of and any potential in resonance enhancements when the incident wave is UWB-RN [55]
- Explore developments as a multi-role system, where receivers are available for SIGINT/ELINT, transmitters available for wideband communications jamming, or simply passive radar modes

- Model the aggregate survivability advantage of UWB-RN and multistatic LPI features (possibly a joint effort with ops research modelers).

#### **5.4.1 System Hardware Improvements.**

- Enhancement of the ultrawideband antennas (possibly with a Vivaldi or patch array design) for a more uniform response and broader effective bandwidth of the emitted and received noise power spectral density
- Integrating voltage-controlled variable attenuators in the RF front-end. This will insure maximization of the dynamic range of the direct-conversion design and allow greater flexibility in distributing and calibrating the system.
- Addition of an embedded processor (or even manual switching) in the RF module for independent power control of transmitter and receiver chains for
- Active noise cancellation by using transmit chain bleed with controllable amplitude and delay to cancel spillover and other close-in clutter [45]
- Explore sub-Nyquist sampling and possible foldover techniques into clear spectral regions to increase effective bandwidth
- Broaden high end of spectrum and mix the transmit replica and receive signals down, exploiting the full usable 750 MHz Nyquist bandwidth of the A/D
- Reduce the ERP (which is limiting the A/D dynamic range due to spillover) and spread the noise power spectral density even wider to improve resolution and SNR
- Integrate GPS receivers for more accurate calibration and test when using widely distributed nodes; potentially use GPS timing for local software trigger

#### 5.4.2 System Software Improvements.

- Acquire license and re-architect with MATLAB<sup>®</sup>Distributed Processing Server for wireless cluster form a shared workspace
- Design digital filters based on system transfer function to better shape the digital replica - providing greater cross-power spectral density (i.e. correlation)
- Integrate CUDA's Graphics Processor APIs as an available 'lab' in the distributed digital signal processing schedule
- Develop means of maintaining synchronized laptop clocks or proper scheduling algorithms for nanosecond accuracy in multistatic software triggering [59]
- Improve latencies associated with current image processing routines, including the elliptic transformation gridding, isorange contour translations and required rotations.

## Appendix A. Matlab® Scripts

The operational code requires each node to have MATLAB® version 2008a or later, Microsoft .NET Framework 3.0 or later, and the A/D board's dynamic library, AL-NET.dll must be installed locally on the laptop. Network capability (cable or wireless) with a shared network accessible folder is also required for netted-monostatic, bistatic or multistatic operations. The distributed and central MATLAB® functions utilize system I/O event listener functions for commanding remotely, and for basic save commands used in the inter-node communication (which could be improved with the MATLAB® Distributed Processing Server and associated job manager functionality). After making all other system connections at each node and insuring all nodes in the cluster are visible on the network (either ad hoc or shared access point), start MATLAB® at each node and insure the appropriate local root directory is selected. At each node, call *enable\_atnode()* and at the cluster head (central processor) call *enable\_atcentral()*. At the cluster head, make all node assignments in each ntr\* data structure as seen in Figure 45 (defaults are stored in the Node\_Config folder as *ntrs.mat*). From the cluster head's command line, call *init\_node()* for each node in the cluster (such as *init\_node(ntr2);init\_node(ntr3)*). This sends node assignments and remotely invokes the *board\_init()* distributed function. The nodes are now set for taking a measurement based on the mode and mode parameters of each ntr data structure. Call *multi\_capture()* and include an input string to specify which node numbers (assigned in the ntr data structure as ntr.num) are desired in the multi-static measurement. For example, calling *multi\_capture(0,1,1,0,0,0)* at the cluster head command line will only use nodes 2 and 3 in the measurement. Once all data is available at the cluster head, *load\_and\_process* is automatically called to compute the multistatic solution. Resulting data is stored in the Final\_Results folder at the cluster head. The ntr data structure also identifies which types of displays should

automatically be produced with the measurement.

The screenshot shows the 'Variable Editor - ntr4' window. The top table lists the fields of the 'ntr4' structure:

| Field        | Value             | Min | Max  |
|--------------|-------------------|-----|------|
| num          | 1                 | 1   | 1    |
| ntr          | 'NoNET-NTR4'      |     |      |
| coords       | [2,0]             | 0   | 2    |
| NumTrigs     | 40                | 40  | 40   |
| cluster_head | 'NoNET-NTR4'      |     |      |
| fs           | 6                 | 6   | 6    |
| xcWin        | <1x6000 double>   | 1   | 6000 |
| BNCthresh    | 300               | 300 | 300  |
| bkg_sub      | 0                 | 0   | 0    |
| bkg          | 0                 | 0   | 0    |
| savefilename | 'mono_ntr4_March' |     |      |
| display      | 'cal_out'         |     |      |
| mode         | 'cal'             |     |      |

The bottom 'Workspace' window shows a list of variables:

| Name | Value        | Min | Max |
|------|--------------|-----|-----|
| ntr1 | <1x1 struct> |     |     |
| ntr2 | <1x1 struct> |     |     |
| ntr3 | <1x1 struct> |     |     |
| ntr4 | <1x1 struct> |     |     |
| ntr5 | <1x1 struct> |     |     |
| ntr6 | <1x1 struct> |     |     |

Figure 45. Example of the Matlab® node assignment data structure.

#### Listing A.1. Distributed function to enable node's remote system I/O

```

1 %% enable_atnode
  %Enables node for system.IO event handlers
  %Builds local folder set in C:\Users\Public\
  %   INPUTS:
  %       None
6  %   OUTPUTS:
  %       global variables - init_flag set true
  %                       arm_flag set true
  %
  %Maj Matthew Nelms (10M/ENG2)
11
  global init_flag arm_flag
  init_flag=1;
  arm_flag=1;
  addpath('C:\Users\Public')
16 addpath('C:\Users\Public\Multi_mfiles\m_support')

```

```

if ~exist('C:\Users\Public\Init','dir'); mkdir('C:\Users\Public','Init'); end
if ~exist('C:\Users\Public\Arm','dir'); mkdir('C:\Users\Public','Arm'); end
%% Initiate event handler that watches for remote board_init
initnode = 'C:\Users\Public\Init';
21 fileObj_init = System.IO.FileSystemWatcher(initnode);
fileObj_init.Filter = '*.mat';
fileObj_init.EnableRaisingEvents = true;
addlistener(fileObj_init, 'Changed', @eventhandlerChangedInit);
%% Initiate event handler that watches for "Arming"; arming after new board init
26 armnode = 'C:\Users\Public\Arm';
fileObj_arm = System.IO.FileSystemWatcher(armnode);
fileObj_arm.Filter = '*.mat';
fileObj_arm.EnableRaisingEvents = true;
addlistener(fileObj_arm, 'Changed', @eventhandlerChangedArm);
31 %% Initiate event handler that watches for "ReArming"; allows rearming w/o board ...
init
rearmnode = 'C:\Users\Public\Arm'; %consolidated arm into 1 folder, but uses .txt
fileObj_rearm = System.IO.FileSystemWatcher(rearmnode);
fileObj_rearm.Filter = '*.txt';
fileObj_rearm.EnableRaisingEvents = true;
36 addlistener(fileObj_rearm, 'Changed', @eventhandlerChangedReArm);

```

**Listing A.2. Distributed function that initializes node Acquisition Board settings based on assignment**

```

function [objAcq,objBoard]=board_init
%% board_init
%Loads node assignments from Init/node-config.mat which is being "watched"
4 %Loads .NET assembly and creates class objects to get and set board config
%Sets all other acquisition parameters
% INPUTS:
%     None
% OUTPUTS:
9 %     objAcq – acq class object used to run assembly methods in take_capture
%     objBoard – board ''
%     global variables – this_node (data structure loaded from node-config)
%                         objut (uses local system time for timestamping)
%                         fs
14 %     NumTrigs (altered & used; later used in take_capture)
%     xcWin (growth var to delay rx channel captures
%     to (1) remove initial rx chain EM path length

```

```

%                                     from rx waveform (wasted correlation) or
%                                     (2) move range fov out for longer ranges
19 %
%Maj Matthew Nelms (10M/ENG2)

global this_node objut fs NumTrigs xcWin

24 load('C:\Users\Public\Init\node_config.mat') %get this_node config data struct

objut=System.DateTime;

HW_version=this_node.ntr %(was "AFIT-" or "LORE-"(64 or 32 bit); now just "...
    NoNET_NTR#"
29 fs=this_node.fs;          % GSa/s
    NumTrigs=this_node.NumTrigs;
    xcWin=this_node.xcWin;
    thresh=this_node.BNCthresh; % mV
    holdoff=1;              % us - time between virtual triggers of multitrig
34 %% Load .NET Assembly and Create Class objects
    if ~isempty('objBoard')
        NET.addAssembly('C:\Users\Public\Support\ALNet2.dll')
        pause(1)
        objBoard = nsAcqLog.nsAPI.AL8xGT(0,2,true);
39    objAcq=nsAcqLog.nsAPI.AcqParams_AL8xGT();
        objCP = nsAcqLog.nsAPI.ChanParams_AL8xGT();
        objFreq=nsAcqLog.nsAPI.Frequency;
        objVolts=nsAcqLog.nsAPI.Voltage;
        objVolts.mV=2000;
44    objCP.InputRange=objVolts; %glitch: isn't setting board's input range
        objAcq.NumberOfResultsToAverage=1; %glitch: needs to be set to one for normal op

    end

    %% Initialize Remaining Capture Parameters
49 % Set both channels' sampling rate
        objFreq.GHz=fs; %note: can interp to create fs up to 6 GSa/s / channel
        objAcq.SampleRate=objFreq;
        %objAcq.NumSamples=??? %glitch: board always collects 1us / channel / trigger
        % Set Trigger Mode conditioned on triggering role in cluster
54 if this_node.cluster_head || strcmp(this_node.mode,'netted-monostatic')
        objAcq.TriggerMode=nsAcqLog.nsAPI.eTriggerMode.Software;

```

```

else
    objAcq.TriggerMode=nsAcqLog.nsAPI.eTriggerMode.BNC;
    objAcq.TrigMode %display trigger mode
59    objVolts.mV=thresh;
    objAcq.BNCThreshold=objVolts;
    objAcq.BNCThreshold %display BNC threshold value
end
NumTrigs=NumTrigs+1; %glitch: last waveform always has extra 2 pts; DSP ignores ...
    last
64 objAcq.MultiTriggerCount=NumTrigs; %enable and set multitriggger parameter
    objAcq.MultiTriggerHoldoff.us=holdoff;

```

**Listing A.3.** Distributed function that arms node performs monostatic DSP and datalinks raw and processed data to cluster head

```

function take_capture()
%% take_capture
%   Performs waveform acquisition for both board channels
4 %   Performs primary distributed DSP and post processing
%   INPUTS:
%       None derived from stored node assignment
%   OUTPUTS:
%       None
9 %
%Maj Matthew Nelms (10M/ENG2) 10 Dec 2009

global objAcq objBoard objut fs NumTrigs xcWin this_node xc_bkg

14 c=299792458; %m/s
    if ~isempty(this_node.mode_param1); param=this_node.mode_param1; else param=1; end
    t1=tic;

    for cd=1:param
19 %% Collect waveforms
        if strcmp(this_node.cluster_head,this_node.ntr)
            pause(1.5)
            objBoard.StartCollection(objAcq,NumTrigs);
            objBoard.IssueSoftwareTrigger();
24    toc(t1)
            pause(.01)
            r=objBoard.CollectFreeRunning(NumTrigs); %DMA call

```



```

objBoard.StopCollection();
this_node.time_stamp=ToFileTime(objut.Now);
29 else %arm, wait for external triggers and capture data
objBoard.StartCollection(objAcq,NumTrigs);
time1=clock;
time2=clock;
while (etime(time2,time1)<15) %loop until all trigs collected or 15 s timeout
34     if objBoard.TriggerCount>=NumTrigs
        r=objBoard.CollectFreeRunning(NumTrigs); %DMA call
        break
    end
    time2=clock;
39 end
objBoard.StopCollection();
this_node.time_stamp=ToFileTime(objut.Now);
disp([num2str(objBoard.TriggerCount),' triggers; all waveforms collected'])
end
44 toc(t1)
%% Perform signal conditioning and Monostatic DSP
if exist('r','var')
    rnawa=zeros(fs*1e3,NumTrigs-1);
    rnwb=zeros(fs*1e3,NumTrigs-1);
49 for i=1:NumTrigs-1 %last dataset has extra pts so don't read it
    temp=GetValue(r,i-1); %also, i-1 since .NET array indexed from 0 to N-1
    temp_a=Get(temp.Waveforms,0); %pull and convert data from board waveforms
    temp_b=Get(temp.Waveforms,1);
    rnawa(:,i)=double(temp_a.Data);
54    rnwb(:,i)=double(temp_b.Data);
end
disp('Successful collect, now running DSP routines')
rawtx=uint8_2_num(rnawa); %returns an array of double when given 2's ...
    complement
rawrx=uint8_2_num(rnwb); %returns an array of double when given 2's ...
    complement
59 xc_m=zeros(size(rawrx,1)*2-1,size(rawrx,2));

%% Monostatic Correlation (convert from A/D count to volts then correlate)
for p=1:size(rawrx,2)

```

```

64     xc_m(:,p)=xcorr(smp2volts(rawrx(:,p),-1:1,8),smp2volts(rawtx(xcWin,p),-1:1,8),...
        'unbiased');

    end

%% Monostatic Post Processing based on measurement MODE
    if ~isempty(this_node.mode_param2) %cd wait (s) or calibration target range (m)
        param2=this_node.mode_param2;
69     else
        param2=0; disp('missing config data: mode_param2')
    end

    switch lower(this_node.mode)
74     case 'bkg_sub'
        xc_avg=mean(xc_m,2)-xc_bkg;
    case 'change_det' %change detection
        if cd>1 %currently set to subtract initial capture for demo
            xc_now=mean(xc_m,2);
79            xc_avg=xc_now-xc_prev; %for true change det
            %xc_prev=xc_now; %uncomment for true change detection
        else
            xc_avg=mean(xc_m,2);
            xc_prev=xc_avg;
84            pause(param2); %param2 seconds allows time to place/move targets
        end
    case {'multi','mono'}
        xc_avg=mean(xc_m,2);
    case 'cal' %pwr cal and range cal
89        xc_avg=mean(xc_m,2);
        [spill_val,spill_ind]=max(abs(xc_avg(fs*1e3:fs*1e3+floor(fs*1e3/24),1)));
        [cal_val,cal_ind]=max(abs(xc_avg(fs*1e3+spill_ind:fs*1e3+spill_ind+floor(fs*1...
            e3/120),1)));
        this_node.cal=[cal_val,spill_ind+cal_ind,spill_ind+cal_ind-(param2*2/c*fs*1e9)...
            ]
        this_node.spill=[spill_val,spill_ind];
94        if strcmp(this_node.display,'cal_output')
            spec_an(smp2volts(rawtx,-1:1,8),smp2volts(rawrx,-1:1,8),fs*1e9,fs*1e3,size(...
                rawrx,1),2);
            plot_stats(smp2volts([],-1:1,8),smp2volts(rawtx,-1:1,8));
            plot_stats(smp2volts([],-1:1,8),smp2volts(rawrx,-1:1,8));
            plot_1d_cal(param2,fs,xc_avg,this_node.cal(1,3))
99        end

```

```

        otherwise          %a background clutter measurement defined into global var
            xc_avg=mean(xc_m,2);
            xc_bkg=xc_avg;
    end
104 else
        disp('Did not collect/process any signal data, check connections & triggering')
        rawtx=[];
        rawrx=[];
        xc_avg=[];
109     xc_m=[];
        xc_bkg=[];
        img=[];
    end
    end
114 %Datalink to cluster_head for central processing
    save(['\\',this_node.cluster_head,'Public\Results\num',num2str(this_node.num)...
        ],...
        'rawtx','rawrx','xc_avg','this_node');

    switch lower(this_node.display)
119     case 'dist_mono_1d'
        plot_1d_cal(param2,fs,xc_avg,this_node.cal(1,3))
        case 'dist_mono_2d'
            map_monostatic(xc_avg,this_node,[],'low')
    end
124 toc(t1)

    end
    %% Support function uint8_2_num
    function [value]=uint8_2_num(p)
129 %pass in an uint8 vector and outputs it's two's complement
    msb = @(x) bitshift(x,-7);
    conv2comp = @(y,x) -y.*(bitcmp(x, 8) + 1);
    value=-1.*((msb(p)-1).*p)+conv2comp(msb(p),p);
    end
134 %% Support function smp2volts
    function out=smp2volts(M,Vpp,bits)
    %pass in a vector of A/D counts, input voltage range, and bits of A/D
    Vmin=min(Vpp);
    Vmax=max(Vpp);

```

```

139 vpl_neg=(abs(Vmin))/((2^bits)/2); %volts per quantization level (neg)
    vpl_pos=(Vmax)/((2^bits)/2-1); %volts per quantization level (pos)
    if isempty(M)
        upper_q=linspace(0,1,(2^8)/2);
        lower_q=linspace(-1,0,((2^8)/2)+1);
144     out=[lower_q(1:end-1) upper_q(1:end)];
    else
        out(sign(M)==1)=M(sign(M)==1)*vpl_pos;
        out(sign(M)==-1)=M(sign(M)==-1)*vpl_neg;
        out(sign(M)==0)=M(sign(M)==0)*0;
149 end
end

```

#### Listing A.4. Central cluster head function to enable remote system I/O

```

%% enable_atnode
%Enables central (cluster head) for system.IO event handlers
%Builds local folder set for central processing in C:\Users\Public\
%Loads node configs from selectable file UNLESS recognized in workspace or GUI
5 % INPUTS:
%     None
% OUTPUTS:
%     None
%
10 %Maj Matthew Nelms (10M/ENG2) 10 Dec 2009

addpath('C:\Users\Public')
addpath('C:\Users\Public\Multi_mfiles')
addpath('C:\Users\Public\Multi_mfiles\m_support')
15 if ~exist('Final_Results','dir'); mkdir('C:\Users\Public','Final_Results'); end
    if ~exist('Results','dir'); mkdir('C:\Users\Public','Results'); end
    %% Initiate event handler that watches for available node results
    if ~exist('fileObjcentral','var')
        data_avail = 'C:\Users\Public\Results';
20     fileObjcentral = System.IO.FileSystemWatcher(data_avail);
        fileObjcentral.Filter = '*.mat';
        fileObjcentral.EnableRaisingEvents = true;
        addlistener(fileObjcentral, 'Changed', @eventhandlerChangedResults);
    end
25 if ~exist('ntr1','var') && isempty(get(0,'CurrentFigure')) %check workspace/GUI
    load(uigetfile('*.*mat','Select the MAT-file containing node config'));

```

```

else disp('building node configs from current workspace variables or GUI')
end

```

**Listing A.5. Central cluster head function that initializes all desired nodes in cluster**

```

function init_node(ntr)
2 %% init_node
  %Commands node to call its board_init()
  %Assigns the node configuration; node loads node_config.mat;
  % INPUTS:
  %     node configuration data structure that defines this_node
7 % OUTPUTS:
  %     global variables – this_node (data structure sent for this_node)
  %
  %
  %Maj Matthew Nelms (10M/ENG2) 10 Dec 09
12
  global this_node
  if isfield(ntr, 'mode')
      this_node=ntr;
      save(['\\', this_node.ntr, '\Public\Init\node_config.mat'], 'this_node');
17 elseif isempty(ntr) %set up default monostatic case using NoNET-NTR1
      this_node.num=2;
      this_node.ntr='NoNET-NTR1';
      this_node.coords=[2 0];
      this_node.NumTrigs=40;
22  this_node.cluster_head='NoNET-NTR1';
      this_node.fs=6; % thousands of samples to collect per trigger
      this_node.xcWin=1:6000;
      this_node.BNCthresh=500;
      this_node.mode='cal';
27  this_node.display='cal_output';
      this_node.savefilename='Downrange';
      save(['\\', this_node.ntr, '\Public\Init\node_config.mat'], 'this_node');
end

```

**Listing A.6. Central cluster head function that arms cluster and computes multistatic measurement**

```

function multi_capture(a,b,c,d,e,f)
%% multi_capture

```

```

    %Used after boards at each node have been manually initialized using board_init*
    %Can be recoded to loop for multiple capture sequences
5  %Maj Matt Nelms (10M ENG2) Dec 2010

    global this_node fs_hz result_flag

    fs_hz=this_node.fs*1e9;
10 total_acqs=1;
    %Nodes will take total_acqs captures (each of which can be multi-trigger)
    for i=1:total_acqs
        result_flag=1;

15 arm_nodes(a,b,c,d,e,f,'.mat');
        disp('waiting for hw or sw trigger')
        if i>1
            pause
            end %wait for the manual trigger between collects
20 % change in local \Results folder should cause load_and_process.m to call
        arm_nodes(a,b,c,d,e,f,'.txt');

    end

25 function arm_nodes(a,b,c,d,e,f,type)

    arm_flag=1;
    if a
        save(['\\NoNET-NTR1\Public\Arm\multi_capture',type],'arm_flag')
30 end
    if b
        save(['\\NoNET-NTR2\Public\Arm\multi_capture',type],'arm_flag')
        end
    if c
35 save(['\\NoNET-NTR3\Public\Arm\multi_capture',type],'arm_flag')
        end
    if d
        save(['\\NoNET-NTR4\Public\Arm\multi_capture',type],'arm_flag')
        end
40 if e
        save(['\\NoNET-NTR5\Public\Arm\multi_capture',type],'arm_flag')
        end

```

```

    if f
        save(['\\NoNET-NTR6\Public\Arm\multi_capture',type], 'arm_flag')
45 end

```

**Listing A.7. Central cluster head function automatically called when all data is available at cluster head for multistatic processing**

```

function load_and_process()
%% load_and_process
%When data becomes available in C:\public\Results\ as an num*.mat,
%triggered by results listener, loads each data set into workspace
5 %and cross correlates all bistatic channels available for inclusion
%in multistatic solution
%Displays results based on node config data structure
%Maj Matthew Nelms (10M ENG2) Dec 2010

10 global s
    count=0;
    t1=tic;

    pause(10) % wait for all datalinks (time will vary based on first listener event)
15 s = what('C:\Users\Public\Results')
    num_nodes=length(s.mat);
    %pause(2)
    if ismember('num1.mat',s.mat)
        count=count+1;
20     data{count} = load('C:\Users\Public\Results\num1.mat');
    end
    if ismember('num2.mat',s.mat)
        count=count+1;
        data{count} = load('C:\Users\Public\Results\num2.mat');
25 end
    if ismember('num3.mat',s.mat)
        count=count+1;
        data{count} = load('C:\Users\Public\Results\num3.mat');
    end
30 if ismember('num4.mat',s.mat)
        count=count+1;
        data{count} = load('C:\Users\Public\Results\num4.mat');
    end
    if ismember('num5.mat',s.mat)

```

```

35     count=count+1;
        data{count} = load('C:\Users\Public\Results\num5.mat');
    end
    if ismember('num6.mat',s.mat)
        count=count+1;
40     data{count} = load('C:\Users\Public\Results\num6.mat');
    end
    %% Perform bistatic DSP for each possible channel
    if num_nodes>=1
        xc_length=length(data{1}.xc_avg);
45     this_chan=cell(num_nodes,num_nodes);
        bi_xc=zeros(5,xc_length);
        p=zeros(num_nodes,num_nodes);
        ind=abs(eye(num_nodes,num_nodes)-1); %Creates MK array with ones for bistatic ...
            channels
        for k=1:num_nodes
50         this_chan{k,k}.fs=data{k}.this_node.fs;
            tau_zero=data{k}.this_node.fs*1e3-600; %delays in triggering make origin < R...
                [0]
            bi_ind=1;
            p(k,:)=ind(k,:).*(1:num_nodes);
        for j=p(k,:) %all available channels
55         if j~=0 %condition met when it is a bistatic channel
            this_chan{k,j}.display=data{j}.this_node.display;
            this_chan{k,j}.tx_node=data{k}.this_node;
            this_chan{k,j}.rx_node=data{j}.this_node;
            for i=1:5%size(data{1}.rawtx,2) %reduced to 5 because of relative clock drift
60                 bi_xc(i,:)=xcorr(data{j}.rawrx(:,i),data{k}.rawtx(:,i),'unbiased');
            end
            this_chan{k,j}.response=mean(bi_xc,1);
            this_chan{k,j}.bi_xc=bi_xc;
            if strcmp(data{k}.this_node.mode,'cal')
65                 [this_chan{k,j}.cal_mag,this_chan{k,j}.cal_smpshift]=max(this_chan{k,j}....
                    response(1,tau_zero:tau_zero+1400));
            end
            if strcmp(data{k}.this_node.mode,'background')
                this_chan{k,j}.bi_bkg=mean(bi_xc,1);
            end
70         channel=[num2str(k),'_',num2str(j)];

```



```

this_chan{k,j}.coords=[data{k}.this_node.coords; data{j}.this_node.coords];% ...
    bistatic baseline
save(['\\',data{1}.this_node.cluster_head,'\\Public\Final_Results\\',data{1}....
    this_node.savefilename,'_',num2str(data{1}.this_node.time_stamp)]);
if strcmp(this_chan{k,j}.display,'central_bi_1d')
    plot_1d_bistatic(this_chan{k,j}.fs,this_chan{k,j}.response,data{k}.this_node....
        savefilename,channel);
75     end
    disp('got a bi_all');
    bi_ind=bi_ind+1;
else
    this_chan{k,k}.display=data{k}.this_node.display;
80     this_chan{k,k}.this_node=data{k}.this_node;
    this_chan{k,k}.response=data{k}.xc_avg;
    if strcmp(data{k}.this_node.display,'central_mono_1d')
        plot_1d_cal(0,data{k}.this_node.fs,data{k}.xc_avg,data{k}.this_node.cal(1,3))
    end
85 end
end

end
elseif num_nodes==1
90     if strcmp(data{1}.this_node.display,'central_mono_1d')
        plot_1d_cal(0,data{1}.this_node.fs,data{1}.xc_avg,data{1}.this_node.cal(1,3))
    end
    disp('multistatic solutions not computed, only monostatic signal data ...
        available');
else
95     disp('check triggering ... no data collected');
end
save(['C:\Users\Public\Final_Results\\',data{1}.this_node.savefilename,'_',num2str(...
    data{1}.this_node.time_stamp)], 'this_chan');
toc(t1); disp('all data processed, saved, and 1d plot results complete')
switch lower(this_node.display)
100     case 'central_mono_2d'
        im_multilateration(this_chan,[],[], 'low')
    case 'central_bistatic_2d'
        im_multilateration(this_chan,[],[], 'low')
    case 'central_netted-monostatic_2d'
105     im_multilateration(this_chan,[],[], 'low')

```

```
        case 'central_multistatic_2d'  
            im_multilateration(this_chan,[],[],'low')  
end  
toc(t1)
```

## Bibliography

- [1] Axelsson, S. “Random Noise Radar/Sodar with Ultrawideband Waveforms”. *IEEE Trans.on Geo.and Remote Sensing*, 45(5):1099–1114, May 2007.
- [2] Barton, David Knox. *Radar system analysis and modeling*. Artech House, Boston, MA, 2004.
- [3] Bradley, C. J., P. J. Collins, D. G. Falconer, J. Fortuny-Guasch, and A. J. Terzuoli. “Evaluation of a Near-Field Monostatic-to-Bistatic Equivalence Theorem”. *Geoscience and Remote Sensing, IEEE Transactions on*, 46(2):449–457, 2008.
- [4] Chernyak, Victor S. *Fundamentals of multisite radar systems :multistatic radars and multiradar systems*. Gordon and Breach Science Publishers, Amsterdam, The Netherlands, 1998.
- [5] Collins, P. Technical report, Course Notes, EENG 627, RCS Analysis, Measurement, and Reduction, School of Engineering, Air Force Institute of Technology, Wright Patterson AFB, OH, Summer 2009.
- [6] Cook, Charles E. and Marvin Bernfeld. *Radar signals;an introduction to theory and application*. Academic Press, New York, 1967.
- [7] Crispin, J. W., R. J. Newman, and K. M. SIEGEL. “RCS calculation of simple shapes - Bistatic”. 1968.
- [8] D’Addio, E. and A. Farina. “Overview of detection theory in multistatic radar”. *Communications, Radar and Signal Processing, IEE Proceedings F*, 133; 133(7):613–623, 1986.
- [9] Dawood, M. and R. M. Narayanan. “Generalised wideband ambiguity function of a coherent ultrawideband random noise radar”. *Radar, Sonar and Navigation, IEE Proceedings -*, 150; 150(5):379–386, 2003.
- [10] Doughty, S. R. *Development and performance evaluation of a multistatic radar system*. PhD dissertation. University of London, London, UK, 2008.
- [11] Doughty, S. R., K. Woodbridge, and C. J. Baker. “Improving resolution using multistatic radar”. *Radar Systems, 2007 IET International Conference on*, 1–5, 2007.
- [12] Dowla, Farid U. *Handbook of RF and wireless technologies*. Newnes, Amsterdam; Boston, 2004.
- [13] Farina, A. and E. Hanle. “Position Accuracy in Netted Monostatic and Bistatic Radar”. *Aerospace and Electronic Systems, IEEE Transactions on*, AES-19(4):513–520, July 1983.

- [14] Fishler, E., A. Haimovich, R. S. Blum, L. J. Cimini Jr., D. Chizhik, and R. A. Valenzuela. “Spatial diversity in radars-models and detection performance”. *Signal Processing, IEEE Transactions on*, 54; 54(3):823–838, 2006.
- [15] Garmatyuk, D. S. and R. M. Narayanan. “ECCM capabilities of an ultrawideband bandlimited random noise imaging radar”. *Aerospace and Electronic Systems, IEEE Transactions on*, 38; 38(4):1243–1255, 2002.
- [16] Garmatyuk, D. S. and R. M. Narayanan. “Ultra-wideband continuous-wave random noise arc-SAR”. *Geoscience and Remote Sensing, IEEE Transactions on*, Dec 2002.
- [17] Glaser, J. I. “Bistatic RCS of Complex Objects near Forward Scatter”. *Aerospace and Electronic Systems, IEEE Transactions on*, AES-21(1):70–78, 1985.
- [18] Glaser, J. I. “Fifty years of bistatic and multistatic radar”. *Communications, Radar and Signal Processing, IEE Proceedings F*, 133; 133(7):596–603, 1986.
- [19] Glaser, J. I. “Some results in the bistatic radar cross section (RCS) of complex objects”. *Proceedings of the IEEE*, 77(5):639–648, 1989.
- [20] Grant, M. P., G. R. Cooper, and A. K. Kamal. “A class of noise radar systems”. *Proceedings of the IEEE*, 51; 51(7):1060–1061, 1963.
- [21] Gray, D. A., K. Kulpa, and M. Piotrkowski. “Multi-channel noise radar”. M. Piotrkowski (editor), *2nd Microwave & Radar Week in Poland. Proceedings International Radar Symposium. IRS 2006*. Univ. of Adelaide, Adelaide Australia, Institute of Electronic Systems, Place of Publication: Warsaw, Poland; Krakow, Poland. Country of Publication: Poland., Jan 2007.
- [22] Guosui, Liu, Gu Hong, and Su Weimin. “Development of random signal radars”. *Aerospace and Electronic Systems, IEEE Transactions on*, 35; 35(3):770–777, 1999.
- [23] Harris, R. W. and T. J. Ledwidge. *Introduction to noise analysis*. Pion, London, 1974.
- [24] Horton, B. M. “Noise-Modulated Distance Measuring Systems”. *Proceedings of the IRE*, 47(5):821–828, May 1959.
- [25] Jackson, M. C. “The geometry of bistatic radar systems”. *Communications, Radar and Signal Processing, IEE Proceedings F*, 133(7):604–612, December 1986.
- [26] Kantsedal, Valeriy and Konstantin Lukin. “Covert Operation of Surveillance Noise Radar”. *Radar Symposium, 2006. IRS 2006. International*, 1–4. 2006.

- [27] Knott, Eugene F., John F. Shaeffer, and Michael T. Tuley. *Radar cross section*. Artech House, Boston, Ma, 1993.
- [28] Kulpa, K., K. Lukin, W. Miceli, and T. Thayaparan. "Signal processing in noise radar technology". *IET Radar, Sonar & Navigation*, 2(4):229–232, Aug 2008.
- [29] Kulpa, K., M. Malanowski, and Z. Gajo. "Ground clutter cancellation in MIMO and multistatic noise radars". *Institution of Engineering and Technology International Conference on Radar Systems 2007*. Inst. of Electron. Syst., Warsaw Univ. of Technol., Warsaw Poland, IET, Place of Publication: Stevenage, UK; Edinburgh, UK. Country of Publication: UK., Jan 2008.
- [30] Lai, C. P. *Through Wall Surveillance Using Ultrawideband Random Noise Radar*. PhD dissertation. Pennsylvania State University, University Park, PA, Aug 2007.
- [31] Lehmann, N. H., E. Fishler, A. M. Haimovich, R. S. Blum, D. Chizhik, L. J. Cimini, and R. A. Valenzuela. "Evaluation of Transmit Diversity in MIMO-Radar Direction Finding". *Signal Processing, IEEE Transactions on*, 55; 55(5):2215–2225, 2007.
- [32] Leon-Garcia, Alberto. *Probability and Random Processes for Electrical Engineering*. Addison-Wesley Publishing Company, Inc., 1994.
- [33] Levanon, Nadav and Eli Mozeson. *Radar signals*. J. Wiley, Hoboken, NJ, 2004.
- [34] Li, Jian and Petre Stoica. *MIMO radar signal processing*. J. Wiley & Sons, Hoboken, NJ, 2009.
- [35] Mahafza, Bassem R. and Atef Z. Elsherbeni. *MATLAB simulations for radar systems design*. CRC Press/Chapman & Hall, Boca Raton, FL, 2004.
- [36] Narayanan, R. M. "Through-wall radar imaging using UWB noise waveforms". *Science Direct, Journal of the Franklin Institute by Elsevier*, 659–678, 2008. URL [www.sciencedirect.com;www.elsevier.com/locate/jfranklin](http://www.sciencedirect.com;www.elsevier.com/locate/jfranklin).
- [37] Narayanan, R. M. and M. Dawood. "Doppler estimation using a coherent ultrawide-band random noise radar". *Antennas and Propagation, IEEE Transactions on*, 48; 48(6):868–878, 2000.
- [38] Nathanson, Fred E., J. Patrick Reilly, Marvin Cohen, and Knovel. *Radar design principles*. SciTech Pub., Mendham, N.J., 1999.
- [39] Pace, Phillip E. *Detecting and classifying low probability of intercept radar*. Artech House, Boston, 2009.
- [40] Papoulis, Athanasios. *Signal analysis*. McGraw-Hill, New York, 1977.

- [41] Saville, M. and T. Hale. Technical report, Course Notes, EENG 668, Advanced Radar Systems Analysis, School of Engineering, Air Force Institute of Technology, Wright Patterson AFB, OH, Spring 2009.
- [42] Scharf, Louis L. and Cdric Demeure. *Statistical signal processing :detection, estimation, and time series analysis*. Addison-Wesley Pub. Co., Reading, Mass., 1991.
- [43] Schmitt, Ashley L. *Radar imaging with a network of digital noise radar systems*. MS. Thesis, Air Force Institute of Technology, Wright-Patterson AFB, OH, 2009.
- [44] Skolnik, Merrill I. “An Analysis of Bistatic Radar”. *Aeronautical and Navigational Electronics, IRE Transactions on*, ANE-8(1):19–27, March 1961.
- [45] Skolnik, Merrill I. *Radar handbook*. McGraw-Hill, New York, 1990.
- [46] Skolnik, Merrill I. *Introduction to radar systems*. McGraw-Hill, New York, 2001.
- [47] Taylor, James D. *Ultra-wideband radar technology*. CRC Press, Boca Raton, 2001.
- [48] Thayaparan, T., M. Dakovic, and L. Stankovic. “Mutual interference and low probability of interception capabilities of noise radar”. *IET Radar, Sonar and Navigation*, 2(4):294–305, 2008.
- [49] Theron, I. P., E. K. Walton, and S. Gunawan. “Compact range radar cross-section measurements using a noise radar”. *Antennas and Propagation, IEEE Transactions on*, 46; 46:1285–1288, 1998.
- [50] Tribble, A. C. “The software defined radio: Fact and fiction”. *Radio and Wireless Symposium, 2008 IEEE*, 5–8, 2008. ID: 1.
- [51] Viswanathan, R. and P. K. Varshney. “Distributed detection with multiple sensors I. Fundamentals”. *Proceedings of the IEEE*, 85; 85(1):54–63, 1997.
- [52] Walton, E. K., I. P. Theron, S. Gunawan, and L. Cai. “Moving vehicle range profiles measured using a noise radar”. *Antennas and Propagation Society International Symposium, 1997. IEEE., 1997 Digest*, 4:2597–2600 vol.4, 1997.
- [53] Wang, Hong, R. M. Narayanan, and Zheng Ou Zhou. “Through-Wall Imaging of Moving Targets Using UWB Random Noise Radar”. *Antennas and Wireless Propagation Letters, IEEE*, 8; 8:802–805, 2009.
- [54] Widrow, B. and I. Kollár. *Quantization Noise: Roundoff Error in Digital Computation, Signal Processing, Control, and Communications*. Cambridge University Press, Cambridge, UK, 2008.

- [55] Willis, Nicholas J. and H. Griffiths. *Advances in bistatic radar*. SciTech Pub., Raleigh, NC, 2007.
- [56] Woodward, Philip M. *Probability and information theory, with applications to radar*. McGraw-Hill, New York, 1953.
- [57] Xu, Xiaojian and R. M. Narayanan. “FOPEN SAR imaging using UWB step-frequency and random noise waveforms”. *Aerospace and Electronic Systems, IEEE Transactions on*, 37; 37(4):1287–1300, 2001.
- [58] Xu, Yi, R. M. Narayanan, Xiaojian Xu, and J. O. Curtis. “Polarimetric processing of coherent random noise radar data for buried object detection”. *Geoscience and Remote Sensing, IEEE Transactions on*, 39; 39(3):467–478, 2001.
- [59] Yang, Yanhua and Kehu Yang. “Time Synchronization for Wireless Sensor Networks using the Principle of Radar Systems and UWB Signals”. *Information Acquisition, 2006 IEEE International Conference on*, 160–165, 2006.
- [60] Zhang, Yan and R. M. Narayanan. “Design considerations for a real-time random-noise tracking radar”. *Aerospace and Electronic Systems, IEEE Transactions on*, 40; 40(2):434–445, 2004.

| REPORT DOCUMENTATION PAGE   |             |                 |                            |   | Form Approved<br>OMB No. 0704-0188   |  |
|---|-------------|-----------------|----------------------------|---|--|--|
| <p>The public reporting burden for this collection of information is estimated to average 1 hour per response, including the time for reviewing instructions, searching existing data sources, gathering and maintaining the data needed, and completing and reviewing the collection of information. Send comments regarding this burden estimate or any other aspect of this collection of information, including suggestions for reducing this burden to Department of Defense, Washington Headquarters Services, Directorate for Information Operations and Reports (0704-0188), 1215 Jefferson Davis Highway, Suite 1204, Arlington, VA 22202-4302. Respondents should be aware that notwithstanding any other provision of law, no person shall be subject to any penalty for failing to comply with a collection of information if it does not display a currently valid OMB control number. <b>PLEASE DO NOT RETURN YOUR FORM TO THE ABOVE ADDRESS.</b></p>   |             |                 |                            |   |  |  |
| 1. REPORT DATE (DD-MM-YYYY)   |             | 2. REPORT TYPE  |                            | 3. DATES COVERED (From — To)                                      |  |  |
| 25-03-2010  |             | Master's Thesis |                            | Aug 2008 — Mar 2010   |  |  |
| 4. TITLE AND SUBTITLE<br><br>Development and Evaluation of a Multistatic Ultrawideband Random Noise Radar   |             |                 |                            | 5a. CONTRACT NUMBER   |  |  |
|   |             |                 |                            | 5b. GRANT NUMBER  |  |  |
|   |             |                 |                            | 5c. PROGRAM ELEMENT NUMBER  |  |  |
| 6. AUTHOR(S)<br><br>Matthew E. Nelms, Maj, USAF   |             |                 |                            | 5d. PROJECT NUMBER<br><br>09318                                   |  |  |
|   |             |                 |                            | 5e. TASK NUMBER   |  |  |
|   |             |                 |                            | 5f. WORK UNIT NUMBER  |  |  |
| 7. PERFORMING ORGANIZATION NAME(S) AND ADDRESS(ES)<br>Air Force Institute of Technology<br>Graduate School of Engineering and Management (AFIT/EN)<br>2950 Hobson Way<br>WPAFB OH 45433-7765  |             |                 |                            | 8. PERFORMING ORGANIZATION REPORT NUMBER<br><br>AFIT/GE/ENG/10-21 |  |  |
| 9. SPONSORING / MONITORING AGENCY NAME(S) AND ADDRESS(ES)<br>Air Force Research Lab, Sensors Directorate<br>Attn: Dr. Steven K. Rogers<br>13th St, Bldg 620<br>Wright Patterson AFB, OH 45433<br>DSN: 674-9891, steven.rogers@wpafb.af.mil  |             |                 |                            | 10. SPONSOR/MONITOR'S ACRONYM(S)<br><br>AFRL/RV                   |  |  |
|   |             |                 |                            | 11. SPONSOR/MONITOR'S REPORT NUMBER(S)                            |  |  |
| 12. DISTRIBUTION / AVAILABILITY STATEMENT<br><br>APPROVED FOR PUBLIC RELEASE; DISTRIBUTION UNLIMITED.   |             |                 |                            |   |  |  |
| 13. SUPPLEMENTARY NOTES   |             |                 |                            |   |  |  |
| 14. ABSTRACT<br><br>This research studies the AFIT noise network (NoNET) radar node design and the feasibility in processing the bistatic channel information of a cluster of widely distributed noise radar nodes. A system characterization is used to predict theoretical localization performance metrics. Design and integration of a distributed and central signal and data processing architecture enables the MATLAB <sup>®</sup> -driven signal data acquisition, digital processing and multi-sensor image fusion. Experimental evaluation of the monostatic localization performance reveals its range measurement error standard deviation is 4.8 cm with a range resolution of 87.2(+/-5.9) cm. The 16-channel multistatic solution results in a 2-dimensional localization error of 7.7(+/-3.1) cm and a comparative analysis is performed against the netted monostatic solution. Results show that active sensing with a low probability of intercept (LPI) multistatic radar, like the NoNET, is capable of producing sub-meter accuracy and near meter-resolution imagery. |             |                 |                            |   |  |  |
| 15. SUBJECT TERMS<br><br>Multistatic Radar, Distributed Sensing, Noise Radar, Low Probability of Intercept Radar  |             |                 |                            |   |  |  |
| 16. SECURITY CLASSIFICATION OF:   |             |                 | 17. LIMITATION OF ABSTRACT | 18. NUMBER OF PAGES   | 19a. NAME OF RESPONSIBLE PERSON  |  |
| a. REPORT   | b. ABSTRACT | c. THIS PAGE    |                            |   | Dr. Peter J. Collins   |  |
| U   | U           | U               | U                          | 139   | 19b. TELEPHONE NUMBER (include area code)<br>(937) 255-3636, x7256; peter.collins@afit.edu |  |